A Cyclic Growth-Dissolution Process for the Controlled Manipulation of Crystal Shape Distributions

Dissertation

zur Erlangung des akademischen Grades

Doktoringenieur
(Dr.-Ing.)

von Dipl.-Ing. Holger Eisenschmidt

geb. am 26. 10. 1983 in Magdeburg

genehmigt durch die Fakultät für Verfahrens- und Systemtechnik

der Otto-von-Guericke-Universität Magdeburg

Abstract

This work addresses the controlled shaping of crystal distributions via a cyclic growth-dissolution process. This process concept is motivated by the fact that the final crystal shape distribution is an important product property of crystalline material, which can be altered through manipulation of the solution temperature only. As this process concept results in a higher complexity compared to simple batch operation, adequate models and control approaches are required. The development of these models and routines is addressed in the work, which can be subdivided into three major parts.

Details on the experimental setup and procedures that are employed in this work are given in the first part of this manuscript. Special emphasis is laid here on the development of a measurement technique capable of observing the crystal size and shape distribution in real time. Additionally, also the model that is used to describe the dynamics of the crystallization process is specified.

The second part of this work addresses the determination of the kinetics that are governing the crystallization process. The face-specific growth kinetics of potassium dihydrogen phosphate (KDP) are determined and parameterized as a function of supersaturation and temperature. It is argued that the growth kinetics of the $\{100\}$-faces of KDP are substantially influenced by the presence of impurities in the solution. This influence is discussed and modeled in more detail on the basis of the BFC-theory in conjunction with the step-pinning mechanism. In a further analysis of the experiments, employed for the determination of the growth kinetics, also growth rate dispersion and nucleation is observed. Kinetic model for both phenomena are identified and parameterized. Finally, also the determination of the face-specific dissolution kinetics of KDP is addressed. The dissolution kinetics are again determined and parameterized as a function of undersaturation and temperature. It is argued that dissolution is, in contrast to growth, limited by bulk diffusion.

The final part of the manuscript addresses the control of crystal shape distributions in a cyclic growth-dissolution process. The routines necessary for this process are described, which include the derivation of the time-optimal process strategy, as well as the introduction of a PI-supersaturation feedback controller and a derivation of time-optimal switching procedures for switches from growth to dissolution conditions and vice versa. In order to improve the controllability of the crystal shape trajectory, a Kalman filter is employed to smoothen the measurements of the crystal size and shape distributions. All those routines are embedded in a controller structure that is subsequently employed to realize a feedback-controlled growth-dissolution process on an experimental level. It is demonstrated that a tight control of the evolution of the crystal shape trajectory can be achieved by the developed methods. The concept of growth-dissolution cycles is proven to be a viable process concept for crystal shaping that can be achieved by pure temperature or supersaturation control.

Zusammenfassung

In dieser Arbeit wird ein geregelter Prozess aus Zyklen von Wachstums- und Auflösungsphasen zur gezielten Steuerung von Kristallformverteilungen untersucht. Dieses Prozesskonzept wird durch die Tatsache motiviert, dass die finale Kristallformverteilung eine bedeutende Produkteigenschaft von kristallinem Material darstellt, welche hier durch alleinige Temperaturregelung beeinflusst werden kann. Da dieses Prozesskonzept erheblich komplexer ist als einfache Batch-Prozesse, sind adäquate Modelle und Strategien zur Beschreibung bzw. Regelung des Prozesses notwendig.

Details zum Aufbau und zum Ablauf der Experimente werden im ersten Teil dieser Arbeit beschrieben. Hierbei wird insbesondere auf die Entwicklung eines Beobachters eingegangen, mit dem sich die Kristallformverteilung in Echtzeit bestimmen lässt. Zusätzlich werden auch die Modellgleichungen zur Beschreibung der Prozessdynamiken in diesem Teil spezifiziert.

Der zweite Teil dieser Arbeit thematisiert die Bestimmung und Beschreibung der wichtigsten kinetischen Effekte des Kristallisationsprozesses. Die flächenspezifischen Wachstumskinetiken von Kaliumdihydrogenphosphat (KDP) werden in Abhängigkeit von Übersättigung und Temperatur bestimmt und parametriert. Es wird argumentiert, dass das Wachstum der {100}-Flächen von KDP erheblich durch das Vorhandensein von Verunreinigungen beeinflusst wird. Dieser Einfluss wird detaillierter betrachtet, und durch die Verbindung der Theorien zum Spiralwachstum und zum Einfluss von Verunreinigungsmolekülen auf das Kristallwachstum modelliert. In einer weiterführenden Analyse der Versuche zur Bestimmung der Wachstumskinetiken werden zusätzlich Wachstumsdispersion und Keimbildung beobachtet. Kinetische Modelle werden für beiden Phänomene identifiziert und parametriert. Abschließend wird die Bestimmung der flächenspezifischen Auflösungsraten thematisiert. Diese Auflösungskinetiken werden in Abhängigkeit von Untersättigung und Temperatur bestimmt und parametriert. Die vermessenen Kinetiken deuten darauf hin, dass die Auflösung, im Gegensatz zum Wachstum, durch Diffusion in der Lösung limitiert ist.

Im letzten Teil dieser Arbeit wird die Kristallformsteuerung durch geregelte Zyklen von Wachstum und Auflösung betrachtet. Hierzu werden zunächst Strategien beschrieben die zur Prozessregelung verwendet werden. Diese umfassen die Bestimmung von Optimalsteuerungsprofilen, die Entwicklung eines PI-Reglers zur Übersättigungsregelung sowie die Bestimmung von zeitoptimalen Routinen für das Umschalten zwischen Über- auf Untersättigung. Zur Verbesserung der Steuerbarkeit des Prozesses werden die Messwerte der Kristallformverteilung durch einen Kalman-Filter geglättet. Die genannten Regelungsstrategien werden in einer übergeordneten Reglerstruktur implementiert, die wiederum verwendet wird, um einen geregelten zyklischen Wachstums-Auflösungsprozess experimentell zu realisieren. Es wird gezeigt, dass die Trajektorie der Kristallformverteilung zielgenau geregelt werden kann. Die Anwendbarkeit von Zyklen aus Wachstum und Auflösung für die Kristallformsteuerung durch alleinige Temperaturregelung wird experimentell belegt.

Contents

Notation

Latin Symbols

$\mathbf{A}$	Jacobian matrix	
A	surface area	m^2
a	constant coefficients of Eqs. (2.28a) and (4.9a)	
$\mathbf{B}$	Jacobian matrix	
B_{nuc}	nucleation rate	$1/(m^3 s)$
b	constant coefficients of Eqs. (2.28b) and (4.9b)	
$\mathbf{C}$	Jacobian matrix	
c	constant coefficients of Eqs. (2.28c) and (4.9c)	
c_p	heat capacity	$J/(kgK)$
c_i	empirical constants of Eqs. (2.2), (3.13), (3.14) and (3.22)	variable
$\mathbf{D}$	vector of dissolution rates	m/s
D_i	dissolution rate of face i	m/s
d	diameter	m
$d_{0,i}$	empirical pre-factor for growth rate diffusivity of face i	m^2/s
d_i	growth rate diffusivity of face i	m^2/s
E_A	activation energy	J/mol
f	(bivariate) population density	m^{-5}
f	function relating a previous state to the current	
$\mathbf{G}$	vector of growth rates	
G_i	growth rate of face i	m/s
g	function relating a state to the measurements	
$\Delta \tilde{H}_{KDP}$	crystallization enthalpy	J/mol
$\mathbf{h}$	geometrical state vector	m
$\overline{\mathbf{h}}$	vector of mean geometrical state	
h_i	face distance of face i	m
$\mathbf{I}$	identity matrix	
I	intensity (grayscale) level	
$\mathbf{K}$	Kalman gain matrix	
K	temperature dependent constant	
K_p	controller parameter	K
k	growth - / dissolution rate constant	m/s
k	heat transfer coefficient	$W/(m^2 K)$
k_0	pre-exponential factor	m/s
$k_{0,N}$	pre-exponential factor for nucleation	$1/(m^{3-n_M} s) / 1/(m^3 s)$
k_B	Boltzmann constant	J/K
L	length	m
m	mass	kg
$\dot{m}$	mass flow	kg/s

$\tilde{m}$	molar mass	kg/mol
$\mathbf{N}$	matrix of face normals	
N	number	
$\mathbf{n}_i$	face normal vector of the face i	
$n_{\mathrm{d},i}$	empirical exponent for growth rate diffusivity of face i	
P	crystal polyhedron	
P_{Th}	thermostat power	W
$\mathbf{P}_{\mathrm{k}}$	*a posteriori* estimate of the error covariance matrix	
$\mathbf{P}_{\mathrm{k}}^{-}$	*a priori* estimate of the error covariance matrix	
$\mathbf{p}$	vector of growth affecting properties	
$\mathbf{p}$	vector of parameters	
$p_{i,j}$	factor specifying the growth rate of face i of crystal j	
$\mathbf{Q}$	process noise covariance matrix	
$\mathbf{R}$	measurement error covariance matrix	
R	universal gas constant	J/(molK)
R	correlation coefficient	
$\mathbf{r}$	vector of 3d space coordinates	m
r	radius	m
S	supersaturation	
$\bar{S}$	average supersaturation	
S^{*}	critical supersaturation	
s	empirical constant	- / °C^{-1} / °C^{-2}
T	temperature	K
$\bar{T}$	average temperature	
T_{N}	controller parameter	s/K
t	time	s
$\mathbf{u}$	vector of control inputs	m
V	volume	m^3
$\mathbf{v}$	vector of measurement noise	m
v	step velocity	m/s
v_i	convective velocity in i-th direction	m/s
$\mathbf{w}$	process noise vector	m
w	solute concentration	kg$_{\mathrm{KDP}}$/kg$_{\mathrm{H2O}}$
$\bar{w}$	average solute concentration	kg$_{\mathrm{KDP}}$/kg$_{\mathrm{H2O}}$
$\mathbf{x}$	vector of external coordinates	m
$\mathbf{x}$	vector of state variables	m
$\hat{\mathbf{x}}_k^{-}$	*a priori* state estimate	m
$\hat{\mathbf{x}}_k$	*a posteriori* state estimate	m
$\mathbf{z}$	vector of measurements	m

Greek Symbols

α	effectiveness factor	
β	angle	
γ	surface energy	J/m^2
δ	Dirac distribution	
δ_i	additional state variable of face i	m
θ	surface coverage	
λ	infrared wavelength	cm^{-1}
$\boldsymbol{\mu}$	vector of moments	
$\mu_{i,j}$	mixed moment	m^{i+j-5}
μ_A	total crystal surface area	m^{-1}
μ_V	total crystal surface volume	
v	molecular volume	m^3
ρ	density	kg/m^3
$\boldsymbol{\sigma}$	vector of standard deviations	
σ	source / sink term	1/(m^{5}s)
σ_1	critical supersaturation	
σ_i^2	variance in the direction of face i	m^2
τ	time constant	s
Ω	integration domain	

Subscripts and Abbreviations

0	initial value
ATR	attenuated total reflectance
BCF	Burton-Cabrera-Franck
back	background
bin	binary
C	crystallizer
CCG	constant crystal growth
CG	crystallizer – ground element
CS	crystallizer – side element
CSSD	crystal size and shape distribution
crit	critical radius
cryst	crystal
D	dissolution
diff	difference
end	end
enh	enhanced
est	estimated
eq	equilibrium
F	final

FTIR   Fourier transformed infrared
G   growth
G   ground element of double jacked
GAP   growth affecting property
GRD   growth rate dispersion
GU   ground element - environment
H_2O water
KDP   potassium dihydrogen phosphate
max   maximal
meas   measured
min   minimal
mod   modeled
nuc   nucleation
obs   observed
P   product
PBC   periodic bond chain
PBE   population balance equation
PI   PI controller
PLS   partial least squares
ref   reference
rel   relative
RF   random fluctuation
RMSE   root mean squared error
S   switching point
S   side element of double jacket
SU   side element - environment
seed   seed crystal population
set   set-point
sim   simulation
sus   suspension
symm   symmetric
Th   thermostat
tot   total
U   environment
val   validation

1. Introduction

Crystallization is an important unit operation in chemical production systems as about 60 % of all chemical substances that are produced by major chemical companies are formulated as solids and mostly as crystalline materials (Wintermantel 1999). In many cases, a crystallization step is not only applied to produce a solid phase, but also to serve as purification step within the entire chemical production system.

There is a variety of different crystallization processes in industrial practice. In order to classify these different processes, a distinction can be made by the phase from which the product material is crystallized. Crystalline material can, for instance, be obtained from a gaseous phase, from the melt, from the crystallization within an amorphous phase, or from the crystallization from a liquid solution. The latter process is probably the most frequent crystallization process in the chemical industry, and also this work is focused on this process type. Solution crystallization processes themselves can again be subdivided into a number of process classes, for instance according to the mode of operation (batch, semibatch, continuous), the source of crystals (seeded, unseeded, autoseeded) or the way by which supersaturation is generated (cooling, evaporation, addition of antisolvent). It is beyond the scope of this work to consider the entire class of all these processes. While some results of this work may be applicable to other solution crystallization processes as well, the focus is laid on seeded batch cooling (and heating) crystallization.

Regardless of the choice of the operation mode, a crystallization process is typically followed by further downstream processes. Such processes can, for instance, be filtration, drying or packaging. The performance of all of these subsequent processing steps is directly related to the final crystal size and shape distribution (CSSD) that results from the crystallization process. For instance a CSSD which is composed of a large amount of fines and/or needle or platelet like crystals is known to cause problems in the washing and drying steps which are employed to remove the remaining solvent or antisolvent from the product material in order to meet the purity specifications of the final product.

Such an inadequate CSSD is furthermore known as one major cause of blockage during the filtration step, which can limit the productivity of the entire production process. Thus, an undesired CSSD can severely affect the economic performance of the entire production chain and might result in an end product that does not meet the required purity specifications. In order for the CSSD to meet the specific requirements of the proceeding downstream processes a variety of different crystallizer concepts and configuration have been developed. These include controlled batch crystallizers (Abu Bakar 2009, Nagy 2011, Jiang 2014a), MSMPR crystallizers (Alvarez 2011, Wong 2012, Temmel 2016a, Temmel 2016b), tubular crystallizer (Eder 2012, Jiang 2014b, Wiedmeyer 2017a, Wiedmeyer 2017b) or fluidized bed crystallizers (Shiau 1999, Moguel 2010, Binev 2015).

Apart from the influence of the CSSD on the performance of the downstream processes, an adequate crystal shape can also influence the solid state properties of the crystalline product directly. Differences in crystal shapes imply differences in the configuration of crystal facets on the outer crystal surface. Due to differences in the arrangement of the molecules that are exposed on the individual facets, these crystal facets can have different properties themselves. This can in turn be exploited to improve the solid state properties of the product by designing a crystallization process that will yield such favorable crystal shapes. The design of catalyst particles is one of the most prominent examples in this context. The catalytic activity and selectivity can vary between different crystal facets. Hence, the design of adequate crystal shapes can directly result in better catalytic performance or the reduction of the catalyst material that is required for a specific process. Recent examples of catalyst improvement through crystal shape modification can for instance be found in Yang et al. (2008), a series of papers by Linic and Christopher (Christopher 2010, Linic 2010) or Xu et al. (2011). Apart from the example of heterogeneous catalysis, crystal shape control for the improvement of solid state properties can, amongst others, also be found in the areas of solar cell applications (Law 2005), improvement of pharmaceuticals (Muster 2002, Bladgen 2007, Variankaval 2008) or the design of particles with enhanced antimicrobial activity (Gilbertson 2016).

In order to design a crystallization process that yields an adequate CSSD, detailed knowledge about the crystallization kinetics is required. This is particularly true, for crystal shape control, as the final shape of a crystal is determined by the growth (or dissolution) rates of the individual crystal facets that are (or might be) appearing on the outer surface of the crystal.
In order to determine these growth kinetics, it was (and mostly still is) customary to track the shape evolution of single crystals under well-defined conditions in single crystal growth cells or hot-stage reactors, see for instance Ma et al. (2012a), Nguyen et al. (2014) or Ochsenbein et al. (2015) for recent examples. Such a procedure requires however a large amount of repeated experiments in order to obtain results that are not affected by the phenomenon of growth rate dispersion (Ochsenbein 2015). This makes the determination of face-specific growth rates through single crystal experiments quite time consuming. Furthermore, the applicability of the obtained kinetics to real crystallization processes remains somewhat questionable, as the process fluid dynamics can be only coarsely mimicked in single crystal cells. Additionally, crystal-crystal or crystal-wall collisions which may alter the individual face-specific growth rates do, of course, not occur in such setups.
It is hence desirable to determine the growth (and dissolution) rates under real process conditions. This notion stipulated some recent research activities in obtaining face-specific growth (and dissolution) kinetics from real process data, as for instance demonstrated recently by Ma et al. (2012b) and Ochsenbein et al. (2014, 2015) for the β-polymorph of L-glutamic acid and by Borchert et al. (2014) and Eisenschmidt et al. (2015a) for potassium dihydrogen phosphate (KDP).

Despite the important impact of the crystallization kinetics on the entire crystallization process, detailed studies on these kinetics (and particularly studies on face-specific kinetics) are still rare in the open literature. This can mainly be attributed to the lack of measurement

techniques and devices with which is it possible to track the evolution of the CSSD during the crystallization process online. The increase in the computational power of modern desktop computers allowed for the application of video microscopy for measuring the CSSD, as it became possible to perform the required image processing steps (which are computationally expensive) sufficiently fast. Consequently, several algorithms have recently been presented that relate either the individual crystal shapes (Larsen 2006, Larsen 2007a, Li 2006, Ferreira 2011, Schorsch 2012, Schorsch 2014, Borchert 2014, Le Borne 2016) or the state of the CSSD (Eggers 2008, Kempkes 2010, Zhang 2014) directly to the frames of the crystal suspension which are recorded by video microscopic devices.

While these algorithms have been demonstrated to be capable of tracking the CSSD evolution over time, real-time implementations can up to date not be found[1]. This can mainly be attributed to the high requirements in computational performance, which are necessary to process the large amount of data that is necessarily provided by the video microscopes. Nevertheless, real-time observation can be expected to be highly beneficial for the application of advanced concepts for controlling the crystallization process.

The goal of crystal shape control is clearly the design and realization of a crystallization process that yields crystalline material consisting of crystals with a desired shape distribution. This goal can for instance be achieved by the usage of additives, see Sangwal (2007) or Mullin (2001) and references therein, which alter the growth rates of individual face types and therefore alter the final crystal shape distribution. The downside of this concept is that, apart from the availability of a suitable additive, the crystal purity is decreased and that growth is hindered by the presence of additives which results in lower process productivities as well as in an increased risk of spontaneous nucleation. In an extreme case, growth can even stop completely, in which case the supersaturation can only be depleted through growth of freshly nucleated crystals, which will result in a broad CSSD. Alternatively, also solvent changes can affect the final crystal shape (Davey 1982, Lahav 2001, Mullin 2001). However, solvent changes are influencing the entire chemical production process, and are therefore rarely used in industrial applications.

An alternative to crystal shape control by such chemical means is given by the concept of crystal shape control through supersaturation control (Ristic 2001, Boerrigter 2002, Yang 2006, Borchert 2014, Eisenschmidt 2015a). This approach exploits differences in the supersaturation-dependencies of the growth rates of individual face types which are resulting in differences in the obtained final crystal shape. Supersaturation control can simply be achieved by controlling the solution temperature[2], which makes this process concept attractive for industrial applications.

However, the degree to which crystal shapes can be manipulated by supersaturation control can in practice be quite small. Hence an extension of this process concept to the application

---

[1] With the exception of Zhang et al. (2014) whose algorithm estimates mean and standard deviation of an univariate log-normal distribution and is hence structurally quite different from the aforementioned approaches, and not applicable for crystal shape monitoring.

[2] Assuming that the solubility curve exhibits a temperature dependence that is sufficiently high. This is the case for most solute-solvent systems.

of a series of growth and dissolution phases has been recently proposed and investigated by several authors (Snyder 2007a, Snyder 2007b, Bunin 2010, Lovette 2012b, Bajcinca 2013, Jiang 2014a, Eisenschmidt 2015b, Eisenschmidt 2016, Simone 2017, Bötschi 2017). The additional dissolution phases of this concept offer additional degrees of freedom that can be used to enlarge the region of attainable crystal shapes compared to pure growth processes (Lovette 2012b, Jiang 2014a, Eisenschmidt 2016, Simone 2017, Bötschi 2017). Nevertheless, the complexity of the crystallization process is significantly increased by this concept which will naturally also result in an increased process time. Therefore, this process concept requires an adequate design as well as suitable controllers. This is why the present work is dedicated to the development of these requirements and ultimately to the experimental realization of crystal shape control via growth-dissolution cycles.

1.1 Aims of this Work

The basic scope of this work is the control of crystal shapes in a crystallization process. While there are several approaches to achieve this goal (which can be realized in a variety of different crystallizer configurations), this work is restricted purely to the control of crystal shapes by supersaturation control in a seeded batch crystallization process. Thus, approaches for crystal shape control like the usage of additives or different solvents are excluded from this work as well as the concept of crystal shape control by controlling the polymorphic content. In terms of crystal shape, this work is solely focused on convex facetted crystals. Hence, dendritic crystal shapes, as they appear frequently in precipitation processes as well as non-convex crystal shapes that result from agglomeration processes are not considered here.

Special emphasis is, however, laid on the process concept of crystal shape manipulations by controlled growth-dissolution cycles, as this process was already demonstrated to enlarge the region of attainable crystal shapes compared to pure growth processes. Therefore, this concept can be expected to be applicable in a range of solute-solvent systems that stretches far beyond the example system of KDP – water that is considered here. The aim of designing, optimizing and controlling such a cyclic crystallization process directly imposes several experimental and theoretical requirements that have to be met. These requirements are therefore addressed in this work, in order to realize this cyclic growth-dissolution process:

i)   From an experimental point of view, the process requires an adequate experimental setup together with the ability of measuring the solute concentration and the state of the CSSD in real time, in order to provide a feedback for the process controller. While monitoring the concentration over time can be considered to be a standard task in crystallization process control, the monitoring of the CSSD (particularly in real time) cannot. It is hence the aim of this work, to develop and implement an observer with which it is possible to measure the state of the solid phase in real time in order to provide a feedback signal for the process control routines.

ii)   The design, optimization and control of the cyclic crystallization process requires a process model that is capable of accurately describing the most important dynamics of the system, yet simple enough to be solved in real time to be applicable within a model-based feedback controller loop.

iii)   A model-based description of the dynamics of the crystalline phase requires the availability of accurate growth and dissolution kinetics, which necessarily have to be face-specific if the crystal shape dynamics are considered. Hence, the determination of these kinetics constitutes a key requirement for the design and optimization of the process.

iv)   In order to minimize the total process time, optimal control solutions (despite their importance not derived here, but taken and adjusted from literature (Bajcinca 2013, Bötschi 2017)) need to be approximated as close as possible in the experiment. Therefore, suitable control routines have to be developed and incorporated in the overall controller structure of this work. This controller structure has, of course, to be developed as well in order to force the CSSD evolution towards a desired final shape distribution.

v)   Finally, this controller has, as well as the entire concept of crystal shape control by growth-dissolution cycles, to be validated experimentally in order to assess the capabilities and limitations of the concepts developed in this work.

1.2 Outline of this Work

In order to structure the points just given in a comprehensive manner, the remainder of this work is structured as follows:

Chapter 2 presents preliminary fundamentals of this work. The first part of this chapter specifies the experimental setup that was used (Section 2.1) as well as the model substance KDP (Section 2.2). The measurement of the solute concentration via ATR-FTIR spectroscopy is addressed in Section 2.3. Special emphasis is laid in this first part of Chapter 2 on the description of the measurement setup that was used to monitor the evolution of the CSSD, as this setup forms the basis for the determination of the crystallization kinetics and the closed-loop control of the crystallization process which are discussed in the following chapters.

Theoretical fundamentals of this work are given in the second part of Chapter 2. The mathematical model that is employed for the description of crystal shapes is given in Section 2.5. This section is followed by a brief description of the mechanisms of crystal growth and dissolution in Section 2.6. Finally, also a mathematical model for the description of the dynamic behavior of the crystallization process is derived in Section 2.7. This model includes equations for describing the dynamics of the CSSD, the solute concentration and the solution temperature.

Chapter 3 provides a detailed analysis of the dominant kinetic phenomena that were observable during the crystallization experiments. The face-specific growth kinetics are presented in Section 3.1. These kinetics were determined for constant supersaturation and constant temperature. It is argued that the growth of KDP was influenced by the presence of impurities at low supersaturations. Therefore, Section 3.2 discusses this influence on a more detailed level. The observed growth behavior is explained and parameterized by a combination of the classical BCF-theory for growing crystals and the step pinning mechanism. In a further analysis of the experiments that were conducted for the growth rate estimation, the phenomenon of growth rate dispersion is addressed in Section 3.3. It is shown, that the random fluctuation model is well suited to describe the experimental observations, and the kinetics of growth rate dispersion are determined on a face-specific level. Section 3.4 discusses the kinetics of nucleation. It is argued that the observable increase in the number of crystals is due to secondary nucleation, and an empirical power law approach is employed to parameterize the nucleation kinetics. The final section of this chapter is dedicated to the determination of the face-specific dissolution kinetics. Similarly to growth, the individual dissolution rates were determined for constant levels of undersaturation and temperature. Using the face-specific kinetics for growth and dissolution that were determined in this chapter, also some conclusions about the region of crystal shapes which are attainable by growth-dissolution cycles are drawn in the final part of this section.

Chapter 4 addresses the crystal shape manipulation through controlled growth-dissolution cycles. At first, the optimal control solutions for this process are summarized and adjusted to the kinetics that were determined in the previous chapter. These optimal control solutions require the application of growth and dissolution phases at constant levels of supersaturation and undersaturation, respectively. To meet this requirement, a supersaturation controller is developed and presented in Section 4.2 of this manuscript. A cyclic growth-dissolution process naturally requires changes from supersaturated to undersaturated conditions and vice versa. Therefore, Section 4.3 presents the time-optimal switching procedures between those levels, in order to minimize the total process time and to minimize the (somewhat uncertain) CSSD-evolution during the individual switching phases. Apart from the control of supersaturation (and switches between different supersaturations) also the crystal shape trajectory needs to be controlled in order to realize a process in which the desired final crystal shape can be reached in a reliable and precise manner. For this purpose, a Kalman filter is designed in Section 4.4, which serves to reduce the measurement error of the CSSD-observations that are obtained from the methods presented in Section 2.4. By reducing this error, the controllability of the CSSD trajectory is improved, which is employed in Section 4.5 of this chapter, where the experimental realization of controlled growth-dissolution cycles is presented.

The final chapter 5 aims at providing conclusion in light of the most important aspects of this work. These aspects include the ability to observe the CSSD in real time, the availability of precise face-specific crystallization kinetics, the possibility of closed-loop control of crystallization processes and the overall concept of growth-dissolution cycles. Alongside with

these conclusions, also an outlook on further research and development directions is given in this chapter.

2. Preliminaries

The development of a novel control concept for crystal shape distributions via growth-dissolution cycles is the main objective of the thesis. It requires both, an adequate experimental setup as well as a precise model description of the process dynamics. Therefore, this chapter is dedicated to the description of the experimental devices and procedures employed for this work. It will also introduce the modeling approaches used to describe the dynamics of the crystallization processes.

The experimental setup used throughout this work is specified in Section 2.1, where also the procedures employed for the determination of crystallization kinetics (discussed in Chapter 3) and for the experimental realization of growth-dissolution cycles (see Chapter 4) are described. The model substance of this work – potassium dihydrogen phosphate (KDP) – is introduced in Section 2.2. The crystallization processes are monitored with respect to temperature, solute concentration and the state of the solid phase. While the measurement of the solution temperature is a standard technique, the measurement of the solute concentration and the CSSD are not. But both quantities are of particular importance for the process controllers described in Chapter 4 of this work. Hence, the techniques for measuring the solute concentration and the CSSD are presented in Section 2.3 and 2.4. In order to describe the dynamics of the crystal shape evolution on a quantitative basis, an adequate crystal shape model is required: the model used in this work will thus be introduced in Section 2.5. Furthermore, as the dynamics of the crystal shape evolution is determined by the growth and dissolution rates of the individual crystal facets, the mechanisms of faceted growth and dissolution are shortly summarized in Section 2.6. In the final section of this chapter, the process model is introduced. The transient evolution of the CSSD is modeled by a population balance equation (PBE). The PBE is coupled to the state of the liquid phase through the crystallization kinetics, which depend on supersaturation and temperature. Hence, Section 2.7 also contains a set of model equations describing the dynamics of the solution concentration and temperature.

2.1 Experimental Setup

The experimental setup used in this work is shown in Figure 2.1. The crystallization experiments were performed in a flat-bottomed 3L crystallization vessel ($d = 15$ cm) that was not equipped with any further vortex breakers. The solution was agitated by a four-bladed pitch blade impeller ($d = 4.5$ cm) which was operated at a speed of 400 rpm. This agitation rate was chosen to be high enough to avoid any segregation of larger crystals on the bottom of the crystallizer, while ensuring that no air bubbles, that would impair the performance of the shape estimation routines (see Section 2.4), were entering the solution. The solution
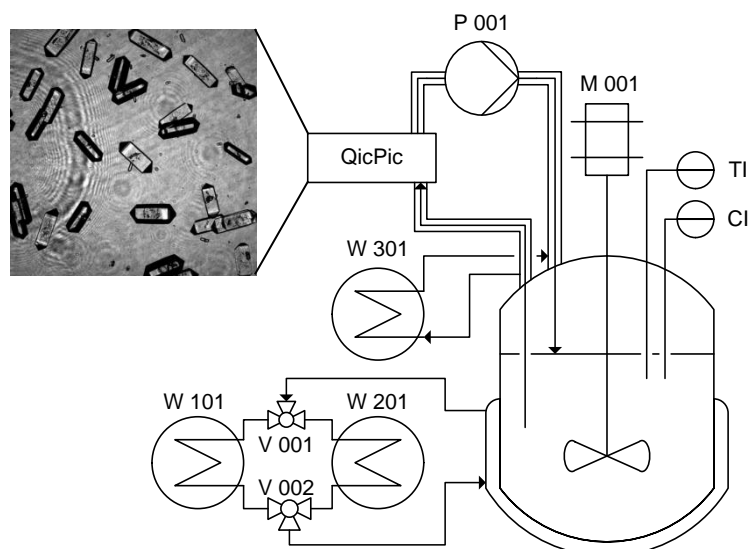
Figure 2.1: Schematic representation of the experimental setup used in this work, including the flow-through microscope (QicPic) together with an example frame collected with this microscope

temperature was monitored by a PT 100 thermocouple, and the solute concentration was measured with an ATR-FTIR probe (Nicolet iS10, Thermo Fisher), as described in more detail in Section 2.3. To control the solution temperature, the double jacked of the crystallizer was connected to two different thermostats (F 32, Julabo), W101 and W201, via two three-way valves. These valves could be simultaneously switched (switching times were below one second) to connect either the thermostats W101 or W201 to the double jacked. This setup was chosen to realize fast changes in the temperature of the cooling jacked, and hence, to allow for fast temperature – and thus supersaturation – changes in the crystallization vessel (see Section 4.3 for more details).

The state of the dispersed phase was monitored with a flow-through microscope (QicPic, Sympatec), which was continuously fed by an external sampling loop. Images of the bypassing solution were collected with this microscope having a resolution of 1024 x 1024 pixels at a frequency of 20 frames per second. The field of view had a size of 5 x 5 mm^2 and a depth of 2 mm. Within the sampling loop of this setup, the suspension was continuously withdrawn from the vessel and pumped through the cuvette of the microscope back to the crystallization vessel. The pump (PD 5206, Heidolph Instruments, P 001) was operated at a speed of 150 rpm with a flow rate of 0.52 L/min to ensure that the suspension stream was high enough to prevent both, clogging of the sampling loop and a selective sampling from the crystallization vessel. To avoid that temperature losses in the sampling loop affect the crystallization behavior, the temperature of all tubing of this loop was controlled by an additional thermostat (W301), whose set-point value was fixed to the current temperature in the crystallization vessel.

To allow for control of the crystallization process, all devices were connected to a process control system (Simantic WinCC, Siemens). Interfaces between the process control system

and Matlab® were implemented to collect all measurements necessary for process control and to pass set-point values to the thermostats and valve positions.

All experiments were prepared by dissolving KDP in 1.8 kg in deionized water (conductivity of 0.055 µS/cm). The amount of dissolved KDP corresponded to the desired level of supersaturation at the starting temperature of the individual experiment. The solution was heated above the equilibrium temperature until all crystalline material had dissolved completely. Afterwards, the solution was cooled down to the starting temperature. As soon as this temperature was reached, 1.0 g of the seed crystal material (see Section 2.2) was added to the solution for the growth experiments (Section 3.1) and 0.8 g seed material was added for the dissolution (Section 3.5) and cyclic experiments (Section 4.5). After the seed addition, the automated video acquisition was started together with the automated temperature control programs.

2.2 Potassium Dihydrogen Phosphate (KDP)

Potassium dihydrogen phosphate (KDP) was chosen as a model substance in this work. KDP crystallizes in the tetragonal space group $I\overline{4}2d$ with $a = 7.460$ Å and $c = 6.982$ Å (Botez 2010), and exposes prismatic {100}-faces and pyramidal {101}-faces on the outer crystal surface. With these face types, and the symmetry relations of the $I\overline{4}2d$ space group, the shapes of KDP crystals that are geometrically possible range from elongated crystals with a high prominence of the {100}-faces on the outer crystal surface to compact crystals, and in the extreme case to octahedral crystals exposing only the {101}-faces on the outer crystal surface, see Figure 2.2 and Section 2.5 for more details.

In recent research related to the growth of KDP crystals, two different main research areas can be identified. Due to their optical properties, KDP crystals are frequently used for optical switching and frequency conversion to the second or third harmonic frequency in high power lasers (Zaitseva 2001). Particularly the application of high power lasers in the process of inertial confinement fusion requires crystals with a size of 400 x 400 x 10 mm^3 (Maunier 2007). The demand for high-purity crystals with such extreme sizes consequently stipulated the development and enhancement of processes for the rapid growth of large single crystals with dimensions of at least 550 x 550 x 500 mm^3 (Maunier 2007) while aiming at reducing the process times and operation costs (Sasaki 1990, Zaitseva 2001, Maunier 2007, Leroudier 2011).
The second main research area, to which this work contributes as well, is related to the control of crystal shapes during a crystallization process. The qualitatively different crystal shapes shown in Figure 2.2 are not only geometrically possible, but have to be expected to occur during a crystallization process depending on the level of supersaturation (Yang 2006). Hence, univariate population balance models with their inherent assumption of constant shape factors offer a rather poor means to describe the dynamics of the crystallization
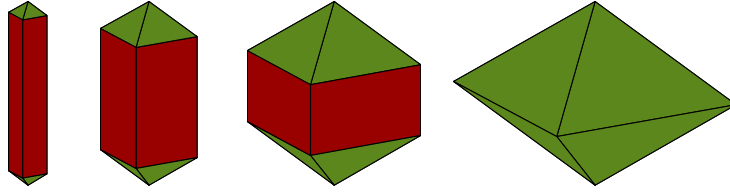
Figure 2.2: Different geometrically possible crystal shapes of KDP that are composed of prismatic {100}-faces (red) and pyramidal {101}-faces (green) on the outer crystal surface.
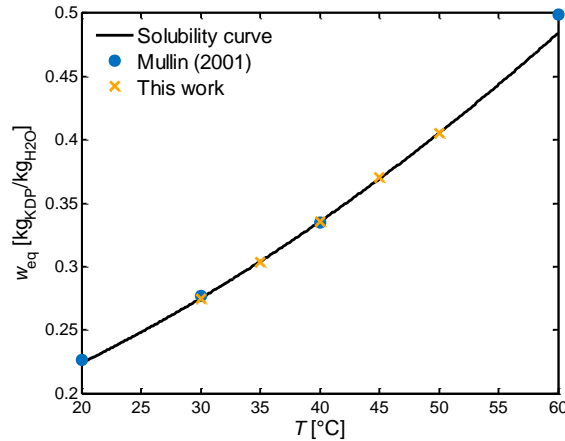
Figure 2.3: Solubility of KDP in water. Solubility data determined in this work are shown as yellow crosses, whereas solubility data given by Mullin (2001) are shown as blue points. The empirical solubility correlation of Eq. (2.2) is indicated by the black solid line.

process. Instead, these dynamics constitute a formidable example for the application of bivariate population balance models. These models require the knowledge of the face-specific growth – and dissolution rates. For KDP, their determination has been addressed by several different authors (Gunawan 2002, Borchert, 2014, Eisenschmidt 2015a, Borsos 2016). On the basis of the kinetics that were determined in these articles, process concepts for controlling the crystal size and shape distributions were developed and realized (Majumder 2013, Eisenschmidt 2015b, Eisenschmidt 2016, Borsos 2016).

The raw material of KDP used for the experiments in this work was purchased from Carl Roth GmbH + Co. KG with a purity of 98 % and a pH value of 4.12 at a saturation temperature of 35 °C. This material was used in all experiments for the preparation of the solution without any further purification.

In order to define and measure the solubility of KDP in water, the concentration w was defined as the ratio between the mass of dissolved solute and the mass of water according to:

$$w = \frac{m_{\text{KDP}}}{m_{\text{H}_2\text{O}}} .$$

(2.1)

The solubility curve of KDP was determined gravimetrically for temperatures in a range from 30 °C to 50 °C. The obtained measurements are shown in Figure 2.3, together with the solubility data given by Mullin (2001) and the empirical solubility correlation

$$w_{eq} = c_{eq,1}T^2 + c_{eq,2}T + c_{eq,3} = 4.6479 \times 10^{-5}T^2 - 0.022596\,T + 2.8535\,, \tag{2.2}$$

that was fitted to the measured solubility data. In this equation w_{eq} denotes the saturation concentration, given in kg_{KDP}/kg_{H_2O}, and the temperature T is given in Kelvin. As can be seen from Figure 2.3, the solubility measurements agree well with the data given by Mullin (2001) in the temperature range that was considered. Deviations occur only at higher temperatures, which could be addressed by taking a higher order polynomial approach in Eq. (2.2). As all experiments of this work were performed at temperatures below 50 °C this was, however, not necessary and the approach given in Eq. (2.2) was used. Using the solubility correlation of Eq. (2.2), the supersaturation S is defined as the ratio of the actual solute concentration w and the equilibrium concentration w_{eq}:

$$S = \frac{w}{w_{eq}(T)}. \tag{2.3}$$

This definition of the supersaturation was used throughout the remainder of this work as a measure for quantifying the driving force of the crystallization process. All crystallization kinetics determined in Chapter 3 are expressed as a function of S as defined through Eq. (2.3). Clearly, values of $S > 1$ indicate supersaturated conditions causing existing crystals to grow. In contrast, values of $S < 1$ indicate undersaturated conditions which result in the dissolution of crystals present in the solution.

As this thesis is dealing with seeded batch crystallization processes, adequate seed material had to be provided and specified. Preliminary experiments revealed that the raw material provided by the company Roth exhibited a rather high degree of agglomeration and was therefore deemed not suitable as seed crystal material. Instead, seed crystals were purchased from Grüssing GmbH Analytica (purity 99.5 %). This material was dry sieved, and a sieve fraction of 212 μm - 300 μm was used as seed material. The size and shape distribution of the seed material was described by a bivariate Gaussian distribution with mean values of $\overline{\mathbf{h}}_{seed,0}$ = [128 μm, 146 μm]^T, standard deviations of $\boldsymbol{\sigma}_{seed,0}$ = [25 μm, 25 μm]^T and covariances equal to zero.

2.3 Concentration Measurement

Monitoring the solute concentration during a crystallization process is essential for understanding the process dynamics, since the supersaturation as the driving force of a crystallization process is directly related to the solute concentration. In this work, the concentration was measured with an ATR-FTIR probe (Nicolet iS10, Thermo Fisher). Each collected spectrum consisted of 16 independent scans in a range of 700 cm^{-1} to 1800 cm^{-1} with a resolution of 0.482 cm^{-1}. With these settings, absorption spectra and hence estimates for the solute concentration could be obtained approximately every 20 seconds. Typical
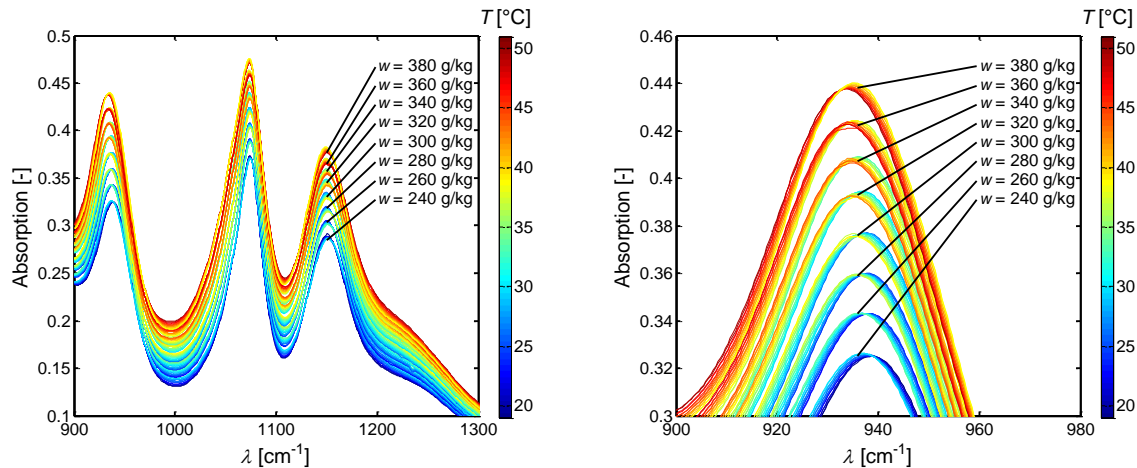
Figure 2.4: FTIR-absorption spectra that were used for calibrating the spectrometer; left: Absorption spectra collected for several concentrations and temperatures (indicated by different colors) for the main absorption peaks of KDP dissolved in water; right: detailed depiction of the absorption peak at λ = 935 cm^{-1}.

absorption spectra that were obtained are shown in Figure 2.4. Distinct absorption bands at λ = 935 cm^{-1}, λ = 1074 cm^{-1} and λ = 1150 cm^{-1} can be identified from this figure, which can be attributed to the vibration modes of the P-O and P-OH bonds in the dissociated $H_2PO_4^-$ ions (Sun 2014). As can be seen, the absorption intensity is dependent on the solute concentration, which in turn can be used to determine the concentration from the collected spectra. Apart from this concentration dependence, also a slight temperature dependence of the absorption spectra is visible, particularly in the right panel of Figure 2.4. Due to this temperature dependence, also the solution temperature had to be estimated from the spectra in order to obtain estimates for the solute concentration[3].

Various spectra in a concentration range from 240 g/kg to 380 g/kg and a temperature range from 18 °C to 52 °C were collected in order to calibrate the FTIR spectrometer. With these standards, a partial least squares (PLS) regression was performed, using the software IC Quant provided by Thermo Fisher, in a spectral range from 900 cm^{-1} to 1220 cm^{-1}. In this regression approach, seven components were considered for the determination of the concentration and six components were considered for estimating the solution temperature.. The results of this calibration are shown in Figures 2.5 and 2.6. As can be seen, the concentrations that were used for the calibration could be precisely re-estimated, with an error of only 0.1487 g/kg (indicated by the root mean squared error RMSE). Also the estimation error for the validation spectra is extremely low with an RMSE of 0.2268 g/kg. This estimation error corresponds roughly to an error of 0.075 percent in terms of

---

[3] Note that it would be possible to estimate the solution concentration directly from the measured absorption spectra and the temperature measurements of the PT100 thermocouple with the employed PLS-regression approach. However, this option was not available in the commercial software tool that was used for the concentration estimation. Hence, both, the solution concentration as well as the solution temperature had to be estimated from the measured absorption spectra simultaneously.
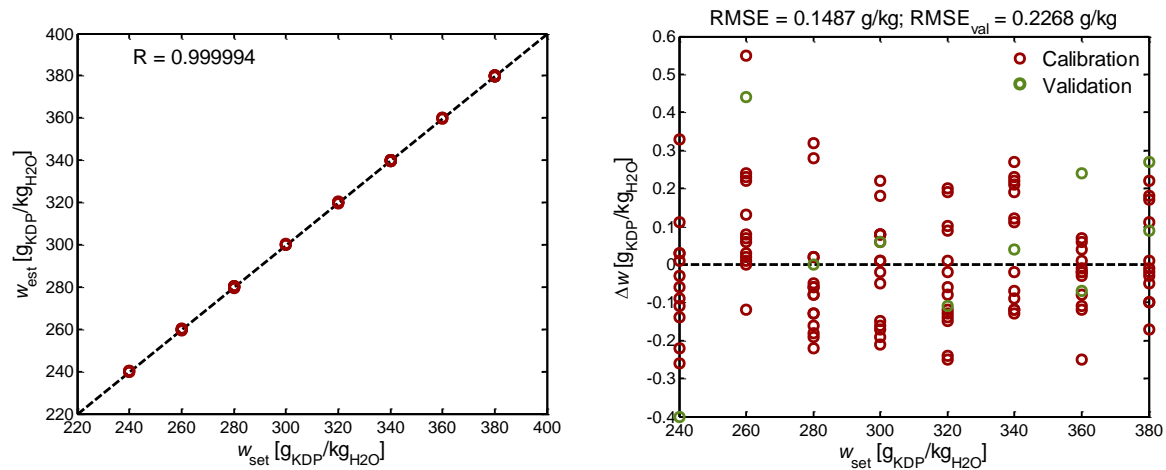
Figure 2.5: Calibration of the FTIR spectrometer for the determination of the solute concentration; left: comparison between true and estimated concentrations; right: estimation errors for the calibration spectra (red) and the validation spectra (green).
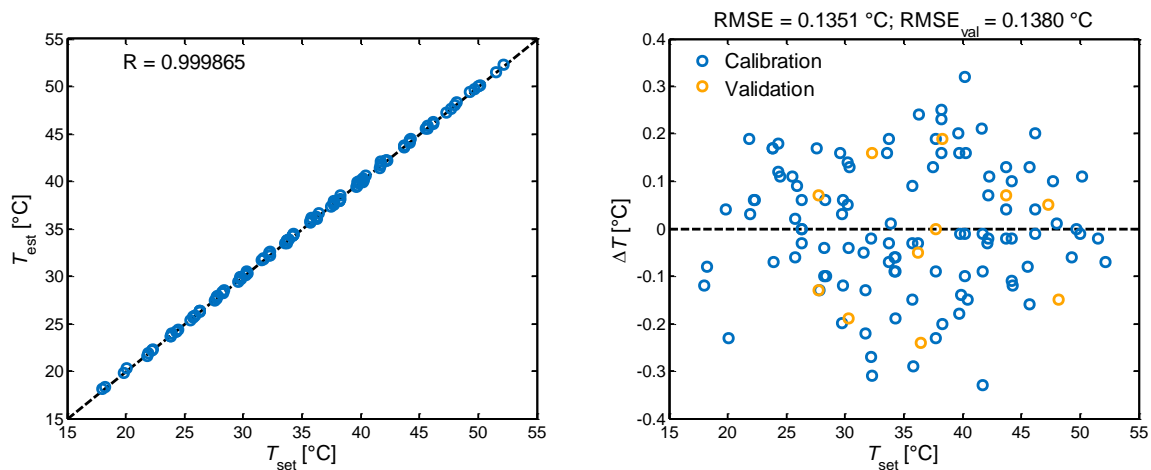
Figure 2.6: Calibration of the FTIR spectrometer for the determination of the solution temperature; left: comparison between measured and estimated temperatures; right: estimation errors for the calibration spectra (blue) and the validation spectra (orange).

supersaturation, which can be considered as sufficiently accurate for process monitoring purposes. Also the solution temperature could be re-estimated quite well with an average error of RMSE = 0.135 °C. However, since the measurement error of the PT100 that was used in this work for measuring the solution temperature was significantly lower (approximately 0.025 °C), the FTIR-based temperature estimates were not further used in the remainder of this work.

2.4 CSSD Observation

Observing the evolution of the CSSD over time is a key technique for the control of a batch crystallization process. For this purpose, and due to the increasing computational power,

video microscopy has recently become a popular measurement technique. While an immediate impression of the state of the dispersed phase can be gained with this technique, the applicability of video microscopy is typically limited to low suspension densities to avoid massive particle overlapping. This issue can be overcome by flow-through microscopes for which the crystal suspension can be diluted with a stream of clear solution as for instance demonstrated by Schorsch et al. (2012). However, an additional external sampling loop is required, which induces the danger of clogging of the tubing or of the microscope cuvette. This is, however, compensated by the improvements of the image quality, particularly in terms of particle sharpness and low particle overlap that can be obtained.

In order to estimate the shape of a crystal that was photographed with a video microscope, it is generally necessary to reconstruct the 'true' three-dimensional crystal geometry from the observed two-dimensional crystal projection. To this end, several algorithms have been presented in the literature. These algorithms include the application of wire frame models (Larsen 2007a), the use of Fourier descriptors (Li 2006), analytical considerations (Le Borne 2016), the CSSD reconstruction from axis lengths distributions measured either with a single or a stereoscopic camera setup (Eggers 2008, Kempkes 2010) and the application of generic crystal shapes (Schorsch 2012, 2014). In this work, the algorithms developed by Borchert et al. (2014) were used. These algorithms are based on the comparison of the measured crystal boundary curves to a pre-computed database, and are briefly summarized here together with the image segmentation procedure developed by Borchert and Sundmacher (2011).

In the first step of the analysis of a recorded video frame, a procedure to distinguish the objects of interest (namely the crystal projections) from the image background has to be established. Such a procedure is a standard task in digital image processing (Gonzalez 2002), commonly referred to as image segmentation, and is illustrated in Figure 2.7. As can be seen from Figure 2.7a, dark and partially transparent crystals were photographed on a comparably dark and non-uniform background. Thus, a simple global thresholding procedure was not applicable for the image segmentation. Instead, an estimate of the static background image was obtained by averaging over 30 video frames. Afterwards, the recorded video frames I were subtracted from the background image

$$I_{\mathrm{diff}}(x, y) = \left| I_{\mathrm{back}}(x, y) - I(x, y) \right|, \tag{2.4}$$

which led to images as depicted in Figure 2.7b. In such an image, background pixels were essentially black, whereas pixels belonging to a crystal had approximately the intensity of the background. This image was further enhanced by the operation

$$I_{\mathrm{enh}}(x, y) = \begin{cases} 1 - I(x, y) & \text{if } I_{\mathrm{diff}}(x, y) > I_{\mathrm{min,1}} \\ I_{\mathrm{diff}}(x, y) & \text{otherwise} \end{cases}, \tag{2.5}$$

with a threshold value of $I_{\mathrm{min,1}} = 51$[4]. Such an enhanced image is exemplarily shown in

---

[4] All images were encoded as 8-bit grayscale images. Hence, the thresholds $I_{\mathrm{min,1}}$ and $I_{\mathrm{min,2}}$ are as well given in this format. In case other image formats are used (e.g. double precision, uint16), the threshold values need to be adjusted accordingly.
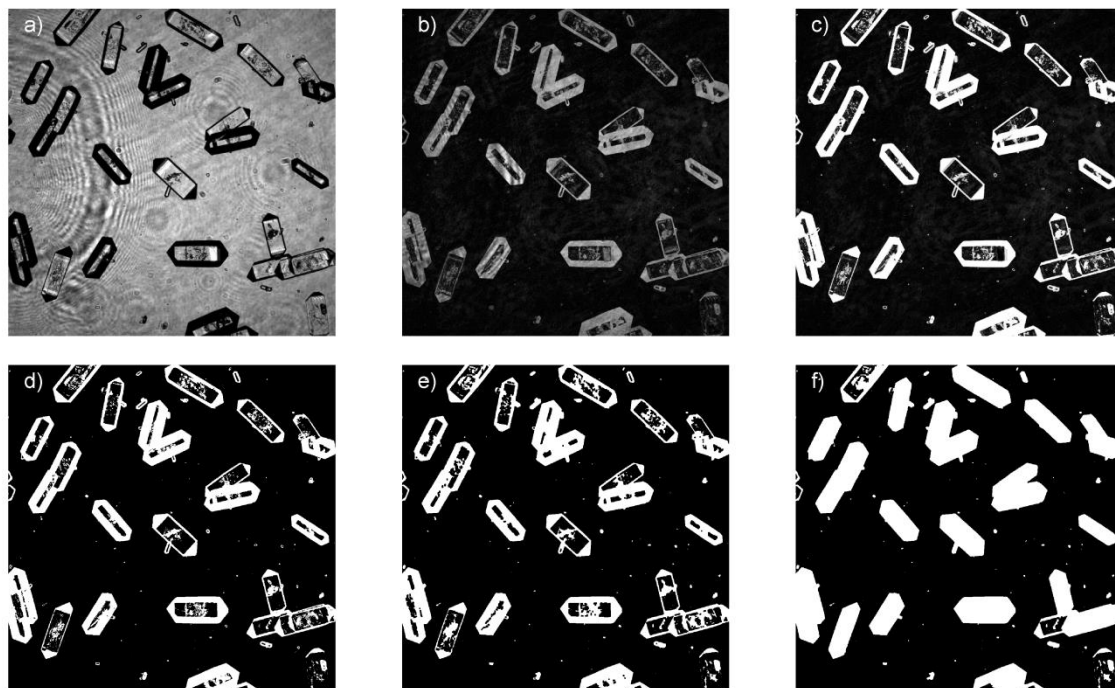
Figure 2.7: Illustration of the image segmentation procedure: a) original grayscale image; b) difference to the background; c) enhanced image; d) binary image; e) closed image; f) filled binary image.

Figure 2.7c. As can be seen, the enhanced image shows an excellent contrast between crystal – and background pixels, and hence, a global thresholding procedure could be easily and reliably applied to this image according to:

$$I_{\mathrm{bin}} = \begin{cases} 1 & \text{if } I_{\mathrm{enh}}(x, y) > I_{\mathrm{min},2} \\ 0 & \text{otherwise} \end{cases}, \tag{2.6}$$

with a threshold of $I_{\mathrm{min},2} = 100$. To close smaller gaps between the object pixels, which were occurring particularly for transparent crystals, a closing operation was performed on the binary image. For this operation a square-shaped structuring element with length of two pixels was used. Finally, a flood-filling operation was performed on the closed image, which led to binary images in which crystal pixels had an intensity value of one (white) while all background pixels had an intensity value of zero (black), as shown in Figure 2.7f.

The estimation of the crystal shapes was done on the basis of the obtained binary images, which contained the (binary) projections of the crystal shapes on the image plain. These projections are dependent on the crystal shapes itself as well as on the orientations from which these crystal were photographed. Hence, both, crystal shape and orientation had to be estimated on the basis of the recorded video frames. This was done by extracting the boundary curves from the crystal projections and by parameterizing these boundary curves through Fourier descriptors. This set of descriptors was subsequently compared to a pre-computed database, which contained in total 45,000 pre-computed sets of Fourier descriptors as well as information about the shape and orientation with which every database entry was
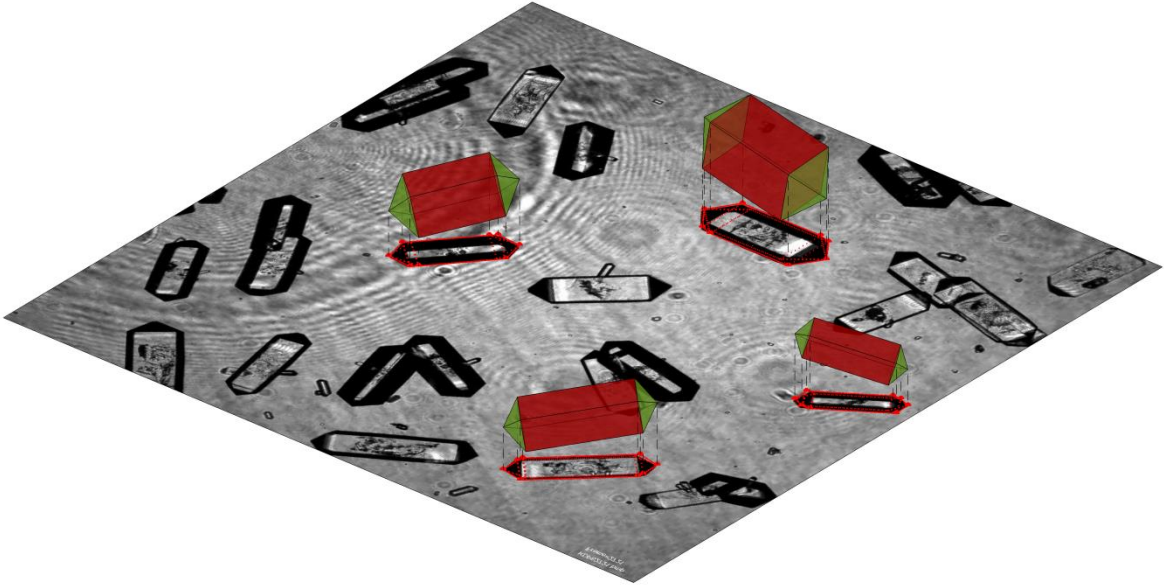
Figure 2.8: Estimated shapes of KDP crystals (color) together with the original grayscale image from which the crystal shapes were estimated.

generated. By finding the closest match of the measured boundary curve to the database entries, estimates of the crystal shape and orientation could be obtained.

The shape estimates resulting from the procedure described above are exemplarily shown in Figure 2.8 together the original grayscale image from which the crystal shapes were estimated. It can be seen that the extracted boundary curves could be approximated extremely well with this procedure. Also edges and vertices in the interior of the projection could be well reproduced with some larger deviations occurring only for the upper left crystal. This is particularly noteworthy since this information was not explicitly used within the estimation procedure. Therefore, matches or mismatches between observed and estimated features in the interior of the crystal projection can be seen as an independent benchmark to assess the quality of the crystal shape estimates. By comparing those interior features, it can be concluded that good estimates for both, the crystal shape as well as the crystal orientation were obtained with the estimation procedure.

It is also interesting to note (particularly in the light of the estimation results for dissolving crystals as discussed in Section 3.5) that the results shown in Figure 2.8 suggest a preferential orientation of the crystals parallel to the image plain. This observation can be attributed to the fluid dynamics within the microscope cuvette, which forced the crystals to have a preferentially parallel orientation to the image plane. This behavior could be well elucidated due to the simultaneous estimation of crystal shape and orientation.

Apart from the necessity for algorithms to reconstruct the three-dimensional crystal geometry from the recorded video frames, the real-time observation of a crystallization process by video microscopy also suffers from the high computational costs. The video microscope that was used in this work collected video frames with a rate of 20 frames per second at a resolution of 1024 x 1024 pixels. Hereby, every pixel was encoded by a set of three 8-bit
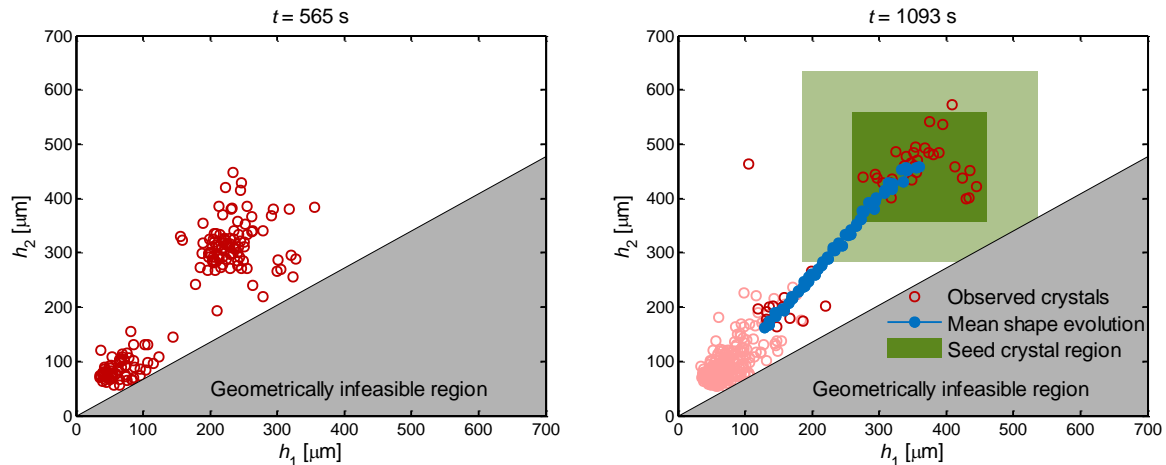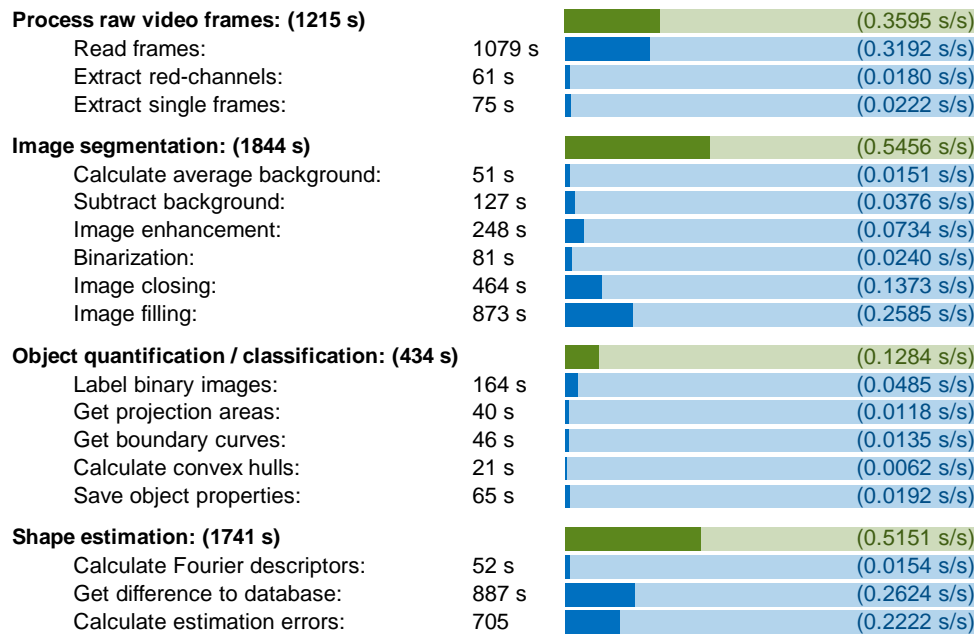
Figure 2.9: Experimentally observed crystal size and shape distributions; left: original output from the shape estimation routines showing two distinct subpopulations of seed –and nucleated crystals; right: classification of seed – (red) and nucleated crystals (light red) by two rectangular regions (light and dark green) and observed mean evolution of the seed crystal population.

unsigned integer values specifying the red, green and blue channels of the pixel[5]. Thus, raw data with a size of 60 MB had to be read (and unpacked) every second. As the intensity information in the individual color channels was redundant, only the information contained in the red-channel was extracted and further processed through Eqs. (2.4) to (2.6). Once the image processing was completed, the boundary curve of every detected single crystal was compared to the pre-computed database. This database contained the boundary curves of 300 random crystal shapes that were photographed from 150 random orientations. Every boundary curve was sampled at 128 points, which were uniformly distributed on the crystal contour and described by the same number of Fourier descriptors. With this configuration, the boundary curve of every detected crystal was compared to a database with a size of approximately 21.7 MB. As can be seen from this rough compilation of the required computation steps and their computational cost, a real time realization of those steps poses a major challenge even for modern desktop computers. For this reason, the main focus of this work was laid on an implementation of the routines described above that allow for a real-time observation of the CSSD during the crystallization process.

The application of the shape estimation routines to all observed single crystals in a collected video part leads to estimates for the CSSD as exemplarily shown in Figure 2.9. As this work is focused on monitoring and controlling the evolution of the seed crystal population, a classification between seed crystals and nucleated crystals was established. To this end, a rectangular region was defined in the state space with a size of $200 \times 200 \ \mu m^2$, depicted by the dark green area in Figure 2.9 (right). Only crystals which were found to lie within this region were considered to belong to the seed crystal population. This region was initially

---

[5] Encoding of a grayscale image does in principle not require the specification of separate red, green and blue channels. Nevertheless, an option for the direct storage of a time series of grayscale video frames was not available for the commercial software that was used for this purpose. Therefore, the video frames had to be stored in an rgb format.

Process raw video frames: (1215 s)		(0.3595 s/s)
Read frames:	1079 s	(0.3192 s/s)
Extract red-channels:	61 s	(0.0180 s/s)
Extract single frames:	75 s	(0.0222 s/s)
Image segmentation: (1844 s)		(0.5456 s/s)
Calculate average background:	51 s	(0.0151 s/s)
Subtract background:	127 s	(0.0376 s/s)
Image enhancement:	248 s	(0.0734 s/s)
Binarization:	81 s	(0.0240 s/s)
Image closing:	464 s	(0.1373 s/s)
Image filling:	873 s	(0.2585 s/s)
Object quantification / classification: (434 s)		(0.1284 s/s)
Label binary images:	164 s	(0.0485 s/s)
Get projection areas:	40 s	(0.0118 s/s)
Get boundary curves:	46 s	(0.0135 s/s)
Calculate convex hulls:	21 s	(0.0062 s/s)
Save object properties:	65 s	(0.0192 s/s)
Shape estimation: (1741 s)		(0.5151 s/s)
Calculate Fourier descriptors:	52 s	(0.0154 s/s)
Get difference to database:	887 s	(0.2624 s/s)
Calculate estimation errors:	705	(0.2222 s/s)

Figure 2.10: Detailed listing of the computation times of the most important processing steps that were spent for the analysis of a crystallization experiment having a total time of 3380 s and requiring a total computational time of 5234 s. Colorbars represent the fraction of the individual computational times on total computation time. The timings in the rightmost column represent the computational times that were in average necessary to process one video second.

centered at the mean seed crystal size of $\bar{\mathbf{h}}_{seed,0}$ and subsequently moved through the state space according to the mean seed crystal evolution. As can be seen from Figure 2.9, the evolution of the seed crystal population could be tracked reliably by this approach. However, it is also apparent that a large number of nuclei were observable, especially after prolonged growth times. As the shape estimation of such a high number of nucleated crystals (see Section 3.4) would dominate the entire computation time, a second rectangular region, centered at the mean seed crystal state was introduced with a width of 350×350 μm^2 (Figure 2.9, right, light green region). This region served to obtain a minimal and maximal projection area which is possible for seed crystals. By using these thresholds, the majority of nucleated crystals could be classified as nuclei (light red circles in Figure 2.9). Since the projection area could be efficiently measured (through the measured number of crystal pixels) during the basic image processing routines, this classification could be achieved prior to the shape estimation procedures. This led to a significant reduction of the computational costs that were required for obtaining estimates of the seed CSSD.

The total computation times that were necessary to monitor an entire crystallization process are summarized in Figure 2.10. For a better visibility of the results, the computation steps were clustered into four main groups. These clusters include the processing of the raw video frames, the image segmentation, the quantification of the identified objects and the shape estimation. It can be seen that already the reading (and unpacking) of the recorded video frames requires a substantial amount of computation time as 0.36 seconds were spent on the routines of this cluster for one video second. The image segmentation step is even

more demanding, mainly due to the closing and filling routines, as 0.54 seconds of computation time is spent per video second on this cluster. In comparison, computation time for the assignment of scalar measurements to the identified objects is almost negligible. The computation times required for the shape estimation were similar to those of the image segmentation routines. While the first three clusters are only dependent on the image resolution and (to a smaller extend) on the number of observed objects, the shape estimation routines are strongly dependent on the size of the database used for the estimation. This database-size correlates to the geometrical complexity of the crystal shapes which have to be estimated. It has therefore to be assumed, that the total computation times are dominated by this processing step, if more complex crystal shapes (i.e. for methionine or paracetamol exposing three or four different face types respectively) have to be estimated.

The timings given in Figure 2.10 and discussed above were obtained for the analysis of one preliminary experiment with a total duration of 3380 seconds on a standard desktop computer (3.00 GHz Intel dual core, 4.00 GB RAM, Matlab 2010b version 7.11, Image Processing Toobox version 7.1). In total, 1.55 seconds of computation time were (in average) required for processing one video second. Although a real time observation could not be fully achieved, the computational performance was sufficient to provide a feedback with respect to the state of the solid phase to the process control routines presented in Chapter 4. In total, a delay of $20 - 35$ seconds between the observation and the availability of the CSSD estimates could be realized. As the typical time scales for the individual growth and dissolution phases were in the order of $10 - 30$ minutes (see Chapters 3 and 4), this time delay was rather negligible, and CSSD estimates could be obtained with a sufficient frequency.

2.5 Crystal Shape

In order to understand and ultimately to control the evolution of a population of faceted crystals, an adequate description of the crystal shape is required. In simple cases, this can be achieved by using characteristic lengths of the crystal (Ma 2001, Bajcinca 2013), or by approximating the actual crystal shape by generic crystal shape models (Schorsch 2012, Ochsenbein 2014). In case of crystal shapes with a larger number of face types (which may or may not be present on the outer crystal surface) the definition of adequate characteristic lengths is in general not straightforward. These complex crystal shapes may however be approximated by generic crystal shapes, yet a distinction between different face types on the basis of generic crystal shapes might not be possible. More general frameworks for the description of crystal shapes are given by the *V*-representation (Ziegler 1995), the *H*-representation (Zhang 2006, Borchert 2012a, Borchert 2012b) or the Minkowski addition of structuring elements (Reinhold 2011). In this work, the crystal shape description through the *H*-representation was employed. Within this *H*-representation, the convex polyhedron P of a faceted crystal is described by the following set of linear inequalities:
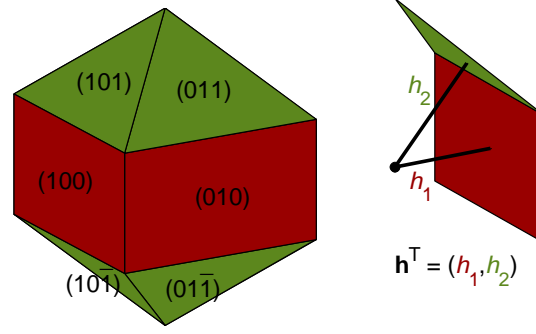
Figure 2.11: Representation of the typical geometry of a KDP crystal through the geometrical state vector h.

$$P = \left\{ \mathbf{r} \in \Re^3 : \mathbf{Nr} \le \mathbf{h} \right\}. \tag{2.7}$$

In this equation, $\mathbf{r}$ denotes a point in the three-dimensional physical space. The matrix $\mathbf{N}$ consists of the unit face normals $\mathbf{n}_i$ of all n faces of the crystal

$$\mathbf{N} = \begin{bmatrix} \mathbf{n}_1^T \\ \vdots \\ \mathbf{n}_n^T \end{bmatrix}. \tag{2.8}$$

Note, that the unit face normals $\mathbf{n}_i$ are given in Cartesian coordinates and are therefore not identical to the normalized Miller indices of the crystal faces (with the exception of crystals from a cubic space group), which are frequently used to specify crystal facets and are given in crystallographic coordinates. However, a transformation between the face normals in both coordinates systems is possible, and can for example be found in Dowty (1980) or Zhang et al. (2006). The vector $\mathbf{h}$ in Eq. (2.7) contains the perpendicular distances of every crystal face to a reference point in the physical space. In this work this reference point is set to be the center of mass of the crystal (without loss of generality). The number of elements in $\mathbf{h}$ is equal to the number of faces that can exist on the outer crystal surface (for example 12 for a KDP crystal with only {100}- and {101}-faces).

Crystals typically exhibit a certain degree of symmetry, which allows for a reduction of the dimensionality of the $\mathbf{h}$-vector. Due to the symmetry of the unit cell, certain faces will grow with the same velocity, and hence, the face distances of these faces will be identical if the center of mass is defined as a reference point for the face distances $\mathbf{h}$. In case of KDP crystals, typically two different face groups exist on the outer crystal surface, namely the prismatic {100}-faces and the pyramidal {101}-faces. It is therefore sufficient to describe the shape of a KDP crystal with only two face distances $\mathbf{h}_{symm} = [h_1, h_2]^T$. In this notation, which is used throughout the remainder of this work, the first element of $\mathbf{h}_{symm}$ - h_1 describes the distance of the prismatic {100}-faces to the crystal center, whereas the second element of $\mathbf{h}_{symm}$ - h_2 denotes the distances of the {101}-faces to the crystal center (see Figure 2.11 for an illustration). In the remainder of this work, symmetric KDP crystals will be assumed, and hence, the subscript 'symm' is skipped for the sake of brevity. Instead, the symmetric crystal shape is denoted only by $\mathbf{h} = [h_1, h_2]^T$.
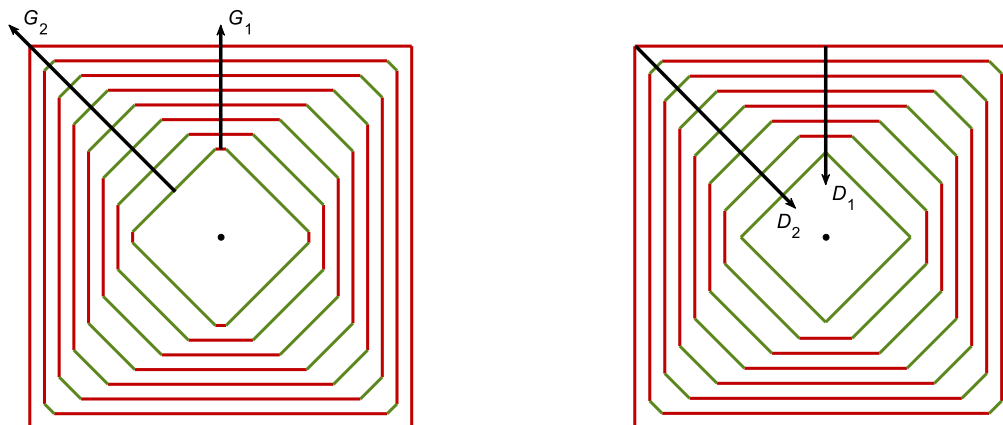
Figure 2.12: Shape changes of an exemplary 2d-crystal due to growth and dissolution; left: slow growing faces dominate the final crystal shape; right: fast dissolving faces dominate the final crystal shape.

With **h** being defined as a state vector describing the actual crystal shape, it is straightforward to define the face-specific growth and dissolution rates G_i or D_i as the derivatives of h_i with respect to time:

$$\frac{dh_i}{dt} = \begin{cases} G_i & \text{if } S \geq 1 \\ D_i & \text{if } S < 1 \end{cases}. \tag{2.9}$$

As h_i denotes the perpendicular distance of the i-th face to the crystal center, the growth or dissolution rate G_i or D_i is equivalent to the displacement velocity of the i-th face from the crystal center. The ratio between the individual displacement velocities will ultimately determine the shape towards which a growing (or dissolving) crystal will evolve. This is depicted in Figure 2.12 for an exemplary 2d crystal with two different face types for both, growth and dissolution. In both cases, the displacement velocity of the {10}-faces (red, index 1) is half the displacement velocity of the {11}-faces (green, index 2). The initial shape of the growing crystal is dominated by the {11}-faces in this example. Due the lower growth rates of the {10}-faces compared to the {11}-faces, the {10}-faces are becoming more dominant on the crystal surface as growth proceeds, until ultimately, the {11}-faces disappear completely from the crystal surface. As those faces may however reappear at the newly formed vertices (or edges in the 3d case) during the crystallization process in case the crystallization conditions change, their displacement velocity is further dictated by the displacement velocity of the {10}-faces. In such cases, the {11}-faces are referred to as virtual faces and their growth rates as virtual growth rates (Zhang 2006).

In case of dissolution, a reverse scenario arises. The {11}-faces reappear immediately on the crystal surface due to their higher dissolution rates, until ultimately, only the {11}-faces are present on the crystal surface. In this case, the {10}-faces and their dissolution rates become virtual.

Three conclusions can be drawn from this simple 2d example:
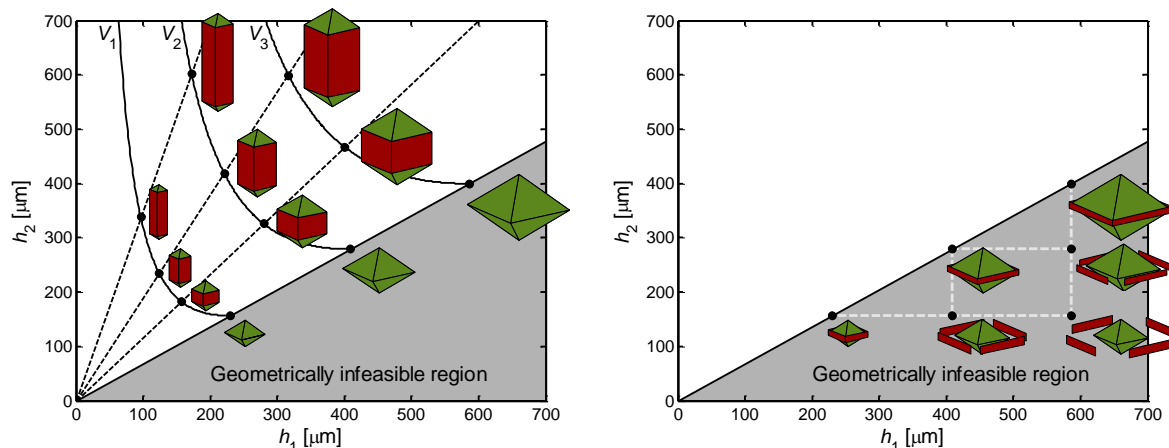
Figure 2.13: Crystal shapes of KDP in h-space; left: different shapes of KDP crystals and their position in h-space; right: crystal shapes with $h_1 > 1.4649\ h_2$ are geometrically infeasible as the {100}-faces would detach from the crystal surface. Instead, the {100}-face become virtual, and the crystal shapes are projected on the subspace $h_1 = 1.4649\ h_2$.

(i)   During growth, the slowest growing faces will dominate the outer crystal surface, while the faster growing faces might disappear completely from the surface and become virtual faces.

(ii) During dissolution, the fastest dissolving faces will be dominant on the crystal surface while the slower dissolving faces might disappear and become virtual faces.

(iii) Faces that become virtual are located on newly formed edges or vertices as they may reappear during the crystallization process. Since the displacement of such faces is further dictated by the displacement of the neighboring faces, the **h**-space is confined to a region of geometrically possible crystals shape

The last conclusion is illustrated for the example of KDP in Figure 2.13 together with different crystal shapes and their location in the state space. As can be seen, the variety of different crystal shapes range from elongated crystals with low h_1/h_2 ratios and a high prominence of prismatic {100}-faces on the outer crystal surface to compact crystals. At a ratio of $h_1/h_2 = 1.4649$ (Borchert 2012c), KDP crystals assume an octahedral shape, at which the prismatic {100}-faces are not present on the outer crystal surface. At even higher h_1/h_2 ratios the prismatic faces would detach from the crystal surface as shown in the right panel of Figure 2.13. Such a scenario is however not possible, as the {100}-face become virtual faces as soon as they disappear from the crystal surface. Therefore, their growth rates become:

$$G_1 = \min\left[G_1, 1.4649 G_2\right], \tag{2.10}$$

ensuring that the {100}-faces cannot detach from the outer crystal surface. A more detailed discussion of the structure of the **h**-space for different crystal shapes beyond KDP is not in the scope of this work. For such an overview, the reader is referred to Reinhold and Briesen (2011), Borchert and Sundmacher (2012b) or Sing and Ramkrishna (2013).

The distinction between virtual and real faces, and the resulting structure of the **h**-space is (to some extent) depending on the choice of face-types considered for the shape description in Eq. (2.7). Consider a KDP crystal exhibiting additional {001}-faces on the outer crystal surface as an illustrative example. The additional {001}-faces would allow for crystal shapes not exhibiting any {101}-faces on the outer crystal surface (which is not possible if only {100} and {101}-faces are considered). Hence the structure of feasible crystal shapes will show a higher degree of complexity than discussed above. However, {001}-faces of KDP cannot be observed experimentally as they are always virtual. In fact, even growth of artificially generated {001}-faces immediately results in the formation of {101}-faces on the macroscopic {001}-faces (Zaitseva 2001, Li 2008). Thus, the question arises which face types have to be considered for a complete description of the crystal shape dynamics that can be expected and/or observed experimentally. This question is addressed and discussed in the light of the Hartman-Perdok theory (1955) in the next section of this work.

2.6 Mechanisms for Growth and Dissolution of Faceted Crystals

Single crystals that were grown from solution under moderate supersaturations appear typically as convex objects, exposing well defined {hkl}-faces on the outer crystal surface. However, despite the vast number of {hkl}-faces that are possible from a combinatorial point of view, typically only a small number of low indexed faces can be observed experimentally. This observation was related to the molecular structure of the crystal lattice by Gibbs, who postulated that the equilibrium crystal shape should minimize the total Gibbs energy (Lovette 2008). This concept was further developed by Wulff, who derived an equivalent criterion, which is referred to as Wulff construction, and can be expressed as:

$$\frac{\gamma_1}{h_1} = \frac{\gamma_2}{h_2} = \cdots = \frac{\gamma_n}{h_n} \,. \tag{2.11}$$

Here, γ_i denotes the surface free energy of the i-th face. Hence, faces with high surface energies will have high face distances h_i, and are therefore likely to be absent from the resulting crystal surface. Following this argumentation, only faces with the lowest free energies will finally be present on the outer surface of a grown crystal.

It is, however, typically observed that crystals do not attain their equilibrium shape, since the final crystal shape is determined by the growth kinetics rather than by the thermodynamic equilibrium. Similarly to the Wulff construction, the Frank-Chernov condition (Dandekar 2013) relates the final crystal shape to the individual growth rates G_i by:

$$\frac{G_1}{h_1} = \frac{G_2}{h_2} = \cdots = \frac{G_n}{h_n} \,. \tag{2.12}$$

According to this equation, the crystal shape, which is also referred to as steady state crystal shape, is governed by the slowest growing faces. A widely accepted approach to relate the face-specific growth rates to the molecular structure of the crystal lattice is given by the
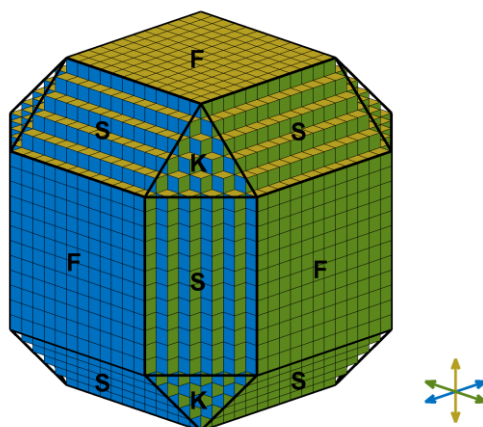
Figure 2.14: Illustration of flat (F), stepped (S) and kinked (K) faces for a crystal with three periodic bond chains (PBC), whose directions are indicated by colored double-arrows in the lower right corner. Face colors indicate the contributions of the PBCs to the attachment energy that is released when one building unit is attached to the crystal face.

Hartman-Perdok theory (Hartman 1955), which is shortly summarized here. This theory is based on the assumption that the time necessary for incorporating a molecule in the crystal lattice is inversely proportional to the attachment energy of the incorporation site. This energy is defined as the bond energy that is released by the molecular attachment. Hence, growth is accelerated (small incorporation times) at sites with high attachment energies, and thus, at sites offering high bond energies to the incorporated molecule. Conversely, growth is decelerated (high incorporation times) at sites with lower attachment energies. This model led to the concept of periodic bond chains (PBCs), which are defined as a set of the strongest bonds between the molecules (or ions) that form a regular and uninterrupted pattern in the crystal lattice.

With the concept of PBCs, the crystal faces can be classified as kinked (K) faces, stepped (S) faces and flat (F) faces, as illustrated in Figure 2.14 for the example of a Kossel crystal. Kinked faces are, by definition, not parallel to any PBC, and hence, they offer already kinked sites on their surface on which the incorporation of molecules can take place directly. Therefore, growth of K faces is assumed to be solely limited by bulk diffusion processes and consequently exhibit the fastest growth rates possible. Stepped faces are parallel to exactly one PBC, and expose steps on the surface which need to be kinked in order to facilitate growth of this face. Flat faces are defined as faces being parallel to at least two PBCs. In order for a flat face to grow, an additional mechanism (described below) is required that creates steps on the F-face which can be kinked and consequently facilitate growth of this face (Vekilov 2007, Kim 2014). Regardless of the mechanism for layer formation, it can be assumed that the average spacing of steps on F-faces will be much higher compared to S-faces (see Figure 2.14 and Figure 2.15 for an illustration) and hence, growth of F-faces will be much slower than growth of S-faces if the kinetics for kink site formations are approximately equal for both face types. It is therefore typically assumed, that the steady state shape of grown crystals expose only F-faces on the outer surface (if geometrically possible).
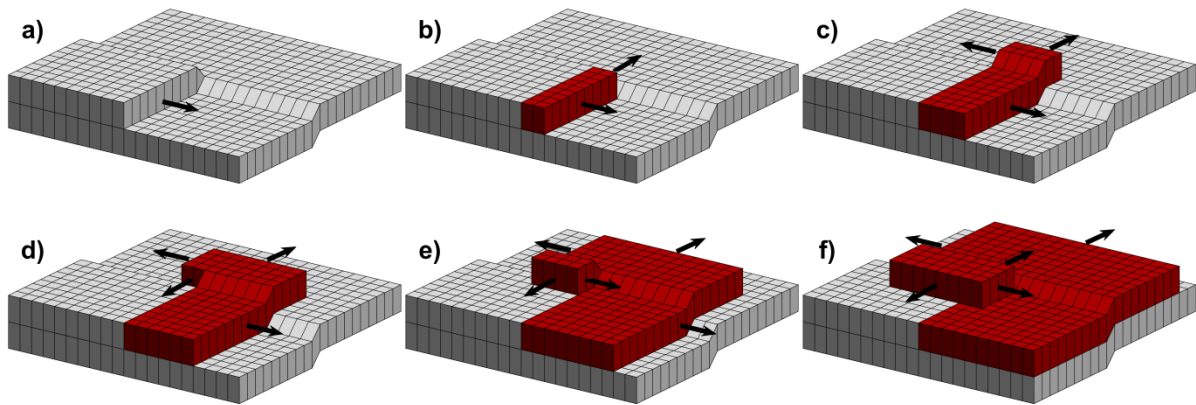
Figure 2.15: Mechanism of crystal growth via screw dislocations; a) original screw dislocation; b)-f) creation and growth of new surface layers by the srew dislocation mechanism. Arrows indicate the directions in which the created steps are growing.

One possible mechanism for the creation of growth layers is the aggregation of molecular clusters on the surface, which is typically referred to as 2d-nucleation. In order for the molecular cluster to be stable and consequently to be able to grow, the cluster size has to reach a critical size, which is a nonlinear function of the supersaturation and temperature. According to classical nucleation theory, this critical size of a two-dimensional nucleus is given by (Mullin 2001):

$$r_{crit,2d} = \frac{\gamma v}{k_B T \ln S},$$ (2.13)

where γ denotes the surface free energy, v denotes the molecular volume and k_B is the Boltzmann constant. As can be seen, the critical radius is increasing with decreasing supersaturation at which transport of molecules to the crystal surface by bulk diffusion is additionally hindered. Therefore, the probability of the formation of a stable two-dimensional nucleus is extremely low at low supersaturations, and hence, growth via this mechanism will be slow as well.

Due to these low nucleation rates, growth at low supersaturations is typically dominated by the growth from screw dislocations, which act as continuous sources of new steps on the surface of an F-face (Lovette 2008). This growth – and layer formation mechanism is illustrated in Figure 2.15. As can be seen in subfigure a), the initial screw dislocation provides one edge on the crystal surface that can directly be kinked and therefore grow. Growth takes place in a direction perpendicular to this edge, and results in the formation of a new edge (in subfigure b) perpendicular to the initial edge. As soon as this newly formed edge exceeds a critical length, growth can also take place on this edge (Lovette 2012a), whose subsequent growth will again create a new (third) edge, see subfigure c). This mechanism continues (subfigures d)-f)) and thereby new steps are permanently created on the crystal surface. Hence, crystal growth can proceed, until the supersaturation is completely depleted. Due to this mechanism, a spiral-like structure emerges on the crystal surface and therefore, this growth mechanism is also referred to as spiral growth.

Screw dislocations have also an important role in the dissolution of F-faces, since the dislocations still act as sources of edges, and thus kink sites. In case of dissolution, the presence of these dislocations results in the formation of etch pits, opposed to spirals in the case of growth, which was already predicted by Cabrera and Levine (1956) and which was observed also experimentally (Lasaga 2001, Clark 2015). This indicates that kink sites also have a pivotal role during dissolution. Apart from screw dislocations, and in contrast to growth, macroscopic crystal edges and vertices can also serve as sources for kink sites during the dissolution process. The disincorporation of molecules from these edges and vertices leads to the appearance of S- and K-faces on the outer crystal surface, see Figure 2.14. Following the same argumentation of the Hartman Perdock theory, these faces will in average expose more kink sites, and hence, dissolution of these faces will be faster than the dissolution of the F-faces (Snyder 2007a). Therefore, these faces will dominate the outer crystal surface after a sufficiently long dissolution time (compare to Figure 3.20). If the dissolution of K-faces is limited by bulk diffusion, which is a typical assumption, these face types will have the highest dissolution rates. This, and the vast number of geometrically possible kinked {hkl}-faces will therefore lead to an ellipsoidal crystal shape without the presence of any significant edges and vertices (compare also to the results and discussion of Section 3.5).

2.7 Process Model

In order to design the experiments for the determination of the crystallization kinetics (discussed in Chapter 3) as well as for the control of the cyclic growth-dissolution process (presented in Chapter 4), adequate model equation are required that describe the governing process dynamics. Therefore, this section is dedicated to the description of these model equations. The dynamic evolution of the crystal size and shape distribution (CSSD) is modeled in the first part of this section by means of a multivariate population balance equation (PBE) which is solved by the method of moments. The resulting solution of the PBE is dependent on the kinetics of crystallization, which in turn are functions of the solution concentration and temperature. Thus, the dynamic process model is equipped with additional model equations in the final parts of this section to describe the dynamic behavior of both quantities as well.

2.7.1 Population Balance Equation

Modeling a batch crystallization process requires the description of the dynamics of a crystal ensemble rather than of an individual crystal. Furthermore, the properties that are characterizing the crystalline state, i.e. the **h**-vector, will generally differ among individual crystals and hence, the crystal population is distributed in the property space. An adequate model that accounts for the dynamics of a crystal population that is distributed in the property

space is given by the population balance equation (PBE). A general formulation of the PBE is given by (Ramkrishna 2000):

$$\frac{\partial f}{\partial t} + \nabla_{\mathbf{x}} \cdot \dot{\mathbf{x}} f + \nabla_{\mathbf{h}} \cdot \dot{\mathbf{h}} f = \sigma^+ - \sigma^- .$$

(2.14)

Here, $f = f(t,\mathbf{x},\mathbf{h})$ denotes the volume specific crystal number density which is distributed w.r.t. the external coordinates $\mathbf{x}$, representing the three dimensional physical space, and w.r.t. the internal coordinates $\mathbf{h}$, representing the n dimensional geometrical property space of the crystals. While the first term on the left hand side describes the accumulation of the crystal number density, the other terms on the left hand side describe the convective transport of the crystal size distribution in the external – as well as in the internal coordinates. In crystallization processes, the corresponding transport velocities can be interpreted as the particle velocities v_i in the physical space and as the growth – or dissolution velocities G_i / D_i of the individual crystal faces:

$$\dot{x}_i = \frac{dx_i}{dt} = v_i$$

(2.15a)

$$\dot{h}_i = \frac{dh_i}{dt} = \begin{cases} G_i & \text{if } S \geq 1 \\ D_i & \text{if } S < 1. \end{cases}$$

(2.15b)

The terms σ^+ and σ^- on the right hand side of Eq. (2.14) represent birth and death terms, which are frequently used to model nucleation, agglomeration and breakage phenomena in crystallization processes. In this work, a crystallization process within a closed and ideally mixed system was considered and hence, the external coordinates were not considered. Furthermore, neither crystal growth nor dissolution was size dependent, see Section 3.1 and Section 3.5, and agglomeration and breakage were assumed to be negligible. Hence, the PBE could be simplified to:

$$\frac{\partial f}{\partial t} + \sum_{i=1}^{n} G_i \frac{\partial f}{\partial h_i} = \sigma^+ ,$$

(2.16)

with $f = f(t,\mathbf{h})$ and the following initial and regularity conditions:

$$f(t = 0,\mathbf{h}) = f_0(\mathbf{h})$$

(2.17a)

$$f(t,h_i = 0,h_{j \neq i}) = 0$$

(2.17b)

$$f(t,h_i \rightarrow \infty,h_{j \neq i}) = 0.$$

(2.17c)

The birth term σ^+ in Eq. (2.16) can be used to model the appearance of new crystals due to nucleation. Assuming, that the size and shape of nucleated crystals can be described by the state vector $\mathbf{h}_{\text{nuc}}$, the birth term σ^+ can be expressed as:

$$\sigma^+ = B_{\text{nuc}} \prod_{i=1}^{n} \delta(h_i - h_{i,\text{nuc}}) ,$$

(2.18)

with B_{nuc} denoting the nucleation rate and δ being the Dirac distribution. It has to be noted at this point, that the formulation of the PBE given in Eq. (2.16) constitutes a rather simple case

in the modeling of crystal shape dynamics, as Eq. (2.16) assumes that no faces disappear from – or reappear on the surface of any crystal of the population during growth or dissolution. As this assumption was fulfilled in the remainder of this work, further details on the modeling of the appearance or disappearance of crystal faces are not given here, but can for instance be found in Borchert and Sundmacher (2012b), Borchert (2012c) or Singh and Ramkrishna (2013).

In order to solve the PBE of Eq. (2.16), the method of moments (Hulburt 1964) was adopted in this work. In the bivariate case of KDP, a mixed moment $\mu_{i,j}$ of the CSSD is defined as:

$$\mu_{i,j} = \int\limits_0^\infty \int\limits_0^\infty h_1^i h_2^j \, f \, dh_1 dh_2 \,. \tag{2.19}$$

With this definition, the population balance can be transformed into a set of ordinary differential equations describing the dynamic evolution of the moments of the distribution. As the remainder of this work is mainly concerned with controlling the evolution of the seed crystal population, nucleation is (with the exception of Section 3.4) neglected. With this simplification and assuming that no crystals disappear due to complete dissolution, the dynamics of the mixed moments can be described by:

$$\frac{d\mu_{0,0}}{dt} = 0 \tag{2.20a}$$

$$\frac{d\mu_{i,j}}{dt} = iG_i\mu_{i-1,j} + jG_j\mu_{i,j-1}. \tag{2.20b}$$

As can be seen from the equations given above, only the evolution of some integral values (namely the moments) of the CSSD can be described by the method of moments. While this approach is computationally efficient, a precise reconstruction of the CSSD from a given set of moments is in general not possible. Due to the simplicity of the chosen model, the solution of Eq. (2.16) requires that the seed crystal distribution is translated through the internal coordinates (or rather through the geometrical state space) in an unaltered way. Hence, the evolution of the mean seed crystal shape, which can indeed be tracked with the moment model of Eq. (2.20), can be used to fully characterize the seed crystal distribution at any time during the crystallization process.

As can be seen from Eq. (2.20b), the derivative of $\mu_{i,j}$ is (apart from the growth rates **G**) only dependent on lower order moments, and hence, a closed set of ordinary differential equations can be obtained[6]. Thus, a finite set of moments can be used to describe the evolution of the CSSD without the necessity of any closure condition. In order to describe the dynamics of the crystallization process, the following set of moments, collected in the vector **μ**, was used:

---

[6] Note that the derivatives $d\mu_{i,j}/dt$ of a moment model derived from the population balance approach of Eq. (3.17) accounting also for growth rate dispersion, will be dependent on $\mu_{i,j}$ as well. Nevertheless, the moment model still constitutes a closed set of differential equations (see Zumstein and Rousseau (1987a, 1987b)).

$$\boldsymbol{\mu} = \left[\mu_{0,0}, \mu_{1,0}, \mu_{0,1}, \mu_{2,0}, \mu_{1,1}, \mu_{3,0}, \mu_{2,1}\right]^{\mathrm{T}}. \tag{2.21}$$

While the total number of crystals per suspension volume can be readily obtained from the 0th moment $\mu_{0,0}$, the mean crystal shape $\overline{\mathbf{h}}$ can be obtained from the first order moments according to:

$$\overline{\mathbf{h}} = \frac{\left[\mu_{1,0}, \mu_{0,1}\right]^{\mathrm{T}}}{\mu_{0,0}}. \tag{2.22}$$

The total crystal surface area and the total crystal volume are of particular importance for the model of the solute concentration and the suspension temperature. Both quantities can be derived from the second and third order moments $\mu_{2,0}$ and $\mu_{1,1}$ or $\mu_{3,0}$ and $\mu_{2,1}$ respectively. This is discussed in the following sections, where the models of the concentration and temperature of the solution is presented.

2.7.2 Solute Concentration

The solution of the PBE is, apart from the initial conditions, dependent on the kinetics of growth and dissolution, which are generally a function of the concentration and temperature of the liquid phase (see Chapter 3). Thus, Eq. (2.16) and Eqs. (2.20) are coupled to the dynamics of the solution temperature and the solute concentration. Hence, dynamic models for both quantities are required in order to fully predict the transient evolution of the CSSD.

Changes in the solution concentration during batch crystallization processes are generally the result of crystal growth or dissolution. As solute molecules are incorporated in (or dissolved from) the crystal lattice, mass transfer between the liquid and solid phase must take place. In order to model the mass transfer rate, and to derive an equation for the concentration profile over time, the volume of a single KDP crystal is considered first. This volume can be calculated from the geometrical state $\mathbf{h}$ according to Borchert (2012c) by:

$$V_{\text{cryst}} = 10.948 h_1^2 h_2 - 4.983 h_1^3. \tag{2.23}$$

Integrating this equation over the suspension volume V_{sus} and the entire CSSD, the total crystal volume can be obtained by

$$V_{\text{cryst,tot}} = V_{\text{sus}}\left[10.948\int_0^\infty\int_0^\infty h_1^2 h_2\, f dh_1 dh_2 - 4.983\int_0^\infty\int_0^\infty h_1^3\, f dh_1 dh_2\right], \tag{2.24}$$

which can be expressed through the definition of the moments of the distribution Eq. (2.19) as:

$$V_{\text{cryst,tot}} = V_{\text{sus}}\left(10.948\mu_{2,1} - 4.983\mu_{3,0}\right). \tag{2.25}$$

By balancing the mass of crystalline and dissolved KDP, and using the crystal density $\rho_{\text{KDP}} = 2338$ kg/m^3 (Ma 2002), the concentration can be expressed through the moments of the CSSD as:

$$w(t) = w(t = 0) - \frac{V_{sus}\rho_{KDP}}{m_{H_2O}} \left[10.948 \big(\mu_{2,1} - \mu_{2,1}(t=0) \big) - 4.983 \big(\mu_{3,0} - \mu_{3,0}(t=0) \big) \right]. \qquad (2.26)$$

The derivative of the concentration w with respect to time can be formulated on the basis of Eq. (2.26) and Eq. (2.20b) according to:

$$\frac{dw}{dt} = -\frac{V_{sus}\rho_{KDP}}{m_{H_2O}} \left[10.948 \frac{d\mu_{2,1}}{dt} - 4.983 \frac{d\mu_{3,0}}{dt} \right] \qquad (2.27a)$$

$$\frac{dw}{dt} = -\frac{V_{sus}\rho_{KDP}}{m_{H_2O}} \left[10.948 \big(2G_1\mu_{1,1} + G_2\mu_{2,0} \big) - 14.949 G_1\mu_{2,0} \right]. \qquad (2.27b)$$

Thus, the dynamic concentration changes can be expressed through an ordinary differential equation, which is dependent on the moments of the crystal distribution and can be integrated alongside with Eqs. (2.20).

2.7.3 Solution Temperature

The temperature of the solution influences the crystallization process in two different ways. As the growth and dissolution kinetics are generally temperature-dependent, the dynamics of the crystallization process is directly affected by the solution temperature (see also the results presented in the next chapter of this manuscript). In addition to this dependence, the supersaturation, and thus the driving force of the crystallization process, is a function of temperature through the solubility correlation of Eq. (2.2). Since the face-specific growth rates of a crystal typically depends in a nonlinear manner on supersaturation, control over the crystallization temperature, and thus over the supersaturation, offers a way for controlling the crystallization kinetics. Furthermore, the control of supersaturation through temperature control may open a direct pathway to control the final crystal shape of the crystallization process. This is the case if the dependencies of the face-specific growth rates on supersaturation differ among the individual face types (see for example Sections 3.1 and 3.2).

Changes of the solution temperature are mainly induces by (and in this work controlled through) the temperature of the thermostat which is connected to the double jacket of the crystallizer. Differences between the temperature of the double jacked, which is directly influenced by the thermostat temperature, and the crystallizer temperature trigger a heat flow which will consequently lead to temperature changes in the crystallizer as well as in the double jacked. To describe these dynamics, the crystallizer was modeled as an ideally mixed vessel. The double jacked was instead modeled as a cascade of two ideally mixed vessels, describing the temperatures of the ground element − (index G) and the side element of the jacked (index S), through which the mass flow of the thermostat $\dot{m}_{Th}$ was flowing (see Figure 2.16). The model of the double jacked was chosen to reproduce the residence time distribution within the jacked, which is of particular importance for the modeling of the
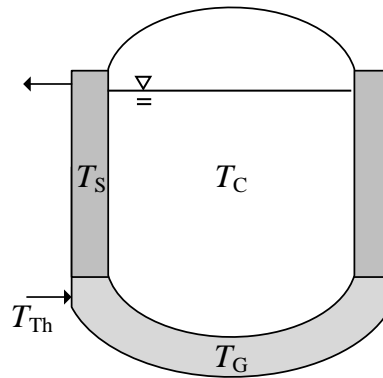
Figure 2.16: Schematic representation of the balance domains used to model the temperature dynamics in the crystallization vessel and its double jacked.

Table 2.1: Parameter values of Eqs. (2.28a), (2.28b) and (2.28c).

Symbol	Value	Unit	Symbol	Value	Unit
A_{CG}	0.0201	m²	k_{CG}	205.2	W/(m²K)
A_{CS}	0.0423	m²	k_{CS}	205.2	W/(m²K)
A_{GU}	0.0482	m²	k_U	29.3	W/(m²K)
A_{SU}	0.1409	m²	$c_{p,C}$	3.960*	kJ/(kgK)
m_C	variable	kg	c_{p,H_2O}	4.180	kJ/(kgK)
m_G	0.8959	kg	$\Delta\tilde{H}_{KDP}$	- 19.0	kJ/mol
m_S	2.2445	kg	$\tilde{m}_{KDP}$	0.1361	kg/mol
$\dot{m}_{Th}$	0.0508	kg/s	T_U	24	°C

* The heat capacity $c_{p,C}$ was determined for a saturated solution at a temperature of 40 °C.

supersaturation switches discussed in Section 4.3. Although this approach constitutes a rather coarse approximation of the real fluid dynamics in the double jacked, it was found to provide a good compromise between the model accuracy (see Figures 4.7 and 4.8 in Section 4.3 for examples) and computational efficiency. The dynamics of all three temperatures can be described by the following set of coupled differential equations:

$$\frac{dT_C}{dt} = \frac{k_{CG}A_{CG}}{m_C c_{p,C}}\left(T_G - T_C\right) + \frac{k_{CS}A_{CS}}{m_C c_{p,C}}\left(T_S - T_C\right) + \frac{\Delta\tilde{H}_{KDP}}{\tilde{m}_{KDP}m_C c_{p,C}}\frac{dm_{KDP}}{dt} \tag{2.28a}$$

$$\frac{dT_G}{dt} = \frac{\dot{m}_{Th}}{m_G}\left(T_{Th} - T_G\right) + \frac{k_{CG}A_{CG}}{m_G c_{p,G}}\left(T_C - T_G\right) + \frac{k_U A_{GU}}{m_G c_{p,G}}\left(T_U - T_G\right) \tag{2.28b}$$

$$\frac{dT_S}{dt} = \frac{\dot{m}_{Th}}{m_S}\left(T_{Th} - T_S\right) + \frac{k_{CS}A_{CS}}{m_S c_{p,S}}\left(T_C - T_S\right) + \frac{k_U A_{GU}}{m_S c_{p,S}}\left(T_U - T_S\right). \tag{2.28c}$$

The parameter values that are appearing in these differential equations were determined in preliminary experiments and are given in Table 2.1. Note that the coefficients of the heat transfers between the jacked ground and the crystallizer k_{CG} and between the jacked side and the crystallizer k_{CS} were assumed to be identical for the sake of identifiability.

An assessment of the accuracy of this temperature model is, for the sake of brevity, not given in this section, but can be found in Chapter 4 of this manuscript (particularly in Sections 4.2, 4.3 and 4.5). In general, a good agreement between modeled and measured temperature profiles was found throughout this work, which indicates the adequacy of the temperature model of Eq. (2.28).

Equation (2.28) constitutes, in conjunction with Eq. (2.27) and Eq. (2.20), a closed set of differential equations that can be used to describe the dynamics of the process variables that are governing the entire crystallization process, namely the solution temperature, the solute concentration and the state of the crystalline phase. However, these equations cannot be solved without the knowledge of the kinetics of crystallization, as these kinetics are appearing either explicitly (as in case of Eq. (2.20)) or implicitly (through the change of the dissolved solute mass dm_{KDP}/dt) in these equations. Therefore, the next chapter of this work is concerned with the determination and parameterization of the growth and dissolution kinetics, in order complete the model equations as well as to gain some insight into the mechanisms through which the kinetic phenomena of growth, nucleation and dissolution are controlled.

3. Crystallization Kinetics

A crystallization process is governed by solid liquid equilibria and crystallization kinetics. Through the solubility curve, thermodynamics define a maximal crystal yield at given start- and end-temperatures for a batch process, and possibly also the stable polymorph of the final crystal product. To design a seeded batch crystallization process based purely on thermodynamics, and thus without using any knowledge of the underlying crystallization kinetics, a simple approach can be derived from McCabes ΔL law (Mullin 2001). This approach relates the product crystal mass and size to the properties of the seed crystals via:

$$\frac{m_{\text{seed},0}}{m_{\text{P}}} = \left(\frac{L_{\text{seed},0}}{L_{\text{P}}} \right)^3 . \tag{3.1}$$

Since the total crystal mass m_{P} can be controlled by the selection of the initial and final crystallization temperature, a desired product crystal size L_{P} can be realized by an appropriate choice of the seed crystal mass $m_{\text{seed},0}$ and the seed crystal size $L_{\text{seed},0}$. However, Eq. (3.1) requires the absence of (primary or secondary) nucleation to be applicable. This is an assumption that can be quite restrictive, and may require low supersaturations during the crystallization process potentially resulting in rather low productivities. Furthermore, the applicability of Eq. (3.1) is limited to crystals whose shape can be completely described by one size coordinate alone and is thus not suited to design a crystallization process for achieving a desired shape distribution.

In order to predict the final CSSD of a crystallization process for faceted crystals, a detailed knowledge of the underlying crystallization kinetics is essential. The face-specific growth (and dissolution) rates determine both, the transient crystal shape evolution as well as the steady state crystal shape towards which the CSSD will evolve during a growth process. In conjunction with the nucleation kinetics, also the dynamics of the supersaturation depletion can be predicted. This in turn allows for the design and optimization of advanced process concepts. Therefore, this chapter is dedicated to the determination of these crystallization kinetics, exemplified on the system KDP-water.

In Section 3.1, the determination of the face-specific growth rates is presented. These growth rates were determined at constant levels of supersaturation and temperature, which allowed for a detailed analysis and description of the dependencies of the growth rates on both process variables. In particular the experimentally observed growth behavior of the prismatic {100}-faces $G_1(S)$ indicated, that growth was affected by the presence of impurities. Some further evidence for this phenomenon is given in Section 3.2, where the influence of impurities on the growth behavior is discussed in more detail. Furthermore, the growth rates are qualitatively described by the step pinning mechanism of Kubota and Mullin (1995) as a function of supersaturation in this section. In the final part of this section, the resulting growth kinetics $G_1(S)$ and $G_2(S)$ are used to obtain the region of crystal shapes that are attainable by pure growth processes. An analysis of this region with respect to the sensitivity

of attainable crystal shapes regarding variations in supersaturation and impurity concentrations is presented and used to derive a range of applicable supersaturation levels for the concept of growth-dissolution cycles.

In the experiments used for the determination of the growth kinetics, not only growth, but also a widening of the seed crystal shape distribution and significant secondary nucleation was observable. The widening of the seed crystal shape distribution is analyzed in Section 3.3, and is, in the absence of size dependent growth, explained by growth rate dispersion. It is shown, that the observations can be well explained by including dispersive second order terms in the morphological population balance. The growth rate diffusivities describing the dynamic CSSD widening are determined in this section, and a clear dependence of the growth rate diffusivities on the face specific growth rates is identified. The phenomenon of nucleation is discussed in Section 3.4 of this work. By analyzing the evolution of the 0th moment of the entire crystal population over time, it is shown that the source of newly born crystals is secondary nucleation. The observations are parameterized by an empirical power law approach, which accounts for the dependence of the nucleation rate on temperature, supersaturation and suspension density.

The face-specific dissolution kinetics of KDP are discussed in Section 3.5. As in the previously discussed case of growth, the kinetics were again determined at constant temperature and constant undersaturation. It was found, that both face types dissolve with essentially identical dissolution rates. The implications of this observation on the region of crystal shapes attainable by growth-dissolution cycles (presented in Chapter 4) are discussed. The final section 3.6 provides a brief summary of the key results of this chapter.

3.1 Growth Kinetics

As already pointed out in Sections 2.6 and 2.7, the knowledge of the face specific kinetics, especially growth kinetics, is crucial for the understanding of the dynamics of crystallization processes and for the design of processes towards a desired crystal shape distribution. The growth kinetics of faceted crystals have been extensively studied in single crystal cells (Davey 1982, Shekunov 1997, Ristic 2001, Nguyen 2014) or hot stage reactors (Ma 2012a, Ochsenbein 2015) for various crystal shapes. Although the evolution of complex crystal shapes can be tracked reliably with such measurement devices, the application of the obtained growth kinetics to batch crystallization processes is not straightforward. This is particularly due to the differences in fluid dynamics which can lead to differences in transport phenomena such as bulk diffusion and furthermore to crystal-crystal or crystal-wall collisions that may induce surface defects (Burton 1951) and/or lattice strain (Zacher 1995, Ristic 1997, Jones 1999), potentially altering the crystal growth rates. It is therefore more desirable to obtain the crystallization kinetics under real process conditions.

While methods for the determination of one-dimensional growth kinetics under real process conditions, such as video microscopy (Temmel 2016b), sieve analysis of samples (Temmel 2016b), desupersaturation experiments (Schöll 2007) or analysis of steady state MSMPR
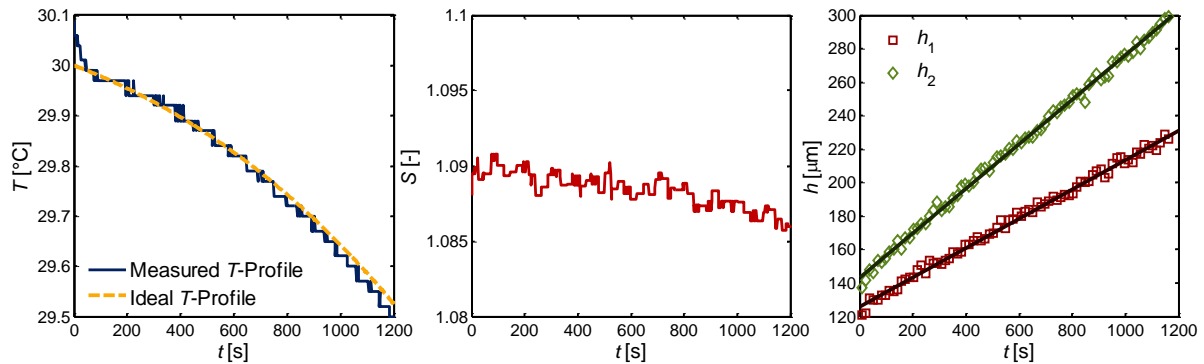
Figure 3.1: Estimation of face-specific growth rates of KDP at constant levels of supersaturation and approximately constant temperature; left: set point temperature profile (dashed yellow) and measured temperature profile (solid blue); middle: measured supersaturations; right: measured (marker) and regressed (solid lines) evolutions of the mean seed crystal shapes. Prismatic {100}-faces are indicated by red squares while pyramidal {101}-faces are indicated by green diamonds.

distributions (Randolph 1988) can be considered quite established, approaches for the determination of multidimensional growth rates are rare. Gunawan et al. (2002) and Borchert et al. (2014) used batch cooling crystallization experiments for the system KDP-water, to determine the face-specific growth rates which were parameterized by temperature-independent power law approaches. The growth kinetics of β L-glutamic acid crystals grown in water were determined by Ma et al. (2012b), again by cooling crystallization experiments, and by Ochsenbein et al. (2014), who applied desupersaturation experiments at different temperatures to describe the growth kinetics in crystal length and width as a function of supersaturation and temperature.

The face specific-growth kinetics of KDP were determined in this work for constant supersaturation. Once the seed crystal population had been added to the solution, a temperature control program was started that allowed for a growth process at constant supersaturation[7]. Due to the rather low seed loading that was used in all experiments (1.0 g of seed material), the resulting temperature gradients were small and the maximal temperature difference between start and end time did not exceed 0.5 °C. Hence, also temperature was considered to be approximately constant during the growth experiments.
Typical temperature and supersaturation profiles of one growth experiment are depicted in Figure 3.1. As can be seen, the set-point temperature (yellow dashed line, left) exhibited a concave shape (due to the increase in the crystals surface area over time) and could be realized extremely well (solid blue). This resulted in an almost constant supersaturation profile (middle) over time. The evolution of the mean seed crystal shape over time, which was measured with the observation techniques presented in Section 2.4, is depicted in the

---

[7] The temperature control program for a constant supersaturation level was based on Eqs. (4.8) and (4.15) of Section 4.2 of this work. Note that in order to apply Eq. (4.15), the growth kinetics need already to be known. Since these kinetics are to be determined through the experiments that are described in this section, they could naturally not be used for Eq. (4.15). Instead, kinetics which were obtained in preliminary experiments were used for the computation of the temperature profiles.
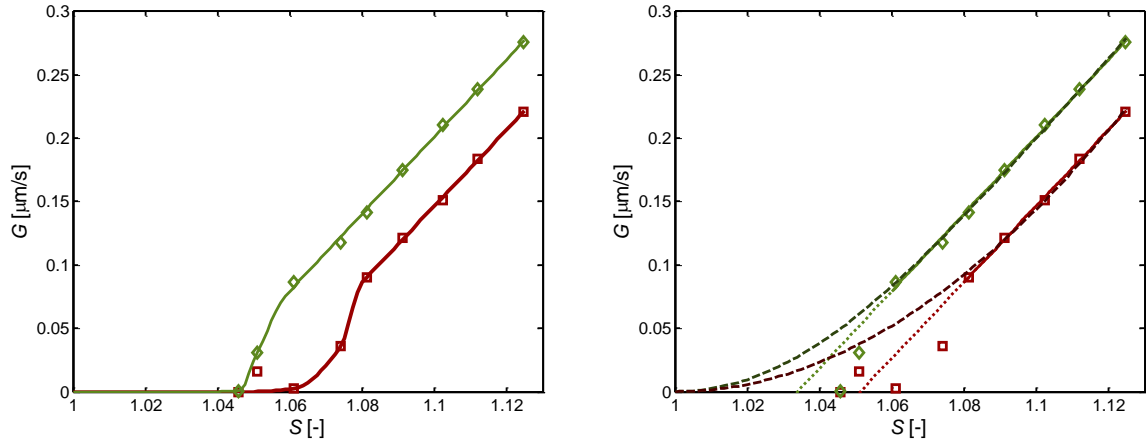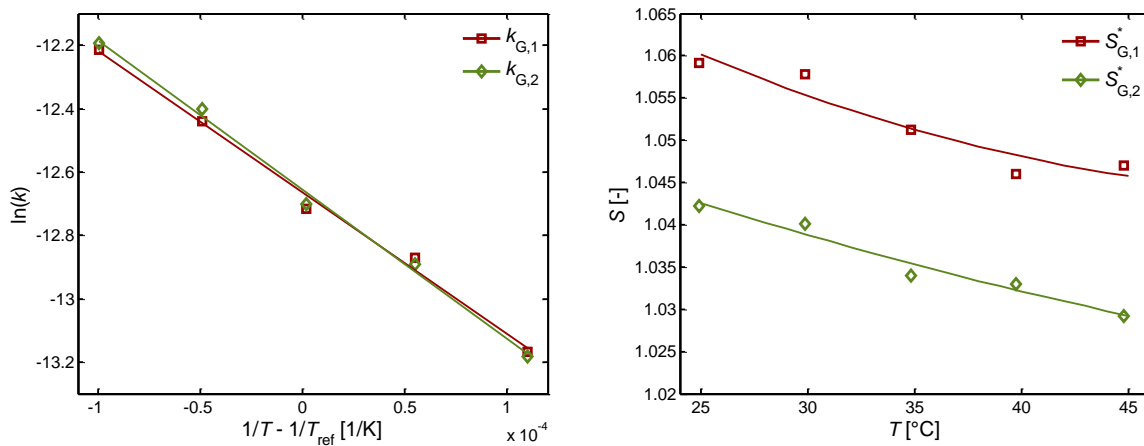
Figure 3.2: Supersaturation dependence of the growth rates of the {100}-faces (red squares) and the {101}-faces (green diamonds) determined for a set-point temperature of T = 35 °C; left: measurements with interpolations; right: measurements with fitted linear kinetics (solid), extrapolated linear kinetics (dotted) and fitted BCF kinetics (dark, dashed).

right part of Figure 3.1. Due to the almost constant supersaturation and temperature profiles, the slopes of the evolutions $h_1(t)$ and $h_2(t)$ were essentially constant. This behavior, which was also confirmed by the other growth experiments, indicates that growth rates are not size dependent for both face types considered. Hence, the growth velocities G_i for the individual crystal faces could be obtained by linear regressions over the observed mean seed crystal shape evolutions, using the growth rate definition of Eq. (2.9). The procedure described above was repeated for different supersaturation levels between 0.03 and 1.13 as well as for different temperatures between 25 °C and 45 °C.

The dependencies of the obtained growth rates on supersaturation are exemplarily shown in Figure 3.2 for a set-point temperature of 35 °C. Generally, three different regions can be identified here. At low supersaturation levels, both face types show growth rates which were essentially zero with respect to the measurement precision (approximately 1 nm/s, see also Table 3.1) of the video microscope. Such a behavior is well known for KDP crystals in the presence of impurities that are affecting the growth behavior and is typically referred to as death zone (Sangwal 2007). Particularly the growth of the prismatic {100}-faces is known to be strongly affected by the presence of trivalent metal ions like Fe^{3+}, Al^{3+} or Cr^{3+} (Rashkovich 1997, Thomas 2004). A detailed discussion on the influence of impurities on the growth behavior of KDP is given in Section 3.2 of this work. A second growth region can be identified at intermediate supersaturations, where the growth rates are strongly increasing with supersaturation. At higher supersaturation levels, a linear dependence of the growth rates on supersaturation is visible. The latter behavior is qualitatively in accordance with the classical BCF theory (Burton 1951), which predicts a dependence of the growth rates on supersaturation according to:

$$G_{\mathrm{BCF}} = k_{\mathrm{BCF}} \frac{(S-1)^2}{\sigma_1} \tanh\left(\frac{\sigma_1}{S-1}\right), \tag{3.2}$$

Figure 3.3: Temperature dependence of the face-specific growth kinetics of KDP: left: Arrhenius plot of the pre-exponential factors $k_{G,i}$ over the temperature; right; temperature dependence of the threshold supersaturations $S^{*}_{G,i}$ defined by Eq. (3.4). {100}-faces are indicated by red squares and {101}-faces are indicated by green diamonds.

with a temperature dependent constant k_{BCF} , and a critical supersaturation σ_1. According to this equation, the growth rate increases quadratically at low supersaturations and linearly at higher supersaturations, $(S-1) > \sigma_1$ with:

$$\frac{dG_{BCF}}{dS} \approx \text{const.}$$ (3.3)

The BCF approach, Eq. (3.2), was fitted to the linear part of the growth kinetics, and the results are shown as dashed lines in the right part of Figure 3.2. As can be seen, good agreement between measurements and model prediction were obtained in the considered supersaturation range. Despite this good agreement, the growth kinetics were, for the sake of simplicity, parameterized in this work by a linear approach:

$$G_i = k_{G,i}\left(S - S^{*}_{G,i}\right),$$ (3.4)

with a temperature dependent growth rate constant $k_{G,i}$ and a threshold supersaturation $S^{*}_{G,i}$. As can be seen from Figure 3.2, the growth laws of Eq. (3.2) and Eq (3.4) lead to almost identical results in the considered supersaturation ranges, and can thus be considered as equivalent in these supersaturation regions.

The procedure for determining the supersaturation dependence of the growth kinetics was repeated for all set-point temperatures in a range from 25 °C to 45 °C. A similar behavior as depicted in Figure 3.2 was observed for all temperatures, and hence, estimates for the parameters $k_{G,i}$ and $S^{*}_{G,i}$ could be obtained by fitting Eq. (3.4) to the measured growth rates of the linear part of the kinetics. The resulting values for the growth rate constants $k_{G,i}$ are shown in Figure 3.3 in an Arrhenius plot. As can be seen, the growth rate constants for both face types have similar values for all investigated temperatures, indicating similar slopes for both growth rates $G_1(S)$ and $G_2(S)$, and are decreasing linearly in the Arrhenius plot. Hence, the temperature dependence of the growth rate constant was parameterized by the approach:
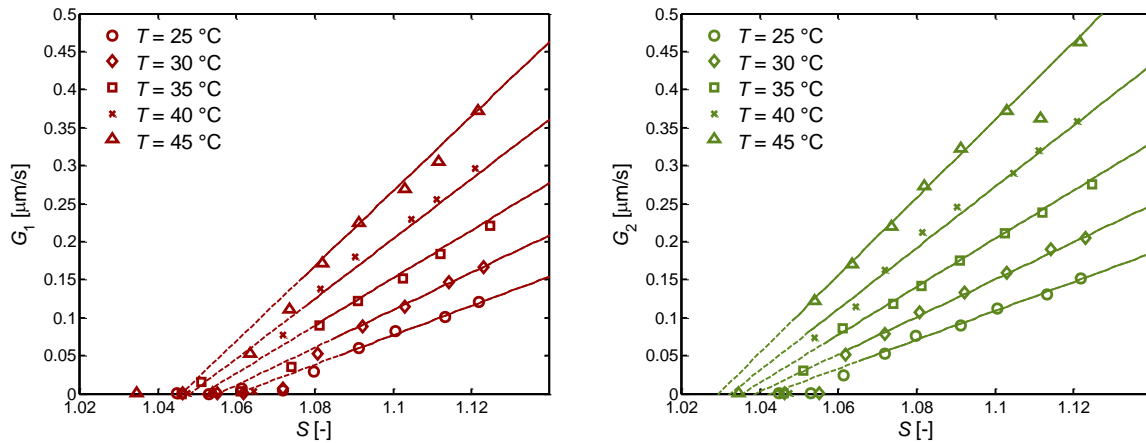
Figure 3.4: Face-specific growth rates of KDP as a function of supersaturation and temperature; left: prismatic {100}-faces; right: pyramidal {101}-faces. Measured growth rates for different temperatures are indicated by the markers in the upper left corners. Dashed lines indicate the kinetics determined with Eqs. (3.4) to (3.6), while solid lines indicate the supersaturation regions in which the kinetics are valid.

$$k_{\mathrm{G},i} = k_{0,\mathrm{G},i} \exp\left(-\frac{E_{\mathrm{A,G},i}}{R}\left(\frac{1}{T} - \frac{1}{T_{\mathrm{ref}}}\right)\right). \tag{3.5}$$

The pre-exponential factors $k_{0,\mathrm{G},i}$ and the activation energies $E_{\mathrm{A,G},i}$ of this approach were determined by linear regression and are given in Table 3.2 together with their confidence intervals. Apart from the growth rate constants, also the threshold supersaturations $S^{*}_{\mathrm{G},i}$ showed a temperature dependent behavior, as depicted in Figure 3.3. A clear decrease of the obtained values for $S^{*}_{\mathrm{G},i}$ can be observed with increasing temperatures which is qualitatively in accordance to literature on crystal growth in the presence of impurities (Kubota 2001). The dependence of $S^{*}_{\mathrm{G},i}$ on temperature is quantified in this work by an empirical second-order polynomial:

$$S^{*}_{\mathrm{G},i} = s_{1,\mathrm{G},i} + s_{2,\mathrm{G},i}T + s_{3,\mathrm{G},i}T^{2}, \tag{3.6}$$

with the empirical parameters $s_{j,\mathrm{G},i}$, given in Table 3.2 together with their confidence intervals. By inserting Eqs. (3.5) and (3.6) into Eq. (3.4), the face-specific growth rates G_i can be expressed as a function of supersaturation and temperature:

$$G_{i} = k_{0,\mathrm{G},i} \exp\left(-\frac{E_{\mathrm{A,G},i}}{R}\left(\frac{1}{T} - \frac{1}{T_{\mathrm{ref}}}\right)\right)\left(S - S^{*}_{\mathrm{G},i}\right). \tag{3.7}$$

The comparison of the growth rates obtained with Eq. 3.7 (equipped with the parameters from Table 3.2) to all measured growth rates is shown in Figure 3.4. As can be seen, the overall growth behavior of both face types could be fitted well by Eq. (3.7) in cases where the supersaturation was high enough to overcome the influences of impurities on the growth rates. Only the growth rate of the {101}-faces at a supersaturation of $S = 1.11$ and a temperature of $T = 45$ °C deviates significantly from the determined kinetics. However, as this growth rate was even lower than for $S = 1.10$ at the same temperature, this measurement should be rather considered an outlier.

Table 3.1: Growth rates and growth rate diffusivities (see Section 3.3) as well as their confidence intervals (Ci, given for a significance level of 95%) that were determined in individual experiments.

$\bar{T}$ [°C]	$\bar{S}$ [-]	{100}-faces				{101}-faces			
		G_1 [µm/s]	$Ci - G_1$ [µm/s]	d_1 [µm²/s]	$Ci - d_1$ [µm²/s]	G_2 [µm/s]	$Ci - G_2$ [µm/s]	d_2 [µm²/s]	$Ci - d_2$ [µm²/s]
24.94	1.045	0.000	± 0.001	0.013	± 0.013	0.000	± 0.001	0.005	± 0.011
25.02	1.053	0.000	± 0.001	0.012	± 0.014	0.000	± 0.001	0.001	± 0.012
24.99	1.061	0.007	± 0.001	0.011	± 0.015	0.024	± 0.001	0.101	± 0.017
24.99	1.072	0.004	± 0.001	0.048	± 0.020	0.052	± 0.001	0.158	± 0.028
24.98	1.080	0.029	± 0.002	0.237	± 0.043	0.076	± 0.002	0.277	± 0.039
24.88	1.091	0.060	± 0.002	0.330	± 0.034	0.090	± 0.001	0.295	± 0.050
24.81	1.101	0.083	± 0.002	0.426	± 0.050	0.113	± 0.001	0.255	± 0.047
24.76	1.113	0.101	± 0.003	0.520	± 0.071	0.131	± 0.003	0.283	± 0.061
24.78	1.122	0.121	± 0.003	0.607	± 0.083	0.151	± 0.003	0.350	± 0.079
29.98	1.046	0.0004	± 0.001	0.022	± 0.020	0.001	± 0.001	-0.008	± 0.015
30.00	1.055	0.0002	± 0.001	-0.002	± 0.013	0.001	± 0.001	-0.016	± 0.015
29.99	1.062	0.0008	± 0.001	0.039	± 0.023	0.051	± 0.001	0.109	± 0.024
29.93	1.072	0.0071	± 0.002	0.094	± 0.040	0.079	± 0.002	0.162	± 0.043
29.86	1.081	0.0520	± 0.002	0.379	± 0.043	0.107	± 0.001	0.239	± 0.048
29.87	1.092	0.0888	± 0.003	0.451	± 0.081	0.133	± 0.003	0.339	± 0.078
29.81	1.103	0.1150	± 0.006	0.544	± 0.148	0.159	± 0.004	0.313	± 0.128
29.48	1.114	0.1472	± 0.003	0.704	± 0.074	0.190	± 0.002	0.395	± 0.072
29.66	1.123	0.1667	± 0.004	0.723	± 0.124	0.204	± 0.004	0.348	± 0.092
34.93	1.046	0.0000	± 0.001	-0.001	± 0.012	0.001	± 0.000	0.000	± 0.011
34.90	1.051	0.0159	± 0.002	0.043	± 0.057	0.031	± 0.004	0.190	± 0.070
34.87	1.061	0.0026	± 0.002	0.064	± 0.038	0.086	± 0.002	0.178	± 0.038
34.84	1.074	0.0358	± 0.002	0.267	± 0.050	0.118	± 0.003	0.296	± 0.063
34.92	1.081	0.0899	± 0.004	0.509	± 0.118	0.141	± 0.003	0.422	± 0.111
34.87	1.091	0.1213	± 0.003	0.638	± 0.100	0.175	± 0.003	0.411	± 0.075
34.72	1.102	0.1511	± 0.004	0.858	± 0.144	0.211	± 0.004	0.427	± 0.100
34.69	1.112	0.1841	± 0.004	0.860	± 0.128	0.239	± 0.004	0.518	± 0.089
34.67	1.125	0.2208	± 0.005	1.166	± 0.178	0.276	± 0.003	0.576	± 0.187
39.80	1.047	0.0003	± 0.001	-0.006	± 0.019	0.001	± 0.001	0.005	± 0.014
39.90	1.054	0.0008	± 0.002	0.112	± 0.047	0.074	± 0.002	0.157	± 0.047
39.82	1.064	0.0028	± 0.001	0.001	± 0.052	0.114	± 0.002	0.227	± 0.053
39.70	1.072	0.0768	± 0.002	0.580	± 0.082	0.163	± 0.003	0.446	± 0.078
39.66	1.082	0.1375	± 0.004	0.803	± 0.118	0.213	± 0.004	0.523	± 0.101
39.78	1.090	0.1798	± 0.004	0.826	± 0.121	0.245	± 0.004	0.588	± 0.113
39.63	1.105	0.2299	± 0.009	1.049	± 0.172	0.290	± 0.007	0.474	± 0.165

Table 3.1: Continued

$\bar{T}$ [°C]	$\bar{S}$ [-]	{100}-faces				{101}-faces			
		G_1 [μm/s]	Ci − G_1 [μm/s]	d_1 [μm²/s]	Ci − d_1 [μm²/s]	G_2 [μm/s]	Ci − G_2 [μm/s]	d_2 [μm²/s]	Ci − d_2 [μm²/s]
39.74	1.111	0.2556	± 0.009	1.109	± 0.283	0.320	± 0.008	0.268	± 0.218
39.80	1.121	0.2967	± 0.012	1.203	± 0.347	0.358	± 0.006	0.427	± 0.297
44.93	1.035	0.000	± 0.001	-0.012	± 0.018	0.001	± 0.001	-0.020	± 0.015
-*	-*	-	-	-	-	-	-		-
44.88	1.054	0.001	± 0.002	0.061	± 0.053	0.122	± 0.003	0.212	± 0.053
44.82	1.063	0.053	± 0.003	0.391	± 0.076	0.171	± 0.003	0.415	± 0.063
44.71	1.074	0.110	± 0.003	0.789	± 0.114	0.219	± 0.003	0.593	± 0.092
44.71	1.082	0.172	± 0.004	0.899	± 0.124	0.273	± 0.003	0.619	± 0.089
44.71	1.091	0.225	± 0.005	1.222	± 0.177	0.324	± 0.006	0.645	± 0.160
44.69	1.103	0.269	± 0.007	1.589	± 0.177	0.372	± 0.008	0.758	± 0.160
44.78	1.112	0.305	± 0.012	1.182	± 0.259	0.362	± 0.007	0.445	± 0.227
44.77	1.122	0.373	± 0.011	1.695	± 0.391	0.462	± 0.008	0.742	± 0.354

* The results of the experiment are depicted in Figure 3.9 and discussed in more detail in Section 3.2. As the crystal shape evolution exhibited a significant time-dependence, no values for the growth rates and growth rate diffusivities were determined for this experiment.

Table 3.2: Parameter values of Eq. (3.5) and Eq. (3.6) for a reference temperature T_{ref} of 35 °C. Confidence intervals are given for a significance level of 95%.

Symbol	{100}-faces		{101}-faces	
	Value	Confidence interval	Value	Confidence interval
$\ln(k_{0,G,i})$ [-]	-12.667	± 0.049	-12.657	± 0.042
$k_{0,G,i}$ [m/s]	3.155×10^{-6}	$[3.004,\ 3.314] \times 10^{-6}$	3.184×10^{-6}	$[3.052,\ 3.322] \times 10^{-6}$
$E_{A,G,i}$ [kJ/mol]	37.048	± 5.491	39.136	± 4.741
$s_{1,G,i}$ [-]	1.0513	± 0.0075	1.0353	± 0.0044
$s_{2,G,i}$ [°C⁻¹]	-7.187×10^{-4}	$± 6.915 \times 10^{-4}$	-6.658×10^{-4}	$± 4.031 \times 10^{-4}$
$s_{3,G,i}$ [°C⁻²]	1.706×10^{-5}	$± 11.735 \times 10^{-5}$	5.906×10^{-6}	$± 68.40 \times 10^{-6}$

Furthermore, Figures 3.2 and 3.4 show that the pyramidal {101}-faces are growing faster than the prismatic {100}-faces for all considered supersaturation and temperature levels. Hence, the relative growth rate

$$G_{rel} = \frac{G_1}{G_2} \tag{3.8}$$

is always below 1. At lower supersaturation values, it is possible that only the pyramidal {101}-faces exhibit a significant growth rate, while the growth rate of the prismatic {100}-faces is essentially zero, see for example $S = 1.06$ in Figure 3.2. Hence, crystal growth under these conditions leads to elongated crystal shapes, as depicted in Figure 3.5, as the pyramidal
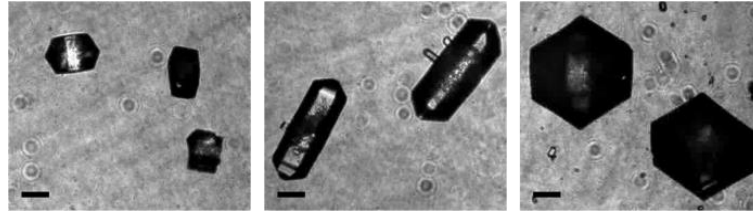
Figure 3.5: Different crystal shapes of KDP obtained from growth: left: seed crystals; middle; elongated crystal shapes resulting from growth at intermediate supersaturations (S = 1.074, T = 35 °C); right: compact crystal shapes obtained from growth at high supersaturations (S = 1.125, T = 35 °C). Scale bars in the lower left corners correspond to 200 µm.

{101}-faces can be grown almost exclusively. Conversely, at high supersaturation levels, both face types are growing with similar velocities, which results in G_{rel} approaching the value of one. If the seed crystals have a compact shape, or the growth time is sufficiently long, these similar growth rates result in similar face distances h_1 and h_2 and therefore in rather compact crystal shapes as shown in Figure 3.5. Hence, the crystal shapes that can be obtained from growth range from elongated shapes at low supersaturation to compact crystal shapes at high supersaturation. Such a behavior was already reported by Yang et al. (2006) and Borchert et al. (2014), and was clearly confirmed in this work. The kinetics determined in this work indicate however, that it is not possible, to obtain octahedral crystal shapes exposing only the pyramidal {101}-faces on the outer crystal surface. In order to grow such shapes, a relative growth rate of $G_{rel} > 1.465$ would be required, see Borchert (2012c) for details. In the investigated supersaturation and temperature range however the relative growth rate was always below one. Also extrapolating the kinetics of this work towards higher supersaturation values and higher or lower temperatures does not predict the existence of growth conditions that would lead to a fulfillment of $G_{rel} > 1.465$.

The face specific growth kinetics of KDP have also been investigated by Borchert et al. (2014) and Gunawan et al. (2002), and the results of both publications are used here for comparison. Both authors used temperature independent power law approaches to quantify the supersaturation dependence of the growth rates:

$$G_{1,\text{Borchert}} = 643.2 \times (S-1)^{3.89} \tag{3.9a}$$

$$G_{2,\text{Borchert}} = 2.07 \times (S-1)^{1.23} \tag{3.9b}$$

$$G_{1,\text{Gunawan}} = 6.105 \times (S-1)^{1.48} \tag{3.9c}$$

$$G_{2,\text{Gunawan}} = 36.811 \times (S-1)^{1.74}, \tag{3.9d}$$

where all growth rates are given in the unit µm/s. Note, that the original kinetics of Gunawan et al. were published by considering the total width and height of the KDP crystals to characterize the crystal shape. For details about the transformation of these internal coordinates to the framework of the **h**-representation see Borchert (2012c). To compare the kinetics obtained in this work with the kinetics of Borchert et al. (2014), a temperature of 35 °C was used, as this represents the mean temperature of the growth experiments described by Borchert et al. The comparison to the growth kinetics of Gunawan et al. (2002) was
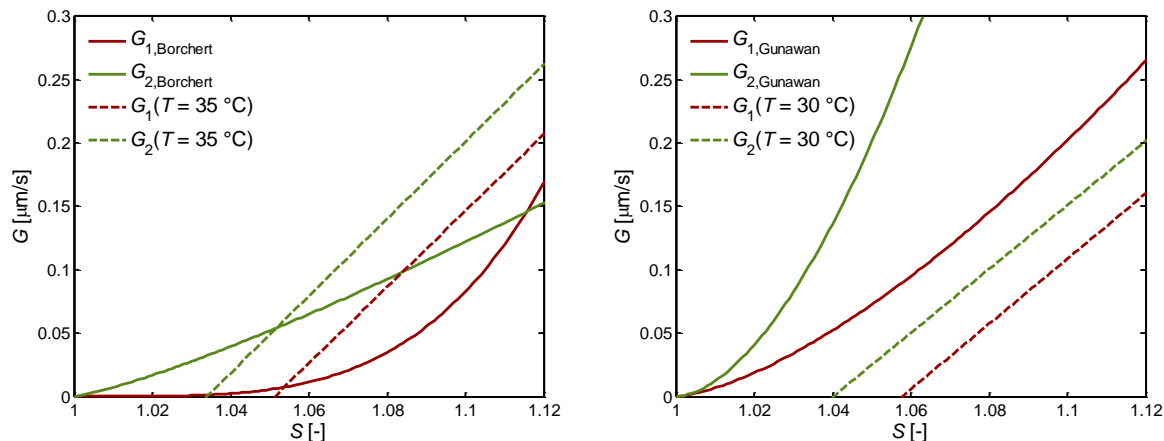
Figure 3.6: Comparison of the growth kinetics determined in this work (dashed lines) with literature data (solid lines); left: kinetics published by Borchert et al. (2014); right: kinetics published by Gunawan et al. (2002).

performed for a temperature of 30 °C. While the kinetics that were determined in this thesis are somewhat faster than the ones published Borchert et al. (2014), see Figure 3.6, they are slower than the kinetics published by Gunawan et al. (2002). This is particularly true for the growth kinetics of the pyramidal {101}-faces of Gunawan et al., which are almost one order of magnitude faster than the kinetics that were determined in this work. This underlines the importance of determining the crystallization kinetics under the actual process conditions to account for the fluid dynamics as well as impurity concentrations in the solution. Particularly the latter aspect is expected to have significant influence on the crystal growth rate and is therefore discussed in more detail in the next section of this work.

3.2 Influence of Impurities on the Growth Kinetics of KDP

Impurities in a crystallization process are often considered to be an undesired phenomenon, as the impurity molecules can adsorb on kink sites of the crystal surface, and thereby hinder the incorporation of new solute molecules into the crystal lattice. In this manner, the crystal growth rates can be decreased by the presence of impurities and in the extreme case, growth can be completely stopped. This effect would naturally result in prolonged growth times, and furthermore potentially increase the risk of spontaneous nucleation, as supersaturation may not be depleted fast enough to maintain the crystallization process within the metastable zone. However, as the adsorption of impurity molecules is strongly related to the properties of the surface on which the molecules are adsorbed, specifically tailored impurities – in this context typically referred to as additives – offer a way for crystal shape control. As the slowest growing crystal faces are the most prominent faces on the outer crystal surface, slowing down the growth rate of a specific crystal face gives direct control over the final crystal shape.

If such additives are known for a specific crystalline substance, their usage represents a popular technique for crystal shape control, provided that constraints on crystal purity and
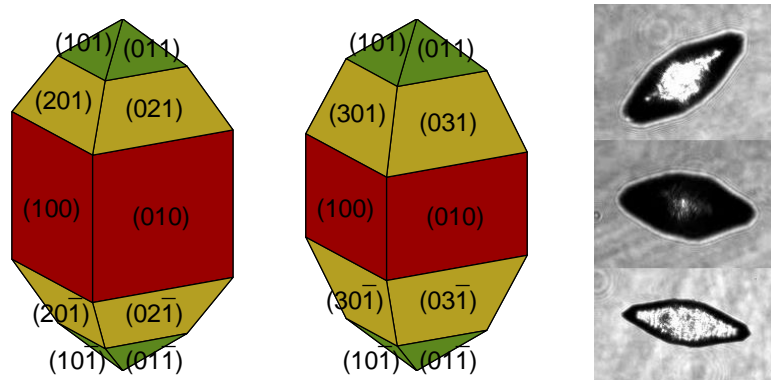
Figure 3.7: Tapered growth of KDP; left: KDP shape exhibiting {201}-faces in addition to the typical {100} and {101}-faces; middle: KDP shape with additional {301}-faces; right: micrographs of experimentally observed crystals that were undergoing tapered growth.

surface – or solid state properties can be met. For example, urea is known to crystallize from water in crystals with a needle-like shape, exhibiting extremely high aspect ratios. The addition of traces of biuret however, reduces growth in the [001]-direction significantly, resulting in crystals with a much smaller aspect ratio (Davey 1986). It is beyond the scope of this work to review the entire field of crystal shape control via additives. For more details, the reader is referred to the compilation of Nývlt and Ulrich (1995) and references therein as well as to the textbook of Sangwal (2007).

The growth kinetics of KDP are known to be influenced by numerous different additives. For example Nývlt and Ulrich (1995) compiled a list of about 30 different ions affecting the growth of KDP crystals. Interestingly, the majority of the investigated additives are adsorbing on the prismatic {100}-faces, among them trivalent metal ions like Fe^{3+}, Al^{3+} or Cr^{3+} as well as bivalent metal ions like Ba^{2+}, Ca^{2+} or Cu^{2+} (Nyvlt 1995, Rashkovich 1997, Zaitseva 1999, Thomas 2004, Sangwal 2007). Additionally, Fu et al. (1999) were investigating additives that were primarily influencing the growth rates of the pyramidal {101}-faces. They found, that by the addition of 100 ppm sodium metaphosphate, closed octahedral crystal shapes exhibiting only pyramidal {101}-faces on the outer crystal surface can be obtained.

Another interesting phenomenon related to the shape control of KDP via additives was observed by Mullin et al. (1970), and is referred to as tapered growth. Here, steps of the {100}-faces are accumulating on the edge between {100} and {101}-faces in a regular pattern, resulting in the formation of macroscopic {h01}-faces on the outer crystal surface. The resulting crystal shape is illustrated schematically in Figure 3.7 with either {201} or {301}-faces, together with experimentally observed crystal shapes, which were subject to tapered growth.

To verify whether the growth of KDP was indeed influenced by impurities in the experiments described in the previous section, the growth experiments for a set point temperature of $T = 35\,°C$ were repeated with KDP raw material purchased from Grüssing instead of the material purchased from Roth. The resulting growth kinetics are shown in Figure 3.8. As can be seen, the influence of the raw material on the growth behavior of the pyramidal {101}-faces is
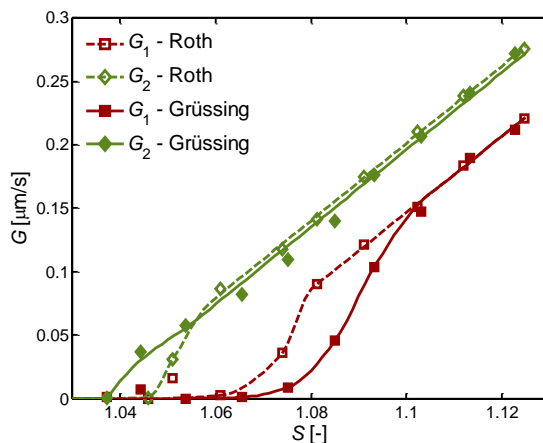
Figure 3.8: Growth kinetics obtained from different raw materials; solid, filled markers: KDP purchased from Grüssing (purity ≥ 99.5 %); dashed, empty markers: KDP purchased from Roth (purity ≥ 98 %).

rather small, but noticeable at low supersaturation levels, e.g., at $S \leq 1.05$. Growth of the prismatic {100}-faces is, however, strongly affected by the raw material used. The dead zone in which no significant growth occurs is even more enlarged for the material purchased from Grüssing, and also the intermediate supersaturation region, in which the growth rate increases strongly, is significantly broader. Only at high supersaturation values of $S \geq 1.10$, the effect of the raw material is diminishing. This suggests that the growth process in this supersaturation region is not influenced by the chemical composition of the solution, which in turn supports the application of the linear approximation of the growth kinetics by Eq. (3.4) to characterize the growth kinetics of KDP independently of the impurity concentration.

To describe the effects of impurities on the growth behavior of KDP that was observed in this work on a quantitative basis, the model for the step-pinning mechanism, proposed by Kubota and Mullin (Kubota 1995, Kubota 2001) was employed, and is briefly summarized here. For a more detailed description of the model, the reader is referred to the review of Kubota (2001). The model assumes that the displacement of a step on the crystal surfaces is hindered – or pinned – by the adsorption of impurity molecules on the kink sites of this step. In this case, the step is forced to curve around these blocked adsorption sites, and the average displacement velocity of the step v decreases according to:

$$\frac{v}{v_0} = 1 - \alpha\theta .$$ (3.10)

In this equation, v_0 denotes the step velocity in a pure solution, θ represents the coverage of active kink sites by impurity molecules and α represents an effectiveness factor of the impurity molecule. If the term $\alpha\theta$ is equal to zero, growth will be unaffected by the presence of impurities. If however, $\alpha\theta > 0$, the step velocity decreases compared to v_0, and if $\alpha\theta \geq 1$, growth is completely inhibited. If the adsorption of impurity molecules is fast compared to the frequency with which new kink sites are created on the step, the surface coverage θ can be replaced by the equilibrium coverage θ_{eq}, which can be obtained from an appropriate adsorption isotherm. In this case, the average step velocity will be constant with respect to
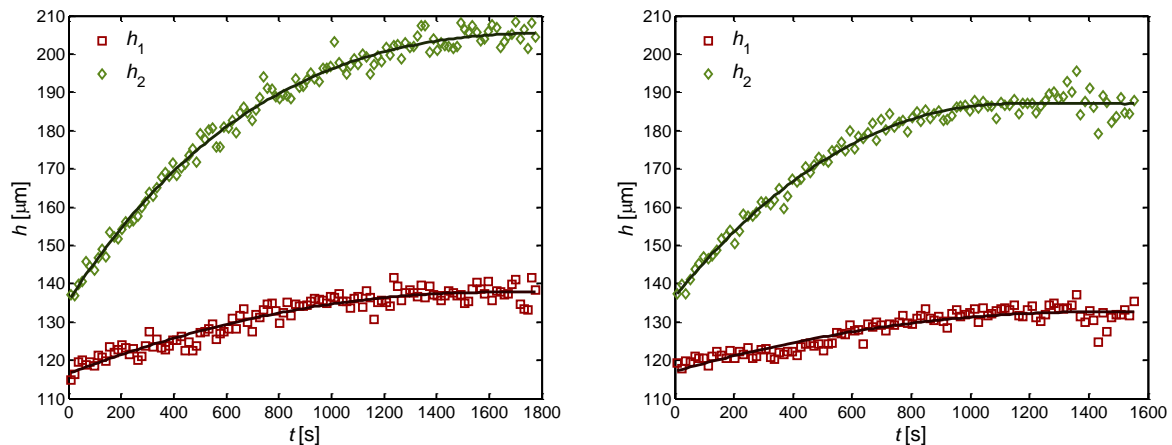
Figure 3.9: Time dependent growth of KDP crystals at a set-point temperature of T = 45 °C, and a supersaturation of S = 1.045 (left) and S = 1.039 (right). Measured mean seed crystal shapes are indicated by markers, and solid lines represent the fitted time dependent growth rates obtained from Eq. (3.12).

time. If, however, adsorption proceeds slowly compared to the formation of new kink sites, the surface coverage can be expressed as a function of time using the Langmuir adsorption mechanism. At non-equilibrium conditions, this leads to the following dynamics of the site coverage (Kubota 2001):

$$\theta = \theta_{eq}\left(1 - \exp\left(-\frac{t}{\tau}\right)\right). \tag{3.11}$$

Consequently, also the step velocity – and thus the growth rate of the face – is time dependent according to:

$$\frac{v}{v_0} = 1 - \alpha\theta_{eq}\left(1 - \exp\left(-\frac{t}{\tau}\right)\right). \tag{3.12}$$

Hence, the step velocity will asymptotically approach $v_0(1-\alpha\theta_{eq})$, if $\alpha\theta_{eq} \leq 1$, while growth stops completely at a critical time t_c, if $\alpha\theta_{eq} > 1$. The latter phenomenon was clearly observed in a growth experiment at T = 45 °C and S = 1.045, as well as in one repetition experiment under similar conditions. The experimentally obtained mean crystal shape evolutions for both experiments are depicted in Figure 3.9. As can be seen, both crystal face types grew at the initial phase of the experiments, but the growth rates decreased over time until growth essentially stopped after 1400 seconds and 1000 seconds, respectively. For a quantitative description of these observations, Eq. (3.12) was regressed to the experimental data by assuming that the face growth rates are linearly dependent on the step velocities. The resulting model fits are shown as solid lines in Figure 3.9. As depicted, the step pinning mechanism with a slow impurity adsorption process is capable of reproducing the experimentally observed crystal shape evolutions very well. Hence, the interpretation that growth of KDP was indeed influenced by impurities in this work is supported by the experimental observations shown in Figure 3.9 together with Eq. (3.12).

In a further extension of the model for the step-pinning mechanism, Kubota et al. (2000) considered the effect of supersaturation on the growth kinetics in the presence of impurities.
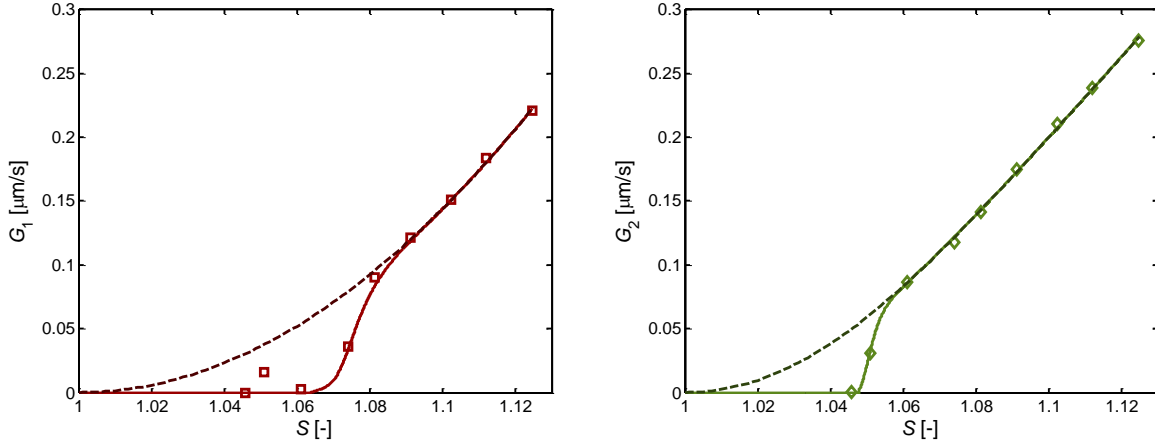
Figure 3.10: Supersaturation dependence of the face-specific growth rates of KDP in the presence of impurities assuming the non-equilibrium adsorption model of Eq. (3.12) (solid lines); left: growth rates of the prismatic {100}-faces; right: growth rates of the pyramidal {101}-faces. Dashed lines correspond to the BCF growth kinetics of Eq. (3.2), and markers represent the measured growth rates for a set-point temperature of $T = 35\,°C$.

The authors assumed the factor $\alpha\theta_{eq}$ to be inversely proportional to supersaturation according to:

$$\alpha\theta_{eq} = \frac{c_1}{S-1},\tag{3.13}$$

with the constant c_1 being dependent on temperature as well as on the impurity concentration. Furthermore, also the time constant τ was considered to be a function of supersaturation. This dependency was expressed by the empirical correlation

$$\tau = \exp(c_2(S - c_3)),\tag{3.14}$$

where c_2 and c_3 are constants. Inserting Eqs. (3.13) and (3.14) into (3.12) yields the step velocity v as a function of both, time and supersaturation in the presence of impurities.

The resulting equation was used to reproduce the growth kinetics obtained in this work and discussed in Section 3.1. To this end, only the growth rates that were determined for a set-point temperature of 35 °C are discussed here, as the growth phases in the cyclic growth-dissolution experiments (presented in Chapter 4) were conducted at this temperature. Eq. (3.12) was evaluated at the time point $t = 2000$ s to ensure that the simulated growth rates achieved their equilibrium value (compare to Figure 3.9). It was furthermore assumed that the growth rates G_i are linearly dependent on the step velocities v_i and that the supersaturation dependencies of the growth rates $G_{0,i}$ of the pure solution can be expressed by the BCF kinetics of Eq. (3.2). Due to the limited amount of measured growth rates in the intermediate supersaturation region, it was, however, not possible to determine the parameters c, A and S_0 individually. Instead, these parameters were set manually to $c_{1,1} = 0.064$, $c_{2,1} = 250$ and $c_{3,1} = 1.044$ for the prismatic {100}-faces and to $c_{1,2} = 0.048$, $c_{2,2} = 500$ and $c_{3,2} = 1.035$ for the pyramidal {101}-faces. The resulting growth rates (solid lines) are shown in Figure 3.10 as a function of supersaturation together with the measured growth rates (markers) and the BCF kinetics (dashed lines) of Eq. (3.2). As can be seen, the measured growth rates can
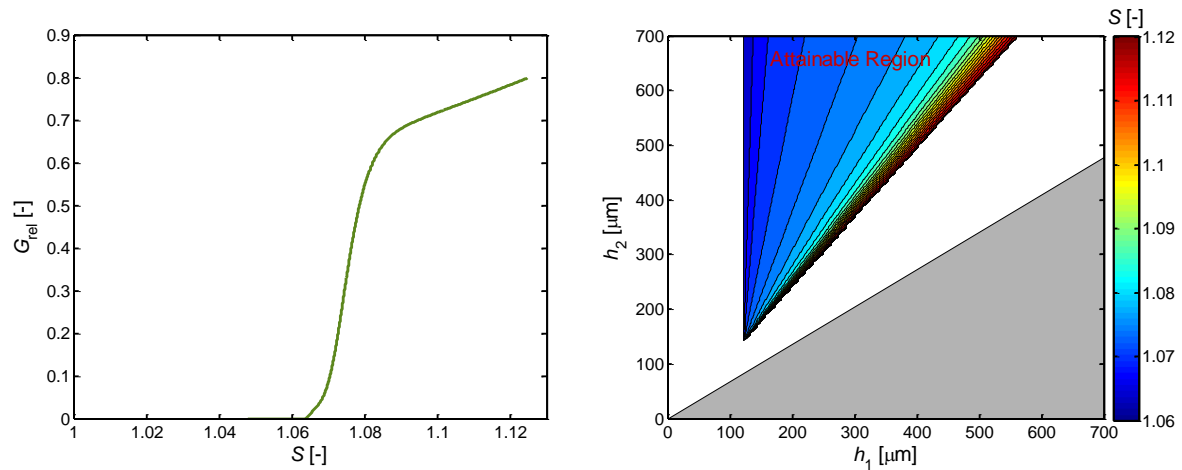
Figure 3.11: Final crystal shapes attainable via growth at $T = 35$ °C; left: relative growth rate G_{rel} as a function of supersaturation; right: supersaturation required to obtain a specific final crystal shape.

qualitatively be well reproduced by employing the model for the step-pinning mechanism. The observed dead zone of the growth rates could be reproduced as well as the growth behavior at higher supersaturation levels which was essentially unaffected by the presence of impurities. Particularly the latter observation provides a qualitative explanation for the observation that the growth rate of the prismatic {100}-faces of KDP is not dependent on the raw material used at higher supersaturations while this was clearly the case at lower supersaturations (see Figure 3.8).

Using the growth kinetics depicted in Figure 3.10, the crystal shapes attainable from an initial shape $\mathbf{h}_0$ can be determined together with the supersaturation which is required for the individual shapes. As already pointed out in Section 3.1, the relative growth rate G_{rel} can be used to quantify the crystal shape towards which the growing crystals evolve. Low values of G_{rel} indicate that growth of the {101}-faces is significantly higher than the growth of the {100}-faces. Hence, crystals grow towards elongated crystal shapes. Values of $G_{rel} \approx 1$ imply that both face types grow with similar velocities which ultimately result in the growth of compact crystals. The dependence of the relative growth rate on supersaturation resulting from the kinetics shown in Figure 3.10 is depicted in the left panel of Figure 3.11. It can be seen that the relative growth rate is zero for supersaturation below 1.06. A sharp increase in the relative growth rate is observable in a supersaturation range between 1.06 and 1.08, which is caused by the sharp increase in the growth rate of the {100}-faces (see Figure 3.10, left). At higher supersaturations, the relative growth rate increases only mildly, and reaches a maximum value of 0.8 at a supersaturation of $S = 1.12$. The region of crystal shapes attainable by these relative growth rates is shown in the right panel of Figure 3.11 together with the supersaturation necessary to obtain the individual shapes. Although the attainable region is quite large, it can be seen that the majority of the attainable crystal shapes require a supersaturation in the range of $1.06 < S < 1.08$, and therefore growth conditions at which the impurities have a strong influence on the growth kinetics and thus on the final crystal shape.
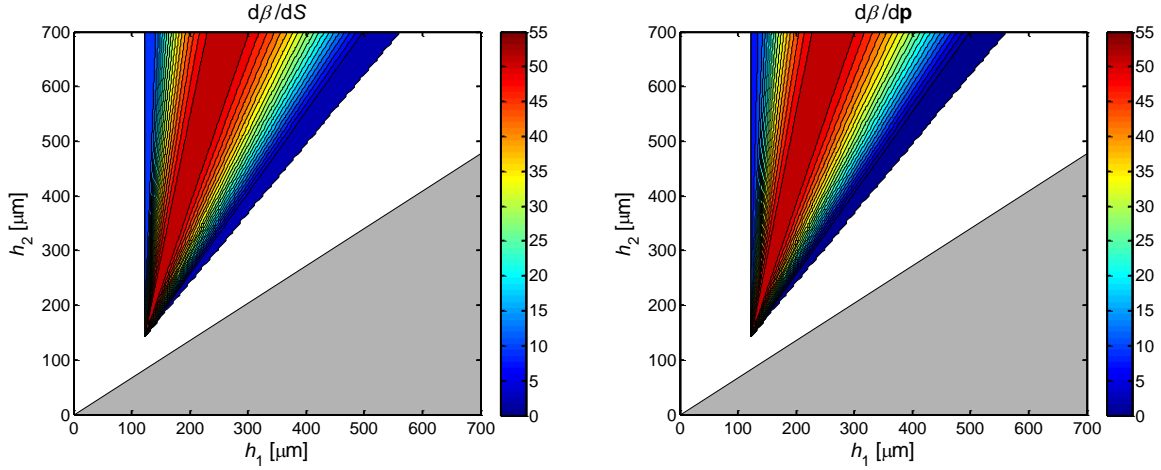
Figure 3.12: Sensitivities of the final crystal shape with respect to uncertainties during a single growth process; left: sensitivity of the final crystal shape with respect to supersaturation; right: sensitivity of the final crystal shape with respect to uncertainties of the parameters c_1, c_2 and c_3 of Eq. (3.13) and Eq. (3.14).

To quantify the influences of the supersaturation and the impurity concentration on the final crystal shape, the angle β is introduced. It is defined as the angle between the crystal shape trajectory and the abscissa:

$$\beta = \text{atan}\left(\frac{G_1}{G_2}\right) = \text{atan}\left(\frac{1}{G_{\text{rel}}}\right) = \text{atan}\left(\frac{h_{\text{F},2} - h_{0,2}}{h_{\text{F},1} - h_{0,1}}\right). \tag{3.15}$$

Note, that β does not describe the final crystal shape directly, but rather parameterizes the steady state crystal shape towards which the crystals are evolving during growth under constant conditions. Obviously, β is an implicit function of supersaturation (and temperature, which is, however, neglected in the following discussion), and the function $\beta(S)$ results directly from the growth kinetics $G_1(S)$ and $G_2(S)$, or the relative growth rate $G_{\text{rel}}(S)$. Due to the strong increase in G_{rel} at supersaturation levels between 1.06 and 1.08, the resulting crystal shapes show a high sensitivity w.r.t. the choice of supersaturation. Therefore, a precise control of the driving force is required if such a crystal shape is to be realized with a single growth step. The sensitivity of the final crystal shape to variations of supersaturation is quantified by the derivative $d\beta/dS$, which was calculated using Eq. (3.12) and is depicted in the left panel of Figure 3.12 for all crystal shapes attainable by growth.

Qualitatively, three different regions can be identified in this contour plot. At low supersaturation, growth of the {100}-faces is essentially inhibited, and hence crystals evolve towards elongated shapes regardless of smaller variations in supersaturation. Conversely, at high supersaturations, both face types grow with similar rates which again results in a low sensitivity $d\beta/dS$. At intermediate supersaturations however, the sensitivity exhibits a distinct maximum and hence, tight supersaturation control as well as precise knowledge of the growth kinetics $G_1(S)$ and $G_2(S)$ are required to obtain such crystal shapes with a single growth step. Especially the latter criterion must be considered crucial, since particularly in this supersaturation region the growth kinetics of the {100}-faces are strongly influenced by the impurities present in the solution. This in turn yields a high sensitivity of the resulting crystal shapes w.r.t. the impurity concentration.

In this work, the dependencies of the growth kinetics on these impurity concentrations were parameterized by the parameters c_i in Eq. (3.13) and Eq. (3.14) for a specific face. It is therefore straightforward to assemble these parameters in a vector $\mathbf{p} = [c_{1,1}, c_{1,2}, c_{3,1}, c_{1,2}, c_{2,2}, c_{3,2}]^T$ and to define the sensitivity $d\beta/d\mathbf{p}$ by:

$$\frac{d\beta}{d\mathbf{p}} = \sum_{i=1}^{6} \left| \left(\frac{\partial \beta}{\partial p_i} \right)_{p_{j \neq i}} \right| . \tag{3.16}$$

The resulting sensitivities $d\beta/d\mathbf{p}$ were again calculated using Eq. (3.12) and are shown in the right panel of Figure 3.12 for all crystal shapes attainable by growth. The sensitivities are qualitatively very similar to the sensitivities $d\beta/dS$ discussed above. While elongated and compact crystals can be reliably obtained, even under varying impurity concentrations, the attainability of intermediate crystal shapes is strongly sensitive to the impurity concentrations in the solution. It can hence be concluded that the control of such crystal shapes requires not only tight supersaturation control and accurate knowledge of the crystallization kinetics, but also tight control of the impurity concentrations in the solution. The latter is, however, challenging to realize in industrial practice. At this point it has to be stressed once more, that the growth kinetics used for the sensitivity analysis were subject to large uncertainties in the supersaturation range of $1.06 \leq S_G \leq 1.08$ due to the limited amount of measured growth rates. Therefore, this discussion is rather of a qualitative nature than of a quantitative one. The general behavior of the sensitivities $d\beta/dS$ and $d\beta/d\mathbf{p}$ will, however, be as discussed, regardless of the specific 'true' growth kinetics of the {100}-faces at this intermediate supersaturation range.

A further interesting phenomenon related to growth affected by impurities has been reported by Guzman et al. (2001). The authors found that the growth rate of potassium sulfate crystals was larger when supersaturation was decreased compared to the growth rates that were obtained by increasing the supersaturation. The presence of impurity molecules was shown to be the reason for this phenomenon which is called growth hysteresis. In subsequent research, also the growth of the prismatic {100}-faces of KDP was shown to be affected by growth hysteresis in the presence of impurities (Guzman 2005). Although this effect was demonstrated experimentally only for Cr^{3+} impurities in case of KDP, the mathematical framework used to model this behavior suggests, that growth hysteresis is a generally observable phenomenon if growth is affected by the presence of impurities (Kubota 2003, Guzman 2005). This finding is particularly important for the concept of growth-dissolution cycles, as will be discussed in Chapter 4, where both a decrease and an increase in supersaturation are inevitable due to the necessary supersaturation switches. The occurrence of growth rate hysteresis in such a process may lead to a significant decrease of the growth rates after the first growth phase and, in the worst case, to no significant growth during the second growth phase. Since Guzman et al. (2001, 2005) were able to show that the effect of growth hysteresis is diminishing at high supersaturations, it can be concluded that growth in a cyclic growth-dissolution process for KDP should preferably be conducted at high supersaturations at which growth is not affected by the presence of impurities.
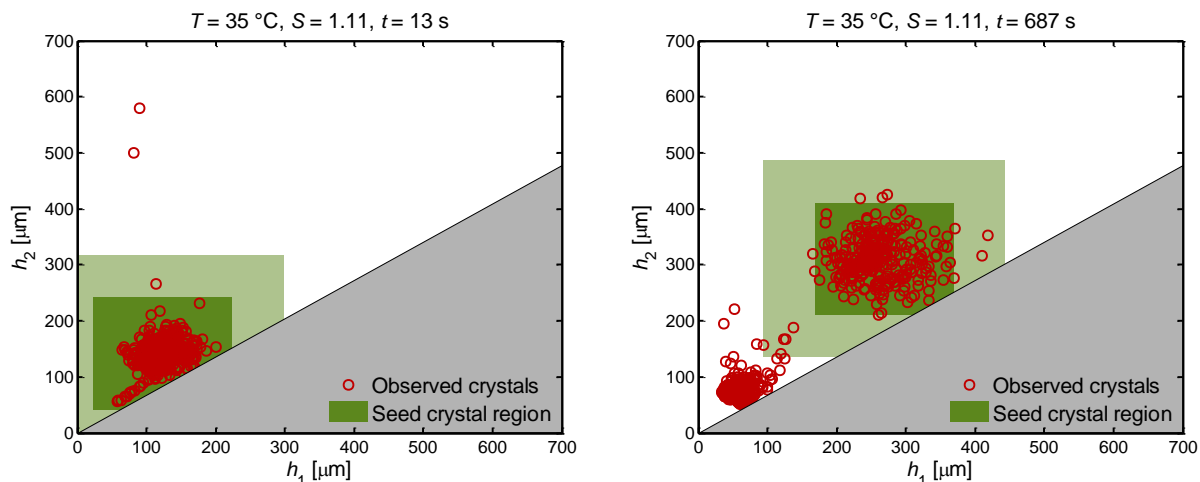
Figure 3.13: Observed crystal shape distributions during one growth experiment at the initial - (left) and the final experimental time (right).

3.3 Growth Rate Dispersion

The evolution of the mean seed crystal shape was used in the previous sections to determine the face-specific growth kinetics of KDP. Next to this information, the experiments also hold information about the evolution of the entire CSSD. The experimental data revealed not only crystal growth, but also a significant widening of the CSSD was apparent. This is illustrated in Figure 3.13, where the final CSSD of one growth experiment is compared to the initial CSSD. Such a widening of the CSSD cannot be explained by the PBE approach of Eq. (2.16), which predicts that the width of the seed distribution remains constant over time. Instead, two different modeling approaches are typically used to describe the widening of the CSSD during growth, namely i) size dependent growth and ii) growth rate dispersion. Since size dependent growth – a model frequently used to describe such a CSSD-widening (Majumder 2010, Nagy 2011, Bajcinca 2012, Ochsenbein 2014) – was not observed in any experiment, the CSSD-widening can clearly be attributed to the phenomenon of growth rate dispersion (GRD). According to the BCF theory (Burton 1951), the growth rate of a crystal face is related to the activities of the screw dislocations on this face. These activities are dependent on the structure of the dislocation network on the crystal surface, which can be assumed to be randomly distributed. Hence, the growth rate of two crystal faces that are crystallographically equivalent might differ even at identical growth conditions (i.e. supersaturation and temperature). Furthermore, due to crystal-crystal – and crystal-wall collisions, new dislocations might be formed, or active dislocations might be deactivated. Hence, crystal growth rates might also fluctuate over time. Apart from the dislocation network on the crystal surface, also other effects like lattice strain (Zacher 1995, Ristic 1997, Jones 1999), surface roughening (Pantaraks 2007, Flood 2010) or the absorption of impurity molecules (which is stochastic by nature) are known to influence the growth rates of crystal faces

For the quantitative description of growth rate dispersion, two main approaches can be identified. The first approach assumes that crystal growth rates fluctuate randomly around a

constant time averaged value in case growth conditions are constant. This random fluctuation (RF) model results in one additional second order dispersive term per internal coordinate in the population balance equation, to give:

$$\frac{\partial f}{\partial t} + \sum_{i=1}^{n} G_i \frac{\partial f}{\partial h_i} - \sum_{i=1}^{n} d_i \frac{\partial^2 f}{\partial h_i^2} = 0.$$

(3.17)

In this equation, d_i denotes the so-called growth rate diffusivity of the i-th face, which is assumed to be size independent in this work. As discussed by Zumstein and Rousseau (1987a, 1987b), the solution of Eq. (3.17) implies that, at constant growth conditions, the variances σ_i^2 of the marginal distributions $f_{h,i}$

$$f_{h,i} = \int_{\Omega_{h,j}} f dh_j, \quad j \neq i,$$

(3.18)

are linearly increasing with time according to:

$$\frac{d\sigma_i^2}{dt} = 2d_i.$$

(3.19)

This linear increase has been employed by several authors (White 1971, Randolph 1977) to identify the random fluctuation model as a suitable approach to describe the phenomenon of growth rate dispersion.

An alternative to the RF model for growth rate dispersion is the constant crystal growth (CCG) model. This model assumes that every crystal face has an individual growth rate, which can, in the simplest case, be calculated by:

$$G_{i,j} = p_{i,j} G_i.$$

(3.20)

Here, G_i is the mean growth rate of the crystal population, as for example determined by the methods presented in Section 3.1, and $p_{i,j}$ is a pre-factor that specifies the growth rate of the i-th face type of the individual crystal j. Hence, the crystal population is not only distributed in the n-dimensional $\mathbf{h}$-space, but also in n additional coordinates $\mathbf{p}$, referred to as growth affecting properties (GAP) (Ochsenbein 2015), characterizing the growth rate distribution of the individual crystals. However, it is assumed, that no transport phenomena take place in the additional property coordinates, and hence, the PBE for this model reads:

$$\frac{\partial f(\mathbf{h},\mathbf{p},t)}{\partial t} + \sum_{i=1}^{n} G_i(\mathbf{p},t) \frac{\partial f(\mathbf{h},\mathbf{p},t)}{\partial h_i} = 0,$$

(3.21)

In contrast to the random fluctuation model, the CCG model predicts that the variances σ_i^2 are increasing quadratically with time (Zumstein 1987a, Zumstein 1987b) according to:

$$\frac{d\sigma_i^2}{dt} = c_1 t + c_2,$$

(3.22)
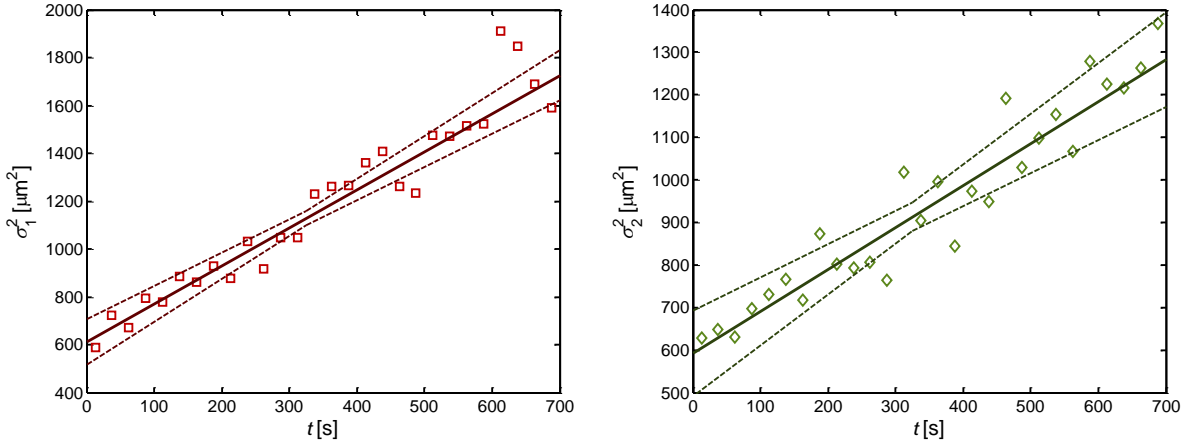
Figure 3.14: Evolution of the variances over time exemplified by one growth experiment; left prismatic {100}-faces; right: pyramidal {101}-faces. Confidence intervals were determined on a significance level of 95 %, and are indicated by dashed lines.

with constants c_1 and c_2. With the help of this criterion, the CCG model can be differentiated from the RF model, which was for instance done by Berglund and Larson (1984), Larson et al. (1985) or Ramanarayanan et al. (1985).

With increasing computational power, the assumption of no convective transport in the GAP coordinates was dropped in an extension of the CCG model by Gerstlauer et al. (2001), to model crystal growth under the consideration of a decrease in lattice strain, as well as by Ochsenbein et al. (2015) to model the growth behavior of β L-glutamic acid. Under these assumptions, the PBE reads (Ramkrishna 2000):

$$\frac{\partial f(\mathbf{h}, \mathbf{p}, t)}{\partial t} + \sum_{i=1}^{n} G_i(\mathbf{p}, t) \frac{\partial f(\mathrm{h}, \mathbf{p}, t)}{\partial h_i} + \sum_{i=1}^{n} \frac{\partial}{\partial p_i} \left(\frac{\partial p_i}{\partial t} f(\mathbf{h}, \mathbf{p}, t) \right) = 0 . \tag{3.23}$$

However, since the distribution of the crystal population in the GAP coordinates is generally hard to determine, and little information about the velocities $\partial p_i / \partial t$ is available, this approach was not further pursued in this work. Instead, only the adequacy of the RF and CCG model was investigated.

As can be seen from Eqs. (3.19) and (3.22), the RF and CCG models can be distinguished by plotting the measured variances σ_i^2 over time. While the RF model results in a linear increase of σ_i^2 over time, the CCG model predicts a quadratic dependence. The results of such an analysis are shown exemplarily in Figure 3.14. Clearly, the variances σ_i^2 are increasing linearly with time, which was the case for all growth experiments and both face types, provided that a significant growth rate was observable. Hence, the experimental results clearly support the validity of the RF model under the experimental conditions investigated in this work.

Similarly to the procedure for determining the face-specific growth kinetics in Section 3.1, the face specific growth rate diffusivities d_i were obtained by linear regression for all temperatures and supersaturations. The resulting values of d_i are shown in Figure 3.15 versus
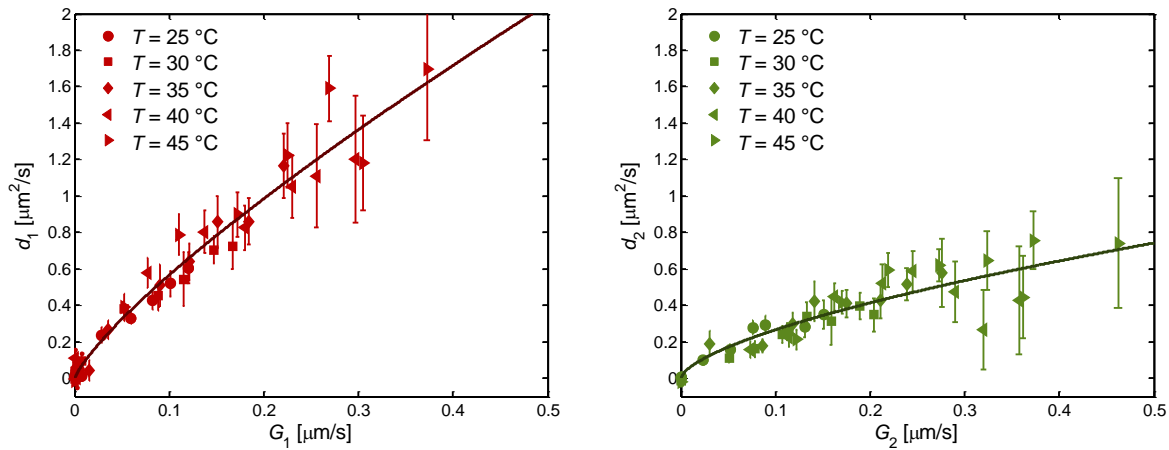
Figure 3.15: Dependencies of the growth rate diffusivities d_i on the face-specific crystal growth rates; left: prismatic {100}-faces; right: pyramidal {101}-faces. Different temperatures are indicated by the marker in the upper right corners. Thick solid lines represent the regressed power law approaches of Eq. (3.24).

Table 3.3: Parameter values of Eq. (3.24) for G_{ref} = 5 x 10^{-7} m/s. Confidence intervals are given for a significance level of 95%.

	{100}-faces		{101}-faces	
Symbol	Value	Confidence interval	Value	Confidence interval
$d_{0,i}$ [m²/s]	2.052 x 10^{-12}	± 0.176 x 10^{-12}	7.419 x 10^{-13}	± 1.376 x 10^{-13}
$n_{d,i}$ [-]	0.802	± 0.086	0.638	± 0.138

the determined growth rates. As can be seen, the growth rate diffusivities exhibit a positive correlation with the determined growth rates, whereas no significant dependence of d_i on temperature, indicated by different markers, can be identified. The dependencies of the growth rate diffusivities on the face-specific growth rates that are apparent from Figure 3.15 were parameterized in this work by an empirical power law approach:

$$d_i = d_{0,i} \left(\frac{G_i}{G_{ref}} \right)^{n_{d,i}} . \tag{3.24}$$

The parameters of these approaches were determined with a nonlinear least squares fitting procedure and are given in Table 3.3. The resulting correlations are shown in Figure 3.15 as thick solid lines. With this set of parameters and the RF approach of Eq. (3.17), the CSSD evolution can be simulated by accounting for the observed distribution widening. Assuming that the initial distribution is described by a bivariate normal distribution as well as constant growth conditions, an analytical solution to Eq. (3.17) can be found (Crank 1975). The population density remains normally distributed, with mean values and variances according to:

$$\bar{h}_i = \bar{h}_{0,i} + G_i t \tag{3.25a}$$

$$\sigma_i^2 = \sigma_{0,i}^2 + 2 d_i t . \tag{3.25b}$$
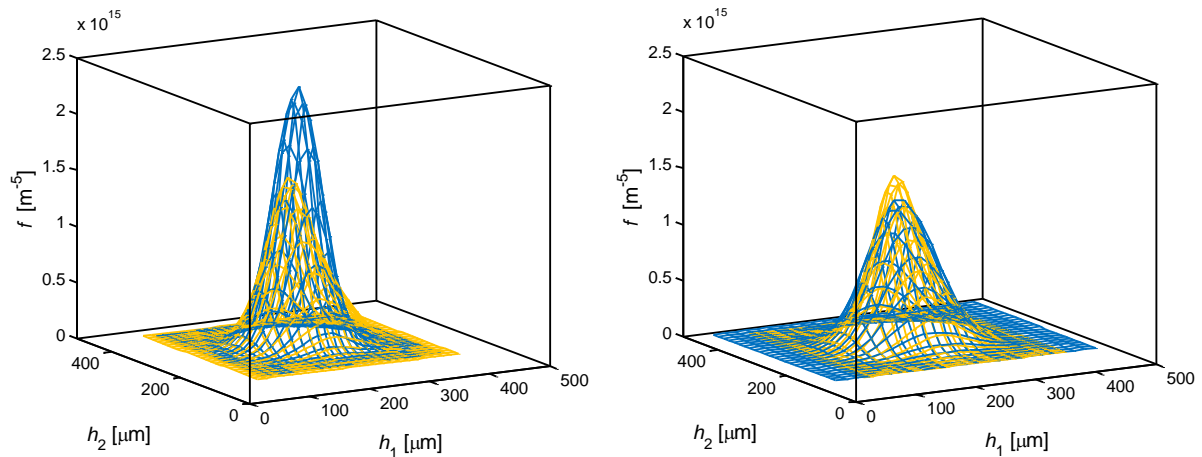
Figure 3.16: Comparison between observed (yellow) and simulated (blue) final CSSDs of one growth experiment; left: simulation results obtained without growth rate dispersion; right: simulation results using Eq.s (3.17), (3.24) and (3.25).

The simulation results obtained are exemplarily depicted in Figure 3.16 (right) together with the measured CSSD at the final experimental time and simulation results which would be expected in the absence of growth rate dispersion (Figure 3.16 left). As can be seen, the widening of the CSSD is quite substantial for the experiment considered, but can be captured well with the approaches and parameters of the RF model identified in this work.

At this point it is important to note, that the kinetics of growth rate dispersion were determined only on the basis of the seed crystal evolution and are strictly only valid for the seed crystal population. The application of these kinetics to the growth of nucleated crystals does therefore constitute an extrapolation of these kinetics which should be considered with some skepticism. Several authors report that the growth rate of small (secondary) nuclei differs significantly from the growth rate of larger crystals (like crystals of the seed crystal population) (Zacher 1995, Gahn 1997, Jones 1999, Temmel 2016b) which was attributed to higher lattice strain that arises from the process of secondary nucleation. Also the results of this work indicate that the growth of nucleated crystals is significantly slower than the growth of seed crystals. However, as evolution of the population of nucleated crystals is of minor importance within the concept of growth-dissolution cycles, this phenomenon was not further investigated in this work.

3.4 Nucleation Kinetics

During the experiments performed for the determination of the growth kinetics, not only an increase in crystal size and distribution width was detected (described in Sections 3.1 and 3.3, respectively), but also significant nucleation was observable. Nucleation leads to an increase in the total number of crystals, or the 0th moment of the CSSD respectively, according to:
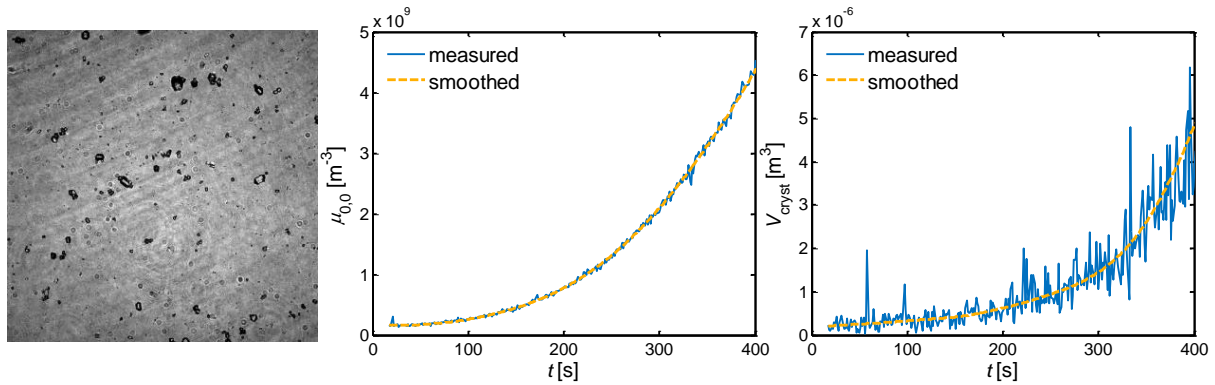
Figure 3.17: Observed increase in the total number of crystals over time; left: example frame showing a large number of nucleated crystals; middle: measured increase in the total number of observed crystals; right: measured increase in the total crystalline mass. Measurements are shown as solid blue lines whereas smoothed measurements are shown as dashed yellow lines.

$$\frac{d\mu_{0,0}}{dt} = B_{\text{nuc}}, \tag{3.26}$$

with B_{nuc} denoting the nucleation rate. By measuring the total amount of objects observed with the video microscope during a fixed time period, an estimate for the 0th moment could be obtained in this work[8]. Hence, the evolution of the 0th moment could be tracked over time. Such an evolution (observed during the growth experiment at $S = 1.12$ and $T = 45$ °C) is exemplarily shown in Figure 3.17 together with a representative video frame collected during the final state of the experiment. Not only is a significant increase in the observed crystal number visible in this figure, but also the convex curvature of the evolution $\mu_{0,0}(t)$ is apparent. This convex curvature is a clear indication for the presence of secondary nucleation. In contrast to primary nucleation, which would result in a linear evolution of $\mu_{0,0}(t)$ at constant crystallization conditions, the rate of secondary nucleation is dependent on the suspension density of the solution. This suspension density increases in a convex manner, due to growth and nucleation resulting in the creation of additional surface areas (as shown in the right panel of Figure 3.17), and hence, the secondary nucleation rate increases monotonically over time.

To parameterize the kinetics of nucleation, an Arrhenius approach was chosen to describe the temperature dependence of the nucleation kinetics, and power law approaches were employed for the quantification of the influences of supersaturation and suspension densities on the nucleation rates. In this work, the suspension densities were expressed through the total crystal surface area per volume μ_A, as well as through the total crystalline mass μ_V per volume. For the seed crystal population, these moments were calculated according to:

---

[8] By measuring the number of observed objects, overlapping crystals or crystal aggregates are considered as single objects, although in both cases the measured objects consists of several primary crystals. Therefore, the number of newly born crystals is underestimated by this approach, and the resulting nucleation kinetics constitute lower bound estimates of the 'true' nucleation kinetics.

$$\mu_{\mathrm{A}} = 21.896\mu_{1,1} - 4.001\mu_{2,0} \tag{3.27a}$$

$$\mu_{\mathrm{V}} = 10.948\mu_{2,1} - 4.983\mu_{3,0}. \tag{3.27b}$$

For nucleated crystals, Eq. (3.27) was not applicable, since the shape estimation on the basis of the rather small crystal projections that were observable for nuclei was deemed unreliable. Instead, the surface area and volume of those crystals was approximated by the surface area and volume of a sphere with a projection area equivalent diameter[9]. With the help of the moments μ_{A} and μ_{V}, the nucleation rate B_{nuc} was expressed through:

$$B_{\mathrm{nuc}} = k_{0,\mathrm{nuc}} \exp\left(-\frac{E_{\mathrm{A,nuc}}}{R}\left(\frac{1}{T} - \frac{1}{T_{\mathrm{ref}}}\right)\right)(S-1)^{n_{\mathrm{S}}} \mu_{\mathrm{A}}^{n_{\mathrm{M}}} \tag{3.28a}$$

$$B_{\mathrm{nuc}} = k_{0,\mathrm{nuc}} \exp\left(-\frac{E_{\mathrm{A,nuc}}}{R}\left(\frac{1}{T} - \frac{1}{T_{\mathrm{ref}}}\right)\right)(S-1)^{n_{\mathrm{S}}} \mu_{\mathrm{V}}^{n_{\mathrm{M}}}. \tag{3.28b}$$

The parameters $k_{0,\mathrm{nuc}}$, $E_{\mathrm{A,N}}$, n_{S} and n_{M} of these approaches were collected in the vector $\mathbf{p}$, and determined by a nonlinear least squares approach

$$\min_{\mathbf{p}} \sum_{i=1}^{n_{\mathrm{meas}}} \sum_{j=1}^{n_{\mathrm{t},i}} \left(\mu_{0,0,i,j,\mathrm{meas}} - \mu_{0,0,i,j,\mathrm{sim}}(\mathbf{p})\right)^2 . \tag{3.29}$$

In this equation, the 0th moment of the i-th experiment which was simulated for the j-th time instant is denoted by $\mu_{0,0,i,j,}$. The simulated values $\mu_{0,0,i,j,\mathrm{sim}}$ of the this equation were obtained by integrating the nucleation rate over time according to:

$$\mu_{0,0,i,j,\mathrm{sim}} = \mu_{0,0,i,j,\mathrm{meas}}(t_{i,0}) + \int_{t_{i,0}}^{t_j} B_{\mathrm{nuc}}\left(S_i(\tau), T_i(\tau), \mu_{\mathrm{A/V},i}(\tau)\right)d\tau . \tag{3.30}$$

The parameter estimation was performed for both approaches given in Eq. (3.28). Additionally, the moments μ_{A} and μ_{V} were calculated either with or without the observed nucleated crystals, and hence, four different sets of parameter estimates were obtained.

As can be seen from Figures 3.17 and 3.18, the measurements of the 0th moments as well as the measurements of μ_{A} and μ_{V} exhibit a significant measurements noise. In order to reduce this noise, and thereby to achieve a better convergence behavior of the optimization routines used to solve Eq. (3.29), both, the 0th moment as well as μ_{A} and μ_{V} were smoothed prior to the optimization (see Figures 3.17 and 3.18).

The parameter estimates that resulted from solving Eq. (3.29) and the optimal objective function values are given in Table 3.4 for all four approaches. It can be seen from this table

---

[9] The treatment of the nucleated crystal as spherical particles constitutes a rather course approximation of the 'true' shape of these crystals. This approximation was, however, necessary as a reliable shape-estimation was not possible with the procedures given in Section 2.4 due to the finite resolution of the microscope camera. As (significant) nucleation occurred at supersaturations above $S = 1.08$ (compare Figure 3.18), the nuclei, that were formed, assumed a rather compact shape, and hence, the approximation error that is induces by the assumption of spherical shapes can be expected to be rather small.
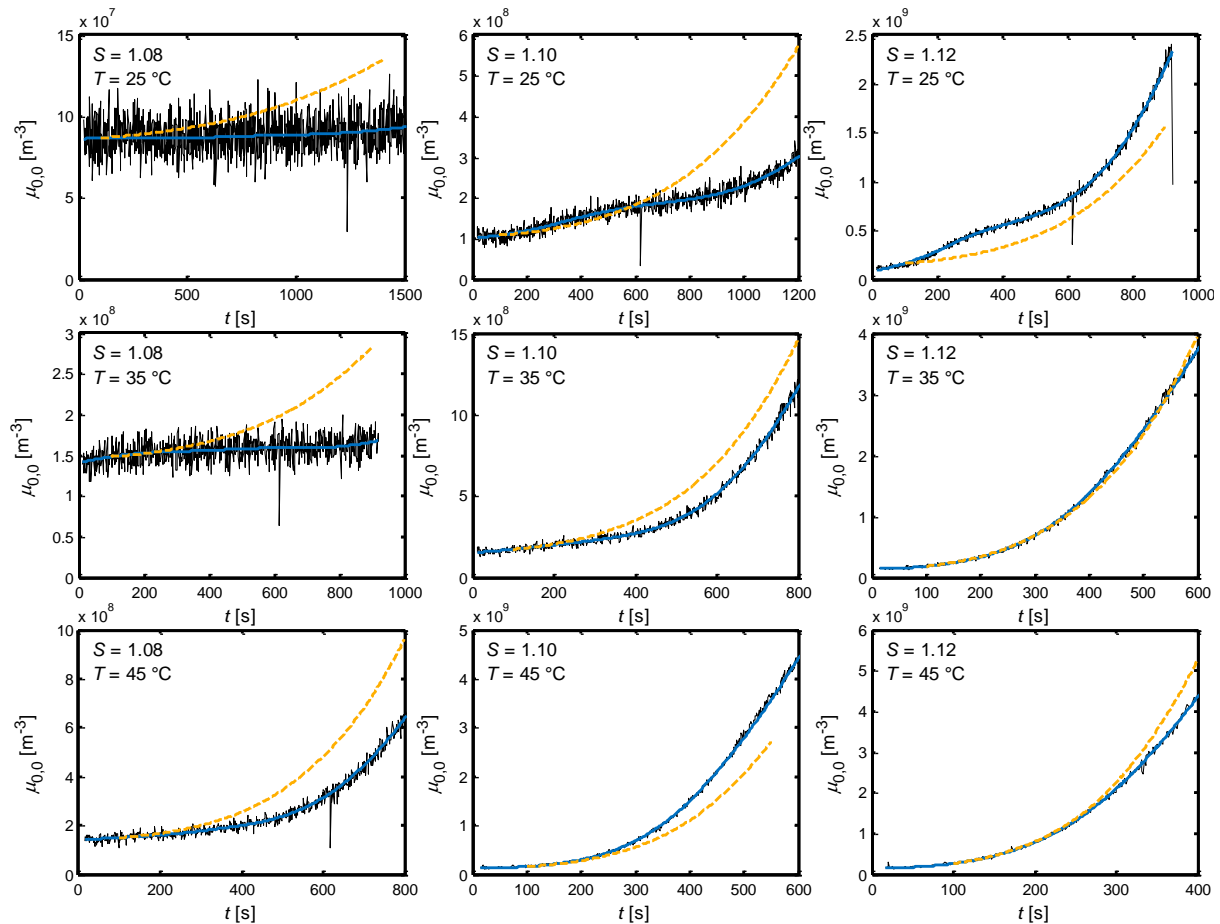
Figure 3.18: Comparison between measured and simulated evolution of the 0th moment over time; thin black lines: measurements; thick blue lines: smoothed measurements; dashed yellow lines: simulation results obtained using Eq. (3.28a) and considering only the second order moments of the seed crystal population.

that the approaches only considering the surface area or the crystal volume of the seed crystal population lead to better model fits (in terms of the residual) compared to the results that were obtained by considering also the second or third order moments of the nuclei. This might be explained by differences in the slip velocities of the crystals compared to the local solution velocities. Due to the small size and comparably large surface-to-volume ratio of the nucleated crystals, it can be assumed that nucleated crystals were able to follow the stream lines of the solution better that the larger crystals of the seed population. Hence, collisions between nucleated crystals might be quite rare compared to collisions between two seed crystals. Furthermore, the impact of collisions between nucleated crystals and other crystals or crystallizer walls might be significantly lower than for seed crystals, which in turn can be expected to result in lower secondary nucleation rates.

Comparing the results of the approaches given by Eq. (3.28a) and (3.28b) for the seed crystal population only, no significant difference was found. This might be attributed to a rather strong correlation between μ_A and μ_V. A designed variation of the seed crystal loading (in terms of initial mass and size distribution) might be suitable to differentiate between the different nucleation approaches given in Eq. (3.28a) and (3.28b). This was, however, not done in this work, as the experiments were primarily designed for the determination of the

Table 3.4: Parameter values of Eq. (3.28a) and Eq. (3.28b) considering the surface area/volume of either all crystals or of the seed crystal population only. The reference temperature T_{ref} was set to 35 °C, and confidence intervals are given for a significance level of 95%.

|		All crystals		Seed crystals	
	Symbol	Value	Confidence interval	Value	Confidence interval
Surface area	$\ln(k_{0,nuc})$ [-]	22.688	± 0.032	24.194	± 0.058
	$k_{0,nuc}$ [1/(m^{3-n_M} s)]	7.14×10^9	$[6.91 \ 7.37] \times 10^9$	3.22×10^{10}	$[3.04 \ 3.41] \times 10^{10}$
	$E_{A,nuc}$ [kJ/mol]	52.730	± 0.200	62.069	± 0.262
	n_S [-]	5.536	± 0.0128	7.172	± 0.024
	n_M [-]	1.556	± 0.005	2.586	± 0.014
	residual	4.44×10^{20}	-	3.36×10^{20}	-
Volume	$\ln(k_{0,nuc})$ [-]	39.140	± 0.075	42.145	± 0.087
	$k_{0,nuc}$ [1/(m^3s)]	9.96×10^{16}	$[9.24 \ 10.74] \times 10^{16}$	2.01×10^{18}	$[1.84 \ 2.19] \times 10^{18}$
	$E_{A,nuc}$ [kJ/mol]	50.224	± 0.314	60.425	± 0.259
	n_S [-]	6.395	± 0.027	7.023	± 0.024
	n_M [-]	1.513	± 0.009	1.683	± 0.009
	residual	4.36×10^{20}	-	3.42×10^{20}	-

growth kinetics (see Section 3.1). Since the approach of Eq. (3.28a) was found to be slightly better compared to Eq. (3.28b), only the simulation results of this approach are shown in Figure 3.18 in comparison to the measurements. Despite some notable deviations between simulations and measurements, the overall trends could be reproduced well. The observable deviations can be attributed to the stochastic nature of the nucleation process, as well as to the empirical nature of the chosen regression approach.

3.5 Dissolution Kinetics

Dissolution is often seen as the reverse process of growth. While this is obviously true in the light of the question whether solute molecules are incorporated in – or removed from the crystal lattice, some fundamental differences in the mechanisms of kink site formation (as already discussed in Section 2.6) can be expected. Thus, the kinetics of growth and dissolution have to be expected to be different, and a detailed analysis of the dissolution kinetics is certainly required in the context of growth-dissolution cycles.

Apart from this process concept, dissolution rates are a key aspect particularly in the field of pharmaceuticals. It is well known that (opposed to growing crystals) dissolving crystals evolve away from a steady state morphology[10] (Snyder 2007a). Therefore, the accuracy of any one-dimensional model to describe the dynamics of dissolution and the accompanied

---

[10] Apart from rather idealized special cases (Singh 2014).
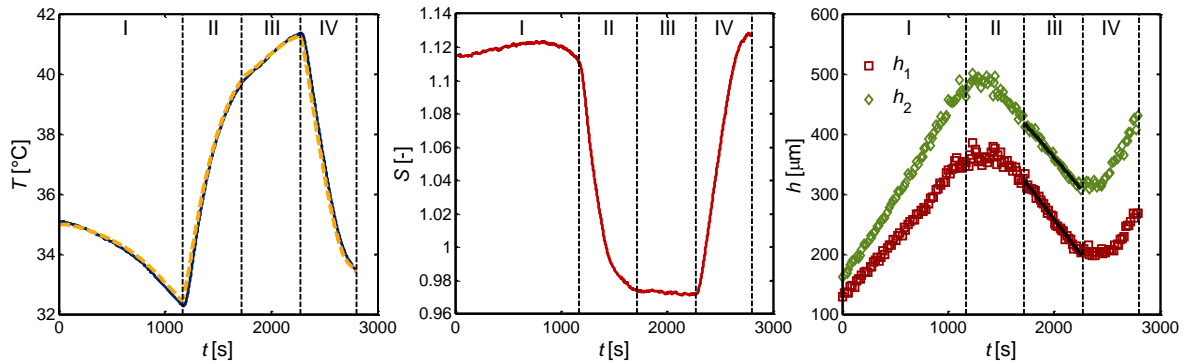
Figure 3.19: Estimation of the face-specific dissolution rates of KDP at constant levels of undersaturation and approximately constant temperature; left: set-point temperature profile (dashed yellow) and measured temperature profile (solid blue); middle: measured super- and undersaturations; right: measured (marker) and regressed (solid lines) evolutions of the mean seed crystal shapes. Prismatic {100}-faces are indicated by red squares while pyramidal {101}-faces are indicated by green diamonds.

increase in solute concentration can only be of limited precision. Any more detailed and accurate model does (in conjunction with the initial CSSD) necessarily require the consideration of face-specific dissolution kinetics. Hence, this chapter aims developing a methodology for determining such face-specific dissolution rates as well as at analyzing the obtained kinetics with special emphasis on the concept of growth-dissolution cycles.

The experimental procedure employed for the determination of the face-specific dissolution rates of KDP is exemplarily depicted in Figure 3.19. As indicated, this procedure can be divided into four different phases. Initially, seed crystals were grown in a supersaturated solution to a size large enough to allow for sufficiently long dissolution times in the subsequent phases. After this phase, the three-way valves (see Figure 2.1) were switched to connect the second thermostat to the crystallizer jacked in order to create an undersaturated solution[11]. Once the desired level of undersaturation was reached, the crystallizer temperature profile was controlled[12] to maintain the level of undersaturation constant. The seed crystals were allowed to dissolve until they reached a minimal size to ensure that no seed crystals disappear during the dissolution process. In the final phase, the three-way valves were switched back, connecting the crystallizer jacked to the initial thermostat in order to generate a supersaturated solution. This way, a final growth phase was induced. As can be seen in Figure 3.19, the level of undersaturation could be controlled well during the dissolution phases, with the solution temperature increasing only slightly. Due to these constant dissolution conditions, the mean seed crystal shapes decreased linearly with time, indicating

---

[11] The necessary temperature profiles of the thermostats were calculated by Eq. (4.21) of Section 4.3 of this work.

[12] The temperature control program for a constant level of undersaturation was based on Eqs. (4.8) and (4.15) of Section 4.2 of this work. Note that in order to apply Eq. (4.15), the growth kinetics need already to be known. Since these kinetics are to be determined through the experiments that are described in this section, they could naturally not be used for Eq. (4.15). Instead, kinetics which were obtained in preliminary experiments were used for the computation of the temperature profiles.
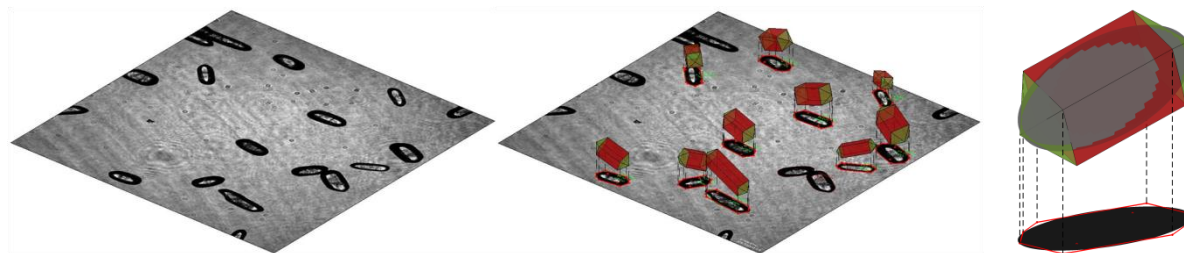
Figure 3.20: Shape estimation of dissolving KDP crystals; left: example frame of dissolving crystals; middle: crystal shapes estimated from the example frame; right: approximation of an ellipsoid (gray) by the typical shape of a grown KDP crystal (color) on the basis of the observed ellipsoid projection (black).

that the dissolution rates were neither size – nor shape dependent. Hence, the dissolution rates could be obtained by linear regression, as indicated by the solid lines in the right panel of Figure 3.19.

As soon as the solution was undersaturated, a fast disappearance of the crystal edges and vertices was apparent from the recorded suspension videos. Instead of the bi-pyramidal prismatic crystal shape, typical for grown KDP crystals, the crystals assumed an ellipsoidal shape, as depicted in Figure 3.20. This phenomenon can be explained by the appearance of higher indexed faces on the outer crystal surface which exhibited faster dissolution rates compared to the initial {100} and {101} faces, and were hence dominating the resulting crystal shape (Snyder 2007a).

Despite the presence of these higher indexed crystal faces, the same shape estimation routines already used to estimate the shapes of growing crystals were also applied to dissolving crystals. As stated in Section 2.4, the routines are based on the assumption that the outer crystal surfaces are solely composed of prismatic {100}-faces and pyramidal {101}-faces. As these assumptions are clearly not met by the dissolving crystals, the application of the shape estimation routines has to be evaluated critically in these cases.

The left and middle panels of Figure 3.20 depict typical shape estimates obtained during the dissolution experiments. As can be seen, the observed crystal projections could be approximated well by the crystal shape model, and the crystal shape estimates were preferentially oriented parallel to the image plane. While the first observation has to be expected as the mismatch between measured and simulated projection is minimized in the shape estimation routines, the latter observation coincides with the preferential orientation that was already observable for grown KDP crystal with a higher aspect ratio (see Figure 2.8 in Section 2.4 for comparison).

To further test the estimation routines the computed projection obtained from a perfect ellipsoid was used as an input for the shape estimation routines. The resulting crystal shape estimate is shown in the right panel of Figure 3.20 together with the original ellipsoid and its projection. Clearly both, the projection and the original ellipsoid orientation could be estimated well, thus supporting the applicability of the shape estimation routines also for dissolving KDP crystals.

A further supportive argument for the suitability of the shape estimation routines to approximate the shape of dissolving crystals is given by the measured mean shape evolution
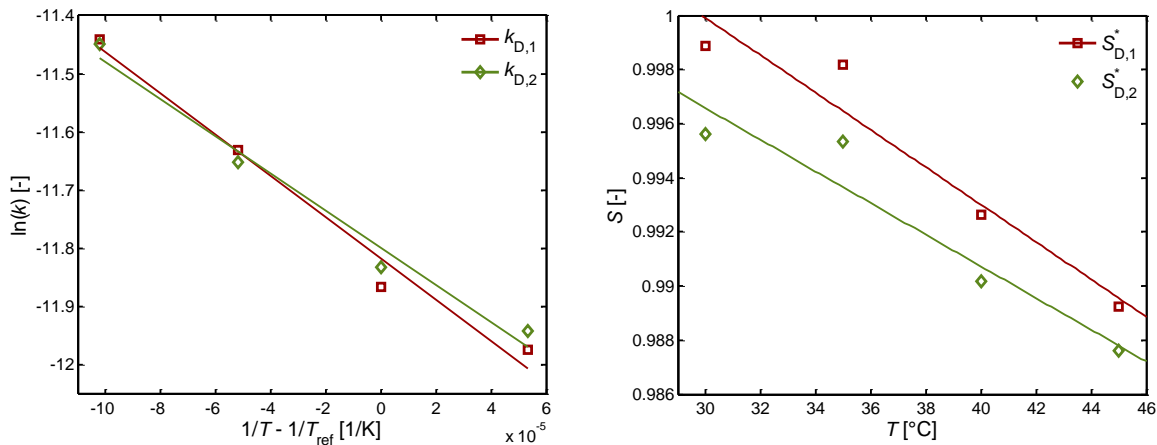
Figure 3.21: Temperature dependence of the face-specific dissolution rates of KDP; left: Arrhenius plot of the pre-exponential factors $k_{D,i}$ over the temperature; right; temperature dependence of the threshold undersaturations $S^*_{D,i}$ defined by Eq. (3.34). {100}-faces are indicated by red squares and {101}-faces are indicated by green diamonds.

(depicted in the right panel of Figure 3.19). The experimental procedure described above allowed for growth of the crystals during the final experimental phase, resulting in the reappearance of the typical {100}- and {101}-faces on the crystal surfaces. The application of an inappropriate shape model during the dissolution phase would result in shape estimates exhibiting a systematic error. This error would disappear quickly during the final growth phase, and hence, an almost instantaneous jump in the shape estimates would be expected during this experimental phase, in case the crystal shape model was not suitable. Such a jump in the shape estimate was however not observed and it can hence be concluded that the shape model of grown KDP crystals is also applicable for the shape estimation of dissolving KDP crystals[13].

The dissolution experiments described above and depicted in Figure 3.19 were repeated for different levels of undersaturation and different temperatures in the range of $0.93 \leq S \leq 0.99$ and $30\,°C \leq T \leq 45\,°C$. A linear dependence of the dissolution rates of both face types on the level of undersaturation was observed at all investigated temperatures, see Figure 3.22. Hence, this dependence was parameterized by the following approach:

$$D_i = k_{D,i}\left(S - S^*_{D,i}\right), \tag{3.32}$$

with temperature dependent parameters $k_{D,i}$ and $S^*_{D,i}$, that were determined by linear regression. The temperature dependence of the obtained dissolution rate constants $k_{D,i}$ is shown in Figure 3.21, left. In the Arrhenius plot, a linear decrease of the growth rate constants is observable, and hence, the temperature dependence of the dissolution rate

---

[13] Note that this conclusion can only be drawn for dissolving KDP crystals. The applicability of the shape estimation routines to other dissolving crystals need to be investigated separately. In fact, it can be expected that crystal shapes exist (for example crystals from a cubic space group with several different face-types) for which the application of the shape estimation routines will fail.
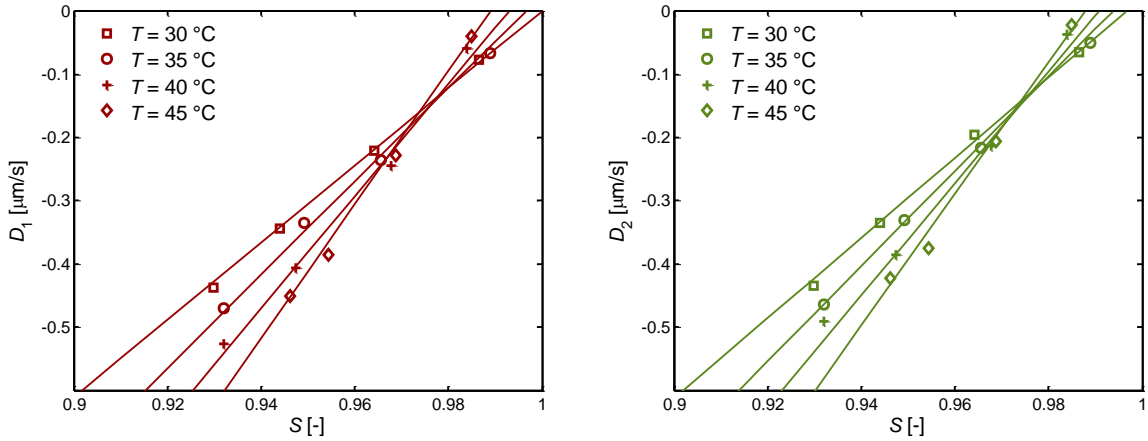
Figure 3.22: Obtained face-specific dissolution rates of KDP as a function of undersaturation and temperature; left: prismatic {100}-faces; right: pyramidal {101}-faces. Measured dissolution rates for different temperatures are indicated by the markers in the upper left corners.

Table 3.5: Parameter values of Eq. (3.33) and Eq. (3.34) for a reference temperature T_{ref} of 35 °C. Confidence intervals are given for a significance level of 95%.

	{100}-faces		{101}-faces	
Symbol	Value	Confidence interval	Value	Confidence interval
$\ln (k_{0,D,i})$ [-]	-11.816	$\pm$ 0.099	-11.798	$\pm$ 0.088
$k_{0,D,i}$ [m/s]	7.383 x 10^{-6}	[6.684, 8.155] x 10^{-6}	7.519 x 10^{-6}	[6.887, 8.209] x 10^{-6}
$E_{A,D,i}$ [kJ/mol]	29.376	$\pm$ 13.096	26.502	$\pm$ 11.566
$s_{1,D,i}$ [-]	0.9965	$\pm$ 0.0035	0.9937	$\pm$ 0.0034
$s_{2,D,i}$ [°C^{-1}]	-6.902 x 10^{-4}	$\pm$ 5.637 x 10^{-4}	-5.637 x 10^{-4}	$\pm$ 5.541 x 10^{-4}

constants was parameterized by:

$$k_{D,i} = k_{0,D,i} \exp\left(-\frac{E_{A,D,i}}{R}\left(\frac{1}{T} - \frac{1}{T_{ref}} \right) \right). \tag{3.33}$$

The pre-exponential factors and the activation energies of this law were again determined by linear regression and are given in Table 3.5 together with their confidence intervals. The threshold undersaturation values $S^*_{D,i}$, calculated from regressing Eq. (3.32) for different temperatures, are shown in the right panel of Figure 3.21. As can be seen, the values were in the range of 1 % undersaturation, and thus approximately correspond to the accuracy of the solubility data. Therefore, and due to the limited amount of data points at low undersaturations, it was not possible to fully clarify whether the true values for $S^*_{D,i}$ did deviate significantly from zero. However, the determined values were used for fitting the dissolution kinetics. Their temperature dependence was parameterized by:

$$S^*_{D,i} = s_{1,D,i} + s_{2,D,i}(T - T_{ref}) . \tag{3.34}$$

The empirical constants calculated for this approach are again given in Table 3.5 together with their confidence intervals.

The dissolution kinetics resulting from Eqs. (3.32) to (3.34) are shown in Figure 3.22, as a function of undersaturation and temperature. Generally, two trends can be identified from this figure. The dissolution rates are significantly faster that the growth rates at similar driving forces (see Figure (3.4) for comparison). This observation can be explained by the occurrence of higher indexed faces during the dissolution processes, resulting in ellipsoidal crystal shapes as described earlier. These ellipsoidal shapes suggest that the dissolution rates were in fact virtual dissolution rates dictated by the dissolution rates of the fastest dissolving crystal faces. Hence, the dissolution rates can be expected to be faster compared to the dissolution rates which would have been obtained from (infinitely) large single faces. This is particularly true, since the appearance of kinked faces have to be expected during the dissolution process, whose dissolution rates will be solely limited by bulk diffusion processes. A diffusion-limited dissolution process predicts that all face types dissolve with the same dissolution rates (Singh 2014), which is the second observation that is apparent from Figure 3.22. This in turn implies that variations in crystal shape during the dissolution process are solely a result of the choice of the initial crystal shape, and not the result of an appropriate choice of temperature or level of undersaturation.

The observation of identical dissolution rates of both face types for all temperatures and levels of undersaturation has strong implications on the applicability of the concept of growth-dissolution cycles for crystal shape control. Such a dissolution behavior requires the existence of growth conditions resulting in a relative growth rate $G_{\mathrm{rel}} \neq 1$ as the crystal shape trajectory evolves on a straight line only otherwise. This straight line can be parameterized by

$$\mathbf{h}(\tau) = h_0 + [1,1]^{\mathrm{T}}\tau ,\tag{3.35}$$

with:

$$-\min\left[h_{0,1}, h_{0,2}\right] \leq \tau \leq \infty .\tag{3.36}$$

Obviously, crystal shapes on this line could already be obtained by a single growth (or dissolution) phase, which would make the application of growth-dissolution cycles obsolete. If, however, growth conditions exist for which $G_{\mathrm{rel}} \neq 1$ holds, the application of dissolution phases in addition to growth phases does indeed widen the rage of attainable crystal shapes. In case of the growth and dissolution kinetics determined in this work, the application of growth-dissolution cycles can thus serve as a process strategy to enlarge the region of crystal shapes attainable by pure growth processes towards more elongated crystal shapes. This is illustrated in the right panel of Figure 3.23, where the region of crystal shapes attainable by growth was obtained for supersaturations in the rage of $1.09 \leq \mathrm{S_G} \leq 1.12$ at $T = 35$ °C. However, a crystal shape evolution towards octahedral crystal shapes cannot be realized with this cyclic process strategy. To obtain such a crystal shape, relative growth rates of $G_{\mathrm{rel}} > 1$ would be required (again assuming identical dissolution rates). This requirement is somewhat
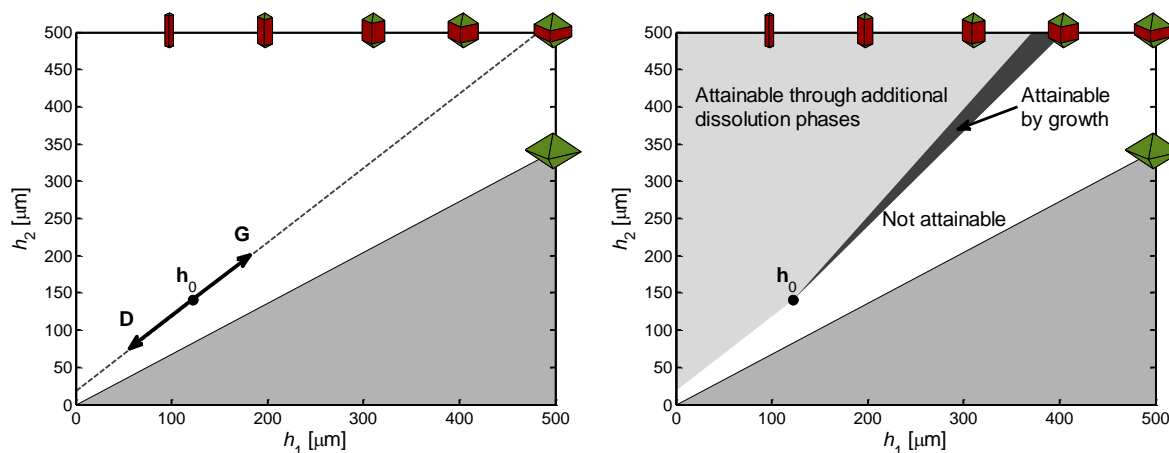
Figure 3.23: Regions of crystal shapes attainable by growth-dissolution cycles; left: attainable shapes, if $G_{rel} = D_{rel} = 1$; right: crystal shapes attainable with the kinetics of this work. Shapes that are attainable by pure growth with $1.09 \leq S_G \leq 1.12$ are indicated by a dark cone originating at h_0, while shapes attainable by additional dissolution phases are indicated by the light grey area.

relaxed compared to the condition of $G_{rel} > 1.465$ which need to be fulfilled in order to obtain octahedral crystal shapes from pure growth processes (see the discussion of Section 3.1). Yet, growth conditions leading to relative growth rates above one were not found in this work and the kinetics that were determined do not indicate the existence of such conditions.

3.6 Summary – Crystallization Kinetics

The kinetic phenomena of growth, nucleation and dissolution were investigated in this chapter for the KDP-water system during seeded batch crystallization processes. The face-specific growth kinetics of KDP were determined at constant levels of supersaturation and temperature in a range of $1.04 \leq S \leq 1.12$ and $25\ °C \leq T \leq 45\ °C$. The results of this study indicate that growth, in particular the growth of the prismatic {100}-faces, is influenced by the presence of impurities in the solution. This influence was, however, decreasing at higher levels of supersaturation. Hence, the growth kinetics were parameterized in this supersaturation region, where a linear dependence of the growth rates on the driving force was apparent.

Further evidence that impurities were indeed influencing the growth kinetics was collected in a separate analysis of the growth experiments. The observed supersaturation-dependencies of the growth rates were explained by a combination of the classical BCF theory (Burton 1951) for spiral growth and the step pinning mechanism developed by Kubota and Mullin (Kubota 1995, Kubota 2001). The resulting growth laws were used to derive a range of applicable supersaturation levels supersaturation for the concept of shape manipulation via growth-dissolution cycles.

The phenomenon of growth rate dispersion was visible throughout the growth experiments by a widening of the CSSD. It was shown that the random fluctuation model for growth rate dispersion is suitable to describe the observed evolution of the seed crystal population. The kinetics of the CSSD widening were again determined on a face-specific level, and a clear dependence of the growth rate diffusivities on the growth rates was found and parameterized by an empirical power law approach.

At higher supersaturation, also secondary nucleation was occurring. The kinetics of nucleation were parameterized by an empirical power law approach in conjunction with an Arrhenius approach to describe the temperature dependence. The analysis of the results indicate that mostly the seed crystal population contribute to the formation of thermodynamically stable molecular clusters, which indicate the importance of the fluid dynamics and crystal inertia on the phenomenon of secondary nucleation.

The final part of this chapter was dedicated to obtaining the face-specific dissolution kinetics of KDP. These kinetics were, as in the case of growth, determined for constant levels of undersaturation and temperature. In contrast growth, both face type dissolve with essentially identical rates under all investigated conditions, and no influence of impurities on the dissolution kinetics was visible. The dissolution rates were linearly dependent on undersaturation, and significantly faster than the growth rates at comparable driving forces. Both findings suggest, together with the observed ellipsoidal shape of the dissolving crystals, that dissolution is limited by bulk diffusion, and that the measured dissolution rates are in fact virtual dissolution rates. Finally, the obtained growth and dissolution kinetics were employed to derive the region of crystal shapes that are attainable by growth-dissolution cycles. The kinetics indicate that a cyclic crystallization process towards elongated crystal shapes is possible with this concept, whereas it is not possible to crystallize octahedral crystal shapes by growth-dissolution cycles.

4. Growth-Dissolution Cycles

The application of growth-dissolution cycles is a strategy frequently used during a batch crystallization process to increase the final crystal size and to decrease the amount of nucleated crystal at the same time, see for example Abu Bakar et al. (2009), Nagy et al. (2011), Griffin et al. (2015), or the recent review article of Wu et al. (2016). Due to the dissolution phases, nucleated crystal dissolve and the released solute is mainly depleted by growth of the seed crystal population during the next growth phase. In a further application, growth-dissolution cycles were also used for the purification of conglomerate forming enantiomeric systems with a fast racemization reaction (Suwannasang 2013, Suwannasang 2016). For this process, slight asymmetries in the growth behavior of both enantiomers were exploited to successively increase the enantiomeric excess of one of the enantiomers.

Next to the control of the crystal size distribution, growth-dissolution cycles were also proposed for the control of crystal shape (Snyder 2007b, Bunin 2010, Bajcinca 2013). Using growth-dissolution cycles for this purpose will also be the main topic of the discussion of this chapter. As shown by Lovette et al. (2012b), the region of crystal shapes attainable via growth-dissolution cycles can be enlarged compared to pure growth processes, rendering the application of growth-dissolution cycles a promising process concept for crystal shape control. Experimental realizations of this concept were demonstrated for single crystals by Lovette et al. (2012b). In batch crystallizations, growth-dissolution cycles were successfully applied for shape modifications of therephthalic acid (McElroy Brown 1989), monosodium glutamate (Jiang 2014a), succinic acid (Simone 2017) and KDP (Eisenschmidt 2015b). A further example was given by Kim et al. (2003), who realized a cyclic process consisting of growth, breakage and dissolution phases to control the size and shape of an active pharmaceutical ingredient originally crystallizing in a needle-like shape.

While the aforementioned authors used predefined temperature profiles to realize supersaturated and undersaturated conditions, it is the goal of this work to embed a cyclic growth-dissolution strategy in a process that is controlled in a closed loop manner. To this end, the feedback obtained from the measurements of the solution concentration and temperature as well as from measurements of the CSSD evolution is used to control the evolution of the mean seed crystal shape towards a desired target crystal shape. The required routines for this controller are described in this chapter.

In Section 4.1, the optimal control solution derived by Bajcinca (2013) and Bötschi (2017) are summarized and adjusted to the growth and dissolution kinetics presented in the previous chapter. As both optimal control solutions contain growth and dissolution phases at constant levels of supersaturation and undersaturation, Section 4.2 is dedicated to the control of supersaturation. A temperature profile of the thermostat is derived in this section on the basis of the process model described in Section 2.7. To compensate for any process disturbances, as for example nucleation, and uncertainties in the kinetics of the process model, the thermostat temperature profile was used as an input for a PI controller, which was found to

show a good performance in controlling the level of supersaturation. The supersaturation switches necessary for a cyclic growth-dissolution process are addressed in Section 4.3. The switching procedures are calculated to minimize the required switching times and to ensure that: i) a cyclic crystallization process between a minimal and maximal crystal volume and that ii) the desired target crystal shape can be attained with high precision. To improve the controllability of the entire cyclic crystallization process, the measurement noise of the observed mean crystal shape evolution is reduced in Section 4.4 by means of a Kalman filter. The experimental realization of controlled growth dissolution cycles is discussed in Section 4.5. The entire process could be well controlled with the strategies developed in the previous sections, and the desired target crystal shape could be reliably reached with high accuracy. Finally, Section 4.6 summarizes this chapter.

4.1 Optimal Control of Growth-Dissolution Cycles

The application of growth-dissolution cycles for the shape manipulation of crystal populations will naturally result in prolonged process times, as this strategy necessitates additional dissolution and growth phases as well temperature switches to change from supersaturated to undersaturated conditions and vice versa. It is therefore straightforward to optimize this cyclic process for a minimal required total process time. Thus, an optimal control problem has to be solved yielding the time optimal trajectory of the crystal population from an initial state $\mathbf{h}_0$ to a desired final state $\mathbf{h}_F$. This problem has been addressed by Bajcinca (2013) and the presented solution was used in this work as a basis for the control of crystal shapes by growth-dissolution cycles. Therefore, the approach of Bajcinca (2013) is briefly presented here and adapted to the crystallization kinetics determined earlier in this work.

Starting from the problem of finding an optimal supersaturation profile, constrained by upper and lower bounds, which allows for a time minimal trajectory from an initial point $\mathbf{h}_0$ to a final point $\mathbf{h}_F$, growth with a constant supersaturation level was found optimal by employing Pontryagin's minimum principle. Hence, no growth-dissolution cycles are required, provided that the final crystal shape can be reached from $\mathbf{h}_0$ by a pure growth process under the given constraints for supersaturation. If, however, the final crystal shape lies outside of the region which is attainable by growth, the application of growth-dissolution cycles was suggested. It was argued that the time optimal process, consisting of only one growth and one dissolution phase, requires a growth phase with constant supersaturation from $\mathbf{h}_0$ to a switching point $\mathbf{h}_S$ and a dissolution phase with a constant undersaturation from $\mathbf{h}_S$ to $\mathbf{h}_F$. Hence, the optimal control problem for a cyclic growth-dissolution process was reduced to a parameter optimization problem with just two decision parameters, which can be formulated in two equivalent ways. In the first formulation, the supersaturation levels are optimized with respect to the upper and lower bounds, whereas in the second formulation, the position of the switching point $\mathbf{h}_S$ is optimized, provided that $\mathbf{h}_S$ can be attained by a growth process from $\mathbf{h}_0$ and that $\mathbf{h}_F$ can be reached from $\mathbf{h}_S$ during dissolution, see Figure 4.1.
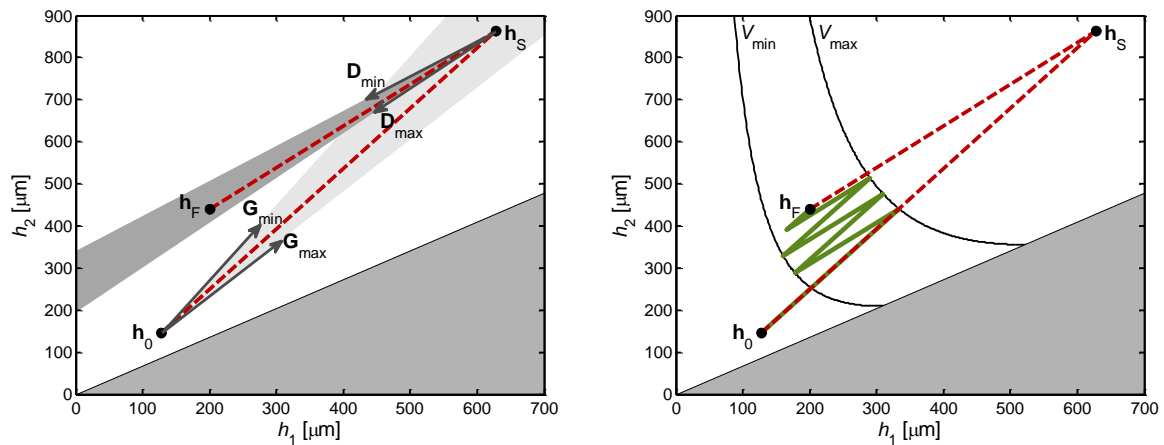
Figure 4.1: Time optimal trajectories for a cyclic growth-dissolution process according to Bajcinca (2013); left: Solution for a single switch scenario, attainability regions for growth and dissolution are indicated by light gray and dark gray cones originating from $\mathbf{h}_0$ and $\mathbf{h}_S$ respectively; right: Solution for a multiple switch scenario resulting from constraints on minimal and maximal crystal volume.

As can be seen from the left panel of Figure 4.1, a growth-dissolution process can, in an ideal case, be realized with a single switch from growth to dissolution. Such a scenario would require that the crystals could be grown until $\mathbf{h}_S$ is reached. However, it is possible that the single switch strategy results in rather high values for $\mathbf{h}_S$ (as for instance in the case of Figure 4.1). Hence, the realization of such a trajectory might not be feasible. In practice, the maximal mean crystal shape is limited, e.g. by the solubility, the limited cooling power of the thermostat or the danger of blockage of the microscope. Hence, crystals can only be grown to a maximal size V_{max} and thus several growth and dissolution phases might be required. Of course, also the minimal crystal volume is limited, as at some point the smallest crystals of the seed population would dissolve completely. To avoid any of these disturbances, the volume constraints were in this work set to $V_{min} = 0.072$ mm^3 and $V_{max} = 0.352$ mm^3 respectively.

The optimization approach of Bajcinca (2013) is based on the assumptions, that temperature – and thus supersaturation switches can be performed instantaneously, and that the growth and dissolution kinetics are independent on temperature. With these assumptions, the solution of the single switch scenario described above also solves the optimal control problem in case of a multiple switching scenario. In this case, the single growth and dissolution phases are split into several growth and dissolution phases such that the evolution of the CSSD remains within a certain region of the $\mathbf{h}$-space. In this work, the crystal volume was confined by a maximal and minimal crystal volume (V_{max}, V_{min}), leading to optimal crystal shape trajectories as depicted in the right panel of Figure 4.1. The optimal control profiles for this case are depicted in Figure 4.2, for a target crystal shape of $\mathbf{h}_F = [200 \; \mu m, 440 \; \mu m]^T$, where the constraints for supersaturation were set to: $1.10 \leq S_G \leq 1.12$ and $0.99 \leq S_D \leq 0.975$. The initial temperature was set to 35 °C and the initial CSSD had a Gaussian distribution with $\overline{\mathbf{h}}_0 = [128 \; \mu m, 146 \; \mu m]^T$, $\boldsymbol{\sigma}_0 = [25 \; \mu m, 25 \; \mu m]^T$ and an initial mass of $m_0 = 0.8$ g. As can be seen, the constraints on minimal and maximal crystal volume are resulting in a process that is
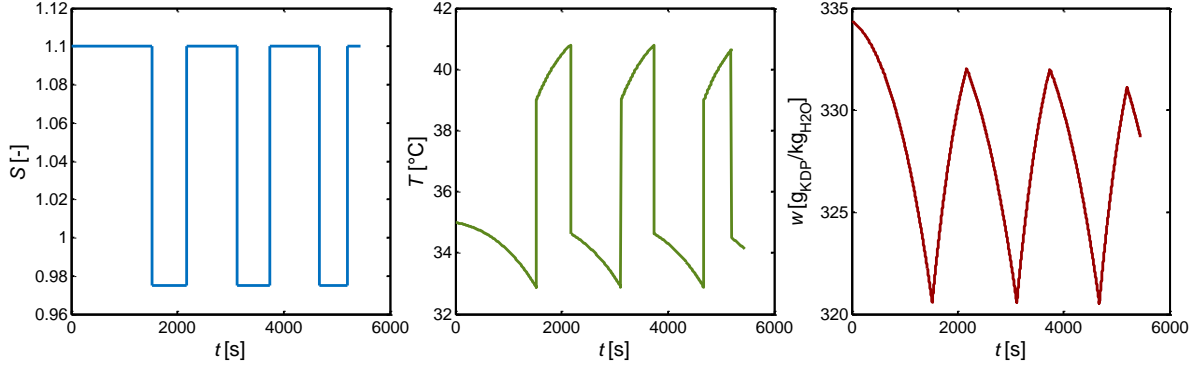
Figure 4.2: Optimal control profiles for a cyclic growth-dissolution process according to Bajcinca (2013); left: Optimal supersaturation profile; middle: Temperature profile required to realize the supersaturation profile; right: Resulting concentration profile.

cycling between a minimal and maximal solute concentration. Furthermore, the temperature profiles during growth and dissolution are bounded by upper and lower values.

The optimization approach presented by Bajcinca (2013) assumes temperature independent kinetics, or negligible temperature gradients during growth and dissolution, but does not rely on any specific formulation of the growth or dissolution kinetics. Here, the approach is illustrated on the example of power law formulations for both kinetics. Therefore, the expressions derived therein are adjusted to account for the linear and temperature dependent growth and dissolution kinetics determined in Chapter 3 of this work. With these kinetics, the optimal control problem can be formulated as follows:

$$\min_{\mathbf{h}_S} \ (t_G + t_D) \tag{4.1a}$$

$$\text{s.t.} : \quad S_{G,min} \le S_G \le S_{G,max} \tag{4.1b}$$

$$\phantom{\text{s.t.} : \quad} S_{D,min} \le S_D \le S_{D,max} \ . \tag{4.1c}$$

To evaluate the objective function and to check whether the inequality conditions are fulfilled, the times for growth and dissolution t_G and t_D as well as supersaturation levels S_G and S_D have to be calculated in dependence of the switching point $\mathbf{h}_S$. This can be done via the following equations:

$$S_G = \frac{S_{G,1}^*(\bar{T}_G) - K_G(\bar{T}) S_{G,2}^*(\bar{T}_G)}{1 - K_G(\bar{T})} \tag{4.2a}$$

$$S_D = \frac{S_{D,1}^*(\bar{T}_D) - K_D(\bar{T}) S_{D,2}^*(\bar{T}_D)}{1 - K_D(\bar{T})} \tag{4.2b}$$

$$t_G = \frac{h_{S,1} - h_{0,1}}{k_{G,1}(\bar{T}_G)(S_G - S_{G,1}^*(\bar{T}_G))} \tag{4.2c}$$

$$t_D = \frac{h_{F,1} - h_{S,1}}{k_{D,1}(\bar{T}_D)(S_D - S_{D,1}^*(\bar{T}_D))} . \tag{4.2d}$$

Here, the constants K_G and K_D can be calculated from:

$$K_G(\overline{T}) = \frac{h_{S,1} - h_{0,1}}{h_{S,2} - h_{0,1}} \frac{k_{G,2}(\overline{T}_G)}{k_{G,1}(\overline{T}_G)} \tag{4.3a}$$

$$K_D(\overline{T}) = \frac{h_{F,1} - h_{S,1}}{h_{F,2} - h_{S,2}} \frac{k_{D,2}(\overline{T}_D)}{k_{D,1}(\overline{T}_D)}. \tag{4.3b}$$

In order to evaluate Eqs. (4.2) and (4.3) on the basis of the growth and dissolution kinetics determined in Sections 3.1 and 3.5, some information about the growth and dissolution temperature has to be available. These temperatures can be estimated prior to optimization on the basis of the minimal and maximal crystal volume as well as on the basis of the upper and lower bounds on the applicable levels of supersaturation and undersaturation, respectively. An average growth and dissolution concentration can be obtained from the minimal and maximal crystal volumes by:

$$\overline{w} = w(t = 0) + \frac{m_{seed}}{m_{H_2O}} - \frac{V_{sus} \mu_{0,0} \rho_{KDP}(V_{min} + V_{max})}{2m_{H_2O}}. \tag{4.4}$$

With this average concentration, the maximal and minimal (average) temperatures for growth and dissolution can be calculated by solving:

$$\overline{w} - S_{G,max} w_{eq}(T_{G,max}) = 0 \tag{4.5a}$$

$$\overline{w} - S_{G,min} w_{eq}(T_{G,min}) = 0 \tag{4.5b}$$

$$\overline{w} - S_{D,max} w_{eq}(T_{D,min}) = 0 \tag{4.5c}$$

$$\overline{w} - S_{D,min} w_{eq}(T_{D,max}) = 0. \tag{4.5d}$$

The average growth and dissolution temperatures can then be estimated on the basis of the maximal and minimal temperatures by:

$$\overline{T}_G = \frac{T_{G,max} + T_{G,min}}{2} \tag{4.6a}$$

$$\overline{T}_D = \frac{T_{D,max} + T_{D,min}}{2}. \tag{4.6b}$$

Clearly, neglecting the temperature profiles during growth and dissolution constitutes in general a coarse approximation of the process dynamics. However, as the seed loadings and hence suspensions densities used in this work were chosen to be rather small, the temperature gradients during growth and dissolution are expected to be small as well. Therefore, the approximation of the temperature profiles by constants may be considered reasonable. This way, by assuming constant temperatures or equivalently temperature independent crystallization kinetics, the evolution of the crystal population is decoupled from the state of the liquid phase. Therefore, the optimization problem Eq. (4.1) can be solved efficiently without the necessity for solving the coupled population balance model of Section 2.7.

The time-optimal control of a cyclic growth-dissolution process assuming non-constant temperature profile has recently been considered by Bötschi et al. (2017). This work uses the same kinetics as presented here, by explicitly accounting for the temperature dependencies of the growth and dissolution kinetics. The authors again assume that supersaturation switches can be performed instantaneously. The results of this study indicate that:

(i)   Constant levels of supersaturation and undersaturation are optimal for the individual growth and dissolution phases.

(ii)   Both, growth and dissolution processes should be conducted at the highest temperatures possible, to maximize the growth and dissolution rate constants. This result implies, for the case of an unconstrained number of switches, that a cyclic process at the minimal valid crystal volume is optimal. In the extreme case this yields growth and dissolution phases with infinitesimal lengths, until a final growth phase is performed, to reach the target crystal shape $\mathbf{h}_F$.

(iii) The levels of supersaturation and undersaturation identified by Bajcinca (2013) are as well optimal for the case studied by Bötschi et al. (2017). This appears to be also the case if the solute mass is decreased, which leads to an increase of the suspension density and thereby also to more pronounced temperature profiles during the growth and dissolution phases.

The assumption of instantaneous temperature or supersaturation switches can, of course, not be met in real crystallization processes. Instead, the switching times are quite significant (approximately 500 to 700 seconds, see Sections 4.3 and 4.5). Hence, the potential gain in process time that results from a higher number of supersaturation switches is most likely overcompensated by the additional switching times that are required in this case. For this reason, the approach of Bajcinca (2013) that minimizes the total number of temperature switches for an optimal set of supersaturation and undersaturation levels was further pursued in this work.

4.2 Supersaturation Control

Control of supersaturation is a strategy frequently used to control crystallization processes (see for example Ward et al. (2006) and references therein) to balance the tradeoff between high crystal growth rates and thus high productivities and the occurrence of unwanted primary and/or secondary nucleation. Note that the latter are phenomena typically correlating in a nonlinear manner with supersaturation (see also Section 3.4). In this work, the realization of constant supersatuation profiles is of particular importance for the realization of a time-optimal cyclic crystallization process; see the discussion in the previous section. The realization of constant supersaturation profiles are of similar importance for the determination of the growth and dissolution kinetics of KDP (see Chapter 3). To obtain a constant level of supersaturation during a seeded batch crystallization process, Mullin and Nývlt (1971)

derived an equation for the crystallizer temperature profile over time which has to be realized. The derivations were based on the method of moments, and were adapted by Eisenschmidt et al. (2015a) to account for faceted crystals. The resulting differential equation was used in this work as a basis for the closed-loop control of supersaturation. For this purpose the model equations for the crystallizer and jacket temperatures (Eq. (2.28)) have been inverted to yield a set-point temperature profile for the thermostat which has to be applied to obtain a constant supersaturation profile over time. This set-point temperature profile was finally used to construct a PI supersaturation controller which has been tested for some model uncertainties that can be expected during the crystallization experiments.

To maintain a constant level of supersaturation, the concentration changes over time that are caused by crystal growth or dissolution, have to be compensated by changes in the equilibrium concentration, and thus by a change in the crystallizer temperature. To derive an equation for the required changes of the crystallizer temperature, the total derivative of the supersaturation with respect to time can be used:

$$\frac{dS}{dt} = \frac{1}{w_{eq}}\frac{dw}{dt} - \frac{w}{w_{eq}^2}\left(\frac{\partial w_{eq}}{\partial T_C}\right)\frac{dT_C}{dt} \, . \tag{4.7}$$

Clearly, the left hand side of Eq. (4.7) has to be zero, to maintain a constant level of supersaturation. Rearranging and using the empirical solubility correlation of Eq. (2.2) then yields:

$$\frac{dT_C}{dt} = \frac{\dfrac{1}{S}\dfrac{dw}{dt}}{\dfrac{dw_{eq}}{dT_C}} = \frac{\dfrac{1}{S}\dfrac{dw}{dt}}{2c_{eq,1}T_C + c_{eq,2}} \, . \tag{4.8}$$

Thus the differential equation (4.8) for the crystallizer temperature has to be fulfilled to achieve a constant supersaturation level during the growth or dissolution phases. In order to realize this, an appropriate temperature profile has to be applied to the thermostat connected to the double jacket of the crystallizer. This thermostat temperature profile is derived from the model equations for the temperatures of the crystallization vessel given in Eqs. (2.28) of Section (2.7). Assuming constant heat capacities and solution densities, these differential equations can be formulated as:

$$\frac{dT_C}{dt} = a_1 T_G + a_2 T_S - a_3 T_C + a_4 \frac{dm_{KDP}}{dt} \tag{4.9a}$$

$$\frac{dT_S}{dt} = b_1 T_G - b_2 T_S + b_3 T_C + b_4 \tag{4.9b}$$

$$\frac{dT_G}{dt} = c_1 T_{Th} - c_2 T_G + c_3 T_C + c_4, \tag{4.9c}$$

with constant coefficients a_i, b_i and c_i. As can be seen, the thermostat temperature T_{Th} is appearing explicitly on the right hand side of Eq. (4.9c). However, to solve this equation for T_{Th}, the temperature change in bottom element of the double jacket dT_G/dt has to be known.

This information is obtained by forming the second order derivative of the crystallizer temperature with respect to time d^2T_C/dt^2 using Eq. (4.8) and Eq. (4.9a) respectively:

$$\frac{d^2T_C}{dt^2} = \frac{1}{S}\frac{\dfrac{d^2w}{dt^2}\dfrac{dw_{eq}}{dT_C} - \dfrac{dw}{dt}\dfrac{d}{dt}\left(\dfrac{dw_{eq}}{dT_C}\right)}{\left(\dfrac{dw_{eq}}{dT_C}\right)^2} = \frac{1}{S}\frac{\dfrac{d^2w}{dt^2}\left(2c_{eq,1}T_C + c_{eq,2}\right) - 2c_{eq,1}\dfrac{dw}{dt}\dfrac{dT_C}{dt}}{\left(2c_{eq,1}T_C + c_{eq,2}\right)^2} \quad (4.10a)$$

$$\frac{d^2T_C}{dt^2} = a_1\frac{dT_G}{dt} + a_2\frac{dT_S}{dt} - a_3\frac{dT_C}{dt} + a_4\frac{d^2m_{KDP}}{dt^2}. \quad (4.10b)$$

In order to evaluate Eqs. (4.10a) and (4.10b), the derivatives dw/dt, d^2w/dt^2 and d^2m_{KDP}/dt^2 need to be known. While dw/dt can be readily obtained from Eq. (2.27), both second order derivatives, d^2w/dt^2 and d^2m_{KDP}/dt^2, can be calculated by:

$$\frac{d^2m_{KDP}}{dt^2} = -\rho_{KDP}V_{sus}\left(10.948\frac{d^2\mu_{2,1}}{dt^2} - 4.983\frac{d^2\mu_{3,0}}{dt^2}\right) \quad (4.11a)$$

$$\frac{d^2w}{dt^2} = \frac{1}{m_{H_2O}}\frac{d^2m_{KDP}}{dt^2}. \quad (4.11b)$$

Using the assumption of a constant supersaturation, the second order derivatives of the moments $\mu_{2,1}$ and $\mu_{3,0}$, appearing in Eq. (4.11a) can be determined as follows:

$$\frac{d^2\mu_{2,1}}{dt^2} = \frac{d}{dt}\left(2G_1\mu_{1,1} + G_2\mu_{2,0}\right)$$
$$= 2\left(\left(\frac{\partial G_1}{\partial T_C}\right)\frac{dT_C}{dt}\mu_{1,1} + G_1\left(G_1\mu_{0,1} + G_2\mu_{1,0}\right)\right) + \left(\frac{\partial G_2}{\partial T_C}\right)\frac{dT_C}{dt}\mu_{2,0} + 2G_2^2\mu_{1,0} \quad (4.12)$$

and

$$\frac{d^2\mu_{3,0}}{dt^2} = \frac{d}{dt}\left(3G_1\mu_{2,0}\right) = 3\left(\left(\frac{\partial G_1}{\partial T_C}\right)\frac{dT_C}{dt}\mu_{2,0} + 2G_1^2\mu_{1,0}\right). \quad (4.13)$$

Note, that while both equations (4.12) and (4.13) are defined for growing crystals, they are applicable for dissolving crystals in the same way. However, the distinction between growth and dissolution is skipped in this section for the sake of brevity. With the set of differential equations given above, Eq. (4.10a) can be evaluated and inserted into Eq. (4.10b), which in turn can be rearranged such that the derivative dT_G/dt reads:

$$\frac{dT_G}{dt} = \frac{1}{a_1}\frac{d^2T_C}{dt^2} - \frac{a_2}{a_1}\frac{dT_S}{dt} + \frac{a_3}{a_1}\frac{dT_C}{dt} - \frac{a_4}{a_1}\frac{d^2m_{KDP}}{dt^2}. \quad (4.14)$$

Finally, this equation can be used, to solve Eq. (4.9c) for the thermostat temperature T_{Th}:
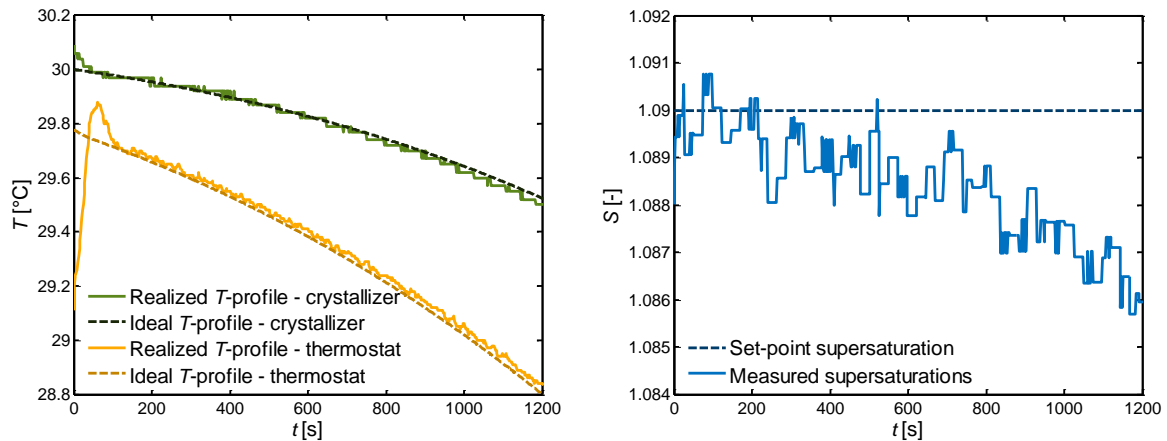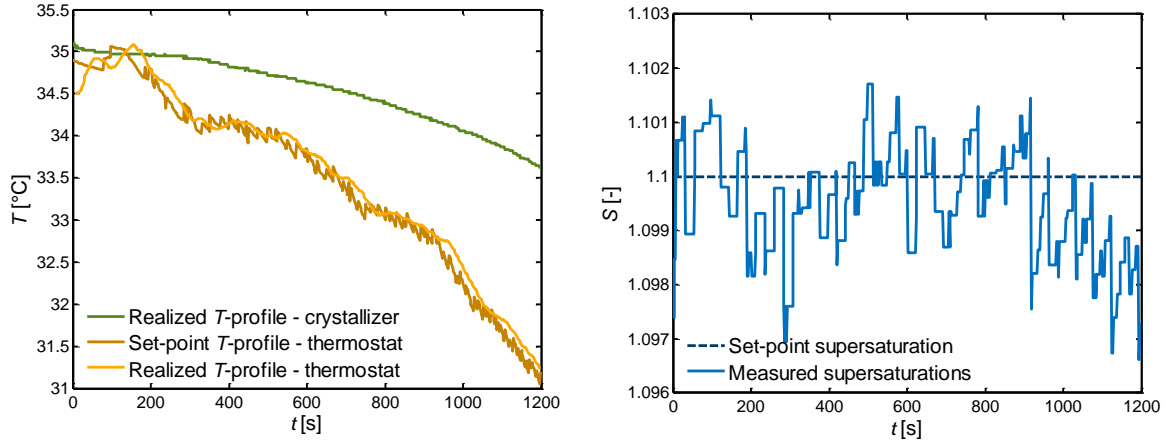
Figure 4.3: Open loop supersaturation control using Eq. (4.15), left: Temperature profiles of the crystallizer and thermostat (green dashed and yellow dashed) calculated by Eqs. (4.8) and (4.15) respectively, and measured crystallizer and thermostat temperature profiles (green solid and yellow solid), right: Measured supersaturation profile (solid line) and set-point supersaturation level (dashed line).

$$T_{\text{Th}} = \frac{1}{c_1} \frac{dT_{\text{G}}}{dt} + \frac{c_2}{c_1} T_{\text{G}} - \frac{c_3}{c_1} T_{\text{C}} - \frac{c_4}{c_1} \, . \tag{4.15}$$

This equation provides the required thermostat temperature profile guaranteeing a constant level of supersaturation. Given a complete set of dynamical variables (moments of the crystal shape distribution, solution concentration and crystallizer temperatures), the equation can be evaluated during or after every time integration step to yield a profile of the thermostat temperature to be applied in order to maintain the level of supersaturation constant during the crystallization process.

An application of supersaturation control via Eq. (4.15) is depicted in Figure 4.3, with the dashed green and dashed yellow lines being the solutions of Eqs. (4.8) and (4.15) respectively. The realized crystallizer and thermostat temperature profiles are shown as solid green and yellow lines. It can be seen, that the required thermostat temperature profile can be realized with high precision. The resulting profile of the crystallizer temperature matches the solution of Eq. (4.8) accurately as well. Consequently, the supersaturation level could be controlled reasonably well. However, after about 600 seconds, the supersaturation level starts to decrease, which can be attributed to uncertainties in the crystallization kinetics and heat transfer coefficients. As some nucleation was observed during this experiment, the consumption of supersaturation by growth of those nuclei can be another explanation for the decrease in supersaturation, as this effect is not covered by the population balance model used for solving Eq. (4.15).

To further improve the performance of the supersaturation controller, Eq. (4.15) is used as a basis to design a PI supersaturation controller. This controller corrects the thermostat temperature according to:
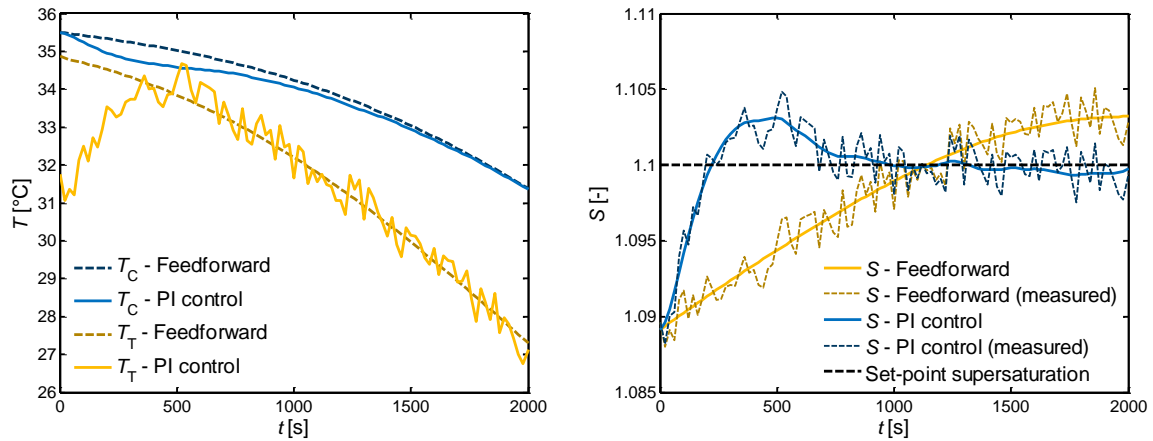
Figure 4.4: Closed loop supersaturation control using Eq. (4.16), left: realized crystallizer temperature profile (green) together with the set-point (dark yellow) and realized thermostat temperature profile (yellow), right: measured supersaturation profile (solid line) and set-point supersaturation level (dashed line).

$$T_{\mathrm{Th,PI}} = T_{\mathrm{Th,mod}} - \left[K_{\mathrm{p}}(S_{\mathrm{set}} - S) + \frac{1}{T_{\mathrm{N}}} \int_0^t (S_{\mathrm{set}} - S(\tau)) d\tau \right], \quad (4.16)$$

where $T_{\mathrm{Th,PI}}$ denotes the corrected set-point value for the thermostat temperature and $T_{\mathrm{Th,mod}}$ denotes the thermostat temperature calculated by Eq. (4.15). To obtain a satisfactory controller performance, the values of the controller parameters were set to: $K_{\mathrm{p}} = 300$ K and $T_{\mathrm{N}} = 1.33$ s/K and used throughout this work. An application of this controller on a crystal growth process is exemplarily shown in Figure 4.4. As can be seen, the supersaturation level could be tightly controlled with small oscillations, having an amplitude that is only slightly higher than the observed measurement noise of the supersaturation around the set-point value. The described oscillations were compensated by the controller within a time range of 200 seconds. Compared to the open loop supersaturation control depicted in Figure 4.3, the PI supersaturation control shows a significantly better performance. This is even more evident, when the crystallization conditions are considered as well, which were set to a higher supersaturation as well as to a higher temperature. Therefore, the uncertainties in growth kinetics as well as occurring nucleation are expected to have an even stronger influence on the supersaturation profile. However, they are compensated by the controller defined by Eq. (4.16).

Although the results of Figure 4.4 were showing a good performance of the controller in the experimental practice, further tests of the controller were necessary in order to ensure that any unexpected perturbations of the crystallization process could be well compensated. To provide such test scenarios, a series of simulated experiments were performed, where different kinds of disturbances, which can be expected during the cyclic crystallization experiments, were considered. To test the behavior of the controller in those scenarios, a random white noise with a standard deviation of 0.1% (in terms of supersaturation) was added to the simulated supersaturation measurements (represented as thin lines in the right
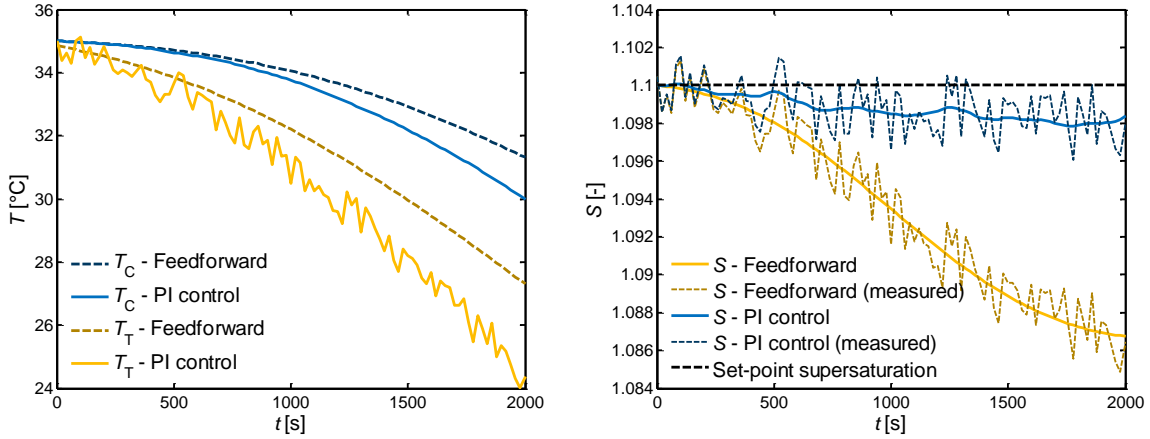
Figure 4.5: Supersaturation control in case of an initial temperature offset. Left: Temperature profiles of the crystallizer (blue) and thermostat (yellow) using the open loop control of Eq. (4.15) (dashed) and the closed loop control (solid) of Eq. (4.16). Right: resulting supersaturation profiles of the open loop control (yellow) and the closed loop control (blue), together with the simulated supersaturation measurements (thin lines) and the set-point supersaturation level (dashed line).

panels of Figures 4.5 and 4.6). Thus, the simulated measurement noise was slightly higher compared to the experimentally observed noise (see Figure 4.4, right). The rate with which the supersaturation measurements are available was simulated to be 30 s, and therefore also slightly above the experimentally realized measurement rate (about 20 s per measurement), to test the controller performance in a 'worst-case' scenario with respect to the quality of the supersaturation measurements.

In a first case study, an initial temperature offset of 0.5 °C is considered, mimicking an imperfect temperature switch from dissolution to growth conditions in the cyclic crystallization process. This temperature offset translates to a supersaturation which is approximately 1 % below the set-point value of 1.10. As can be seen in Figure 4.5, the application of the open loop control of Eq. (4.15) does not correct the initial supersaturation offset. The PI-supersaturation controller is however able to reach − and further to maintain the desired level of supersaturation. Some mild overshooting in supersaturation (in the range of 0.25%) can be observed after 300 seconds until the supersaturation reaches the desired set-point level after 900 seconds.

In a second case study, the pre-exponential factors $k_{0,\mathrm{G},i}$ of the growth kinetics were increased by 10% of their original value. Hence, the solute consumption by growth was higher than predicted by the model used to calculate the thermostat temperatures. The resulting temperature and supersaturation profiles are depicted in Figure 4.6. During the first 200 seconds, no substantial deviation of both supersaturation profiles from the set-point value can be observed. This is due to the relatively small crystal sizes at this time. The small crystal sizes were accompanied by small surface area that were available for growth, and hence, solute consumption. As the crystals grew larger in size after, also the crystals surface areas were increased which resulted in a decrease of both supersaturation profiles due to the perturbed growth rates. While the supersaturation profile of the open loop control is decreasing monotonically to a value of $S = 1.087$ at the end of the simulation time, the

Figure 4.6: Supersaturation control in case of perturbed growth kinetics. Left: Temperature profiles of the crystallizer (blue) and thermostat (yellow) using the open loop control of Eq. (4.15) (dashed) and the closed loop control (solid) of Eq. (4.16). Right: resulting supersaturation profiles of the open loop control (yellow) and the closed loop control (blue), together with the simulated supersaturation measurements (thin lines) and the set-point supersaturation level (dashed line).

supersaturation profile of the closed loop control levels off at a value of about 1.098. As the difference of this level to the set-point value is only slightly higher than the measurement noise considered in this simulation, the controller performance was considered to be sufficient in this simulation experiment.

The simulation results described above, as well as the experimental results shown in Figure 4.4, demonstrate the effectiveness of the developed controller in maintaining a level of supersaturation or undersaturation constant. However, the area of optimal crystallization control by temperature and thus supersaturation control stretches far beyond the pure control of a constant supersaturation. For example, Ward and coworkers (Ward 2006, Tseng 2017) investigated the dependence of the optimal supersaturation profile on the objective function chosen for optimization. Next to constant supersaturation profiles as discussed here, the authors classified the optimal profiles as early growth strategies (Ma 2003, Ward 2006, Tseng 2017), minimizing the number of nuclei formed in a fixed crystallization time, or as late growth strategies (Feng 2002, Ward 2006, Hofmann 2010, Tseng 2017) minimizing the total mass of nuclei formed during a crystallization process.

Although the presented approach for supersaturation control is solely focused on constant supersaturation profiles, it has to be emphasized that this approach can be easily adapted to control any differentiable supersaturation profile. For this purpose the non-zero (and possibly time dependent) left hand side of Eq. (4.7) has to be taken into account, which would yield different formulations of Eqs. (4.8) and (4.10a). Furthermore, Eqs. (4.12) and (4.13) would have to be adjusted, as the derivatives of the growth rates G_i with respect to time have to be calculated by:

$$\frac{dG_i}{dt} = \left(\frac{\partial G_i}{\partial T_C}\right)\frac{dT_C}{dt} + \left(\frac{\partial G_i}{\partial S}\right)\frac{dS}{dt}, \qquad (4.17)$$

with a non-negligible second term on the right hand side. Accounting for these adjustments, the framework given by Eq. (4.15) and Eq. (4.16) is also applicable for the control of non-constant supersaturation profiles, e.g., for the supersaturation switches discussed in the next section. However, as the constraints on the maximal heating or cooling power of the thermostats would lead to prolonged switching times, a different approach based on the use of two thermostats was used in this work.

4.3 Supersaturation Switches

Besides the control of supersaturation, described in the previous section, a cyclic growth-dissolution process naturally involves switching phases from growth to dissolution conditions and vice versa. While these supersaturation switches can be achieved by different means, such as, the addition of clear supersaturated or undersaturated solution from separate feedstocks, or the addition of antisolvent, this work is solely focused on changing the solution temperature, and thereby changing the equilibrium concentration. Hence, in this work supersaturation control was achieved by controlling the solution temperature solely.

Since this work focuses on controlling the evolution of the CSSD during a cyclic growth-dissolution process in a time-optimal manner, it is straightforward to require the necessary supersaturation switches to be time-minimal as well. In order to optimize these switching phases, the process model was equipped with one additional differential equation for each thermostat, describing the temperature-dynamics of this thermostat:

$$\frac{dT_{\mathrm{Th},i}}{dt} = \frac{\dot{m}_{\mathrm{Th},i}}{m_{\mathrm{Th},i} c_{\mathrm{p,H_2O}}} \left(T_{\mathrm{S}} + T_{\mathrm{Th},i} \right) + \frac{P_{\mathrm{Th},i}}{m_{\mathrm{Th},i} c_{\mathrm{p,H_2O}}} . \tag{4.18}$$

The first term on the right hand side of this equation describes the temperature change due to the incoming and outgoing mass flow, whereas the second term represents the heating or cooling of the thermostat bath with the power $P_{\mathrm{Th},i}$. The maximal heating power and cooling power of the thermostats $P_{\mathrm{Th,max}}$ and $P_{\mathrm{Th,min}}$ are, of course, of strong importance for the optimization of the supersaturation switches, and were thus determined in preliminary experiments. In these experiments, the maximal cooling power $P_{\mathrm{Th,min}}$ exhibited a slight temperature dependence:

$$P_{\mathrm{Th,max}} = 1750\,\mathrm{W} \tag{4.19a}$$
$$P_{\mathrm{Th,min}} = -430\,\mathrm{W} + 2\,\mathrm{W/°C} \times T_{\mathrm{Th}}, \tag{4.19b}$$

where T_{Th} is the thermostat temperature in °C. These powers correspond to a maximal heating rate of approximately 4 °C/min and a maximal cooling rate of roughly -0.8 °C/min for a typical mass of the thermostat bath of $m_{\mathrm{TH}} = 6.5$ kg. It is obvious that the maximal heating rate is significantly higher than the maximal cooling rate, an observation of particular importance for the optimization of the switching phases.

Clearly, a time-optimal supersaturation or temperature switch requires the application of maximal driving forces over time. However, it needs to be ensured that the supersaturation level remains constant during the preceding growth or dissolution phase. This was realized by requiring the derivative dS/dt to be zero at the final switching time, which necessitated a final cooling or heating phase for switches from growth to dissolution or from dissolution to growth respectively. Additionally, the crystal shape trajectory was confined by the minimal and maximal volume of the mean seed crystal size V_{min} and V_{max}. In order not to violate these constraints, the time at which the switching procedure was initiated was chosen such that the minimal or maximal volume of the mean seed crystal during the supersaturation switch was equal to V_{min} or V_{max} respectively. For the first switches from growth to dissolution and from dissolution to growth, this was achieved by simulating the CSSD evolution during the switching time with the kinetic expressions of Eq. (3.7) and Eq. (3.33). Due to the uncertainties in the growth kinetics at low supersaturations however (see Section 3.1 and 3.2), this approach was not further pursued at later switches. Instead, the measured CSSD evolution of the previous supersaturation switch was used for the determination of the next switching time. Accounting for all these constraints, the optimal switching procedure from dissolution to growth could be obtained by solving the optimization problem:

$$\min_{t_0, t_S} t_F \tag{4.20a}$$

$$\text{s.t.:} \quad S(t_F) = S_{set} \tag{4.20b}$$

$$P_{Th}(t < t_S) = P_{Th,min}(T) \tag{4.20c}$$

$$P_{Th}(t \geq t_S) = P_{Th,max} \tag{4.20d}$$

$$\min V(\overline{\mathbf{h}}(t)) = V_{min} \tag{4.20e}$$

$$\left. \frac{dS}{dt} \right|_{t=t_F} = 0. \tag{4.20f}$$

As can be seen from these equations, the thermostat was cooled from an initial temperature with maximal power. This indicates that a further decrease in the initial thermostat temperature would have been beneficial to further decrease the total switching time. Therefore, the thermostat temperature was decreased in the previous dissolution phase to a minimal value. After the time t_S that solve the optimization problem of Eq. (4.20), the thermostat was heated with maximal power to ensure that the constraint (4.20f) could be fulfilled at the final switching time t_F.

The experimentally realized temperature and supersaturation profiles for a switch from dissolution to growth are exemplarily shown in Figure 4.7. As can be seen from the temperature profiles, shown in the left panel of this figure, a strong increase in the thermostat temperature was initially observable, which was due to the mass flow from the double jacked, with a temperature of about 42 °C, to the thermostat. The measured temperature profile of the cooling thermostat exhibited slight deviations to the model predictions in this initial phase, which can be attributed to a flow profile in the cooling jacked whose complexity was not fully captured by the model equations. However, the mismatch between measurements and model predictions was quickly decreasing, and the predicted temperature profile of the
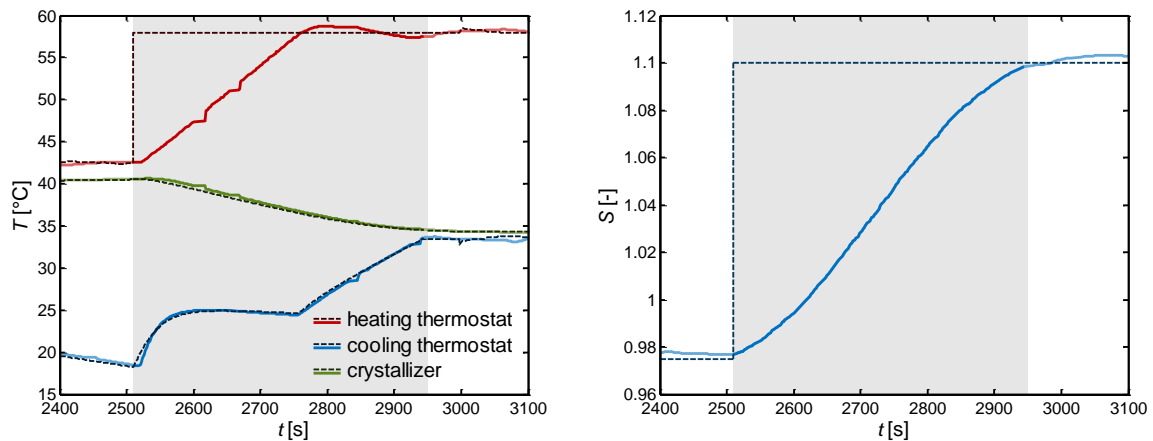
Figure 4.7: Experimentally realized supersaturation switch from growth to dissolution conditions; left: Profiles of the heating thermostat temperature (red), the suspension temperature (green) and the cooling thermostat temperature (blue); right: Supersaturation profile over time. The switching period is indicated by light gray areas, and measured profiles are marked with thick solid lines while computed profiles of set-point values are represented by dark dashed lines.

crystallizer could be well reproduced. At $t = 2750$ s, the final heating phase was initiated which led to an inflection point in the supersaturation and crystallizer temperature profiles. Finally, the set-point supersaturation of $S = 1.10$ could be realized quite accurately with only a slight overshoot.

In case of supersaturation switches from growth to dissolution conditions, the optimal switching policy was slightly different to Eq. (4.20). Due to the comparably high heating power, the initial thermostat temperature could be raised to values which were sufficiently high to omit an initial heating phase during the switching procedure. Hence, the initial thermostat temperature was determined alongside with the starting time by solving:

$$\min_{t_0, T_{Th,0}} t_F \tag{4.21a}$$

$$\text{s.t.:} \quad S(t_F) = S_{set} \tag{4.21b}$$

$$P_{Th} = P_{Th,min}(T) \tag{4.21c}$$

$$\max V(\overline{\mathbf{h}}(t)) = V_{max} \tag{4.21d}$$

$$\left. \frac{dS}{dt} \right|_{t=t_F} = 0. \tag{4.21e}$$

Note, that the process model equations Eq. (2.20), Eq. (2.27) and Eq. (2.28) had to be fulfilled as well in both optimization problems. For the sake of brevity, these equations are not explicitly given here.

The experimentally realized temperature and supersaturation profiles for a switch from growth to dissolution (depicted in Figure 4.8) showed trends as for the previously discussed switched from dissolution to growth. Again, the predicted temperature profile of the crystallizer could be well realized apart from slight initial deviations. A small overshoot in the temperature of the heating thermostat is visible at $t = 1800$ s. This overshoot was due to
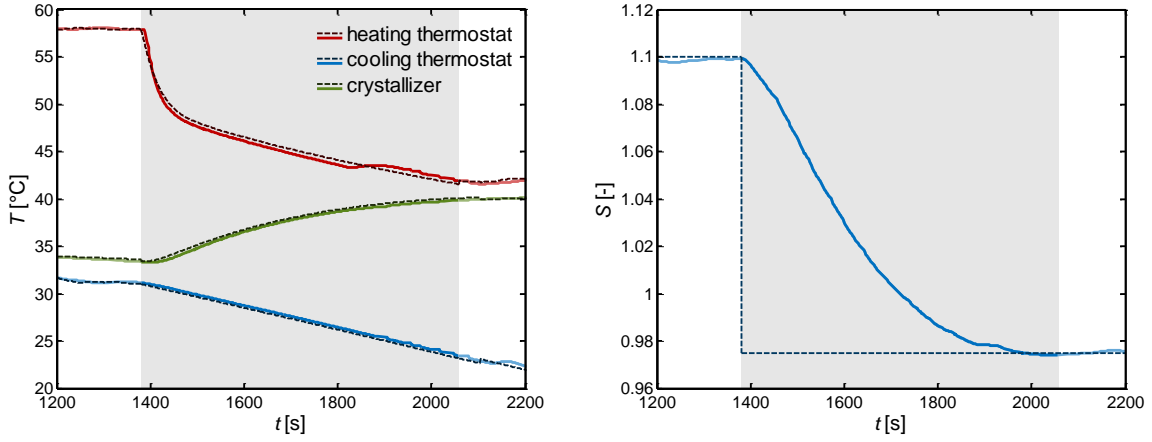
Figure 4.8: Experimentally realized supersaturation switch from dissolution to growth conditions; left: Profiles of the heating thermostat temperature (red), the suspension temperature (green) and the cooling thermostat temperature (blue); right: Supersaturation profile over time. The switching period is indicated by light gray areas, and measured profiles are marked with thick solid lines while computed profiles of set-point values are represented by dark dashed lines.

the PI controller of the thermostat, controlling the thermostat temperature from this time instance onwards. However, the final set-point supersaturation level of $S = 0.975$ could be realized almost exactly.

The switching procedures were automatically calculated and optimized during the growth and dissolution phases after each new CSSD observation, and hence, a cyclic crystallization process between the volume constraints of V_{min} and V_{max} could be realized in a reliable manner, see Figure 4.9. However, the target crystal shape has to be expected to be not exactly attainable, except for special cases, by a growth-dissolution process that is solely cycling between the volume constraints of V_{min} and V_{max}. Instead, such a process typically results in an overshoot of the CSSD-evolution, which in turn results in the target crystal shape lying outside of the region attainable by growth-dissolution cycles, as depicted in the left panel of Figure 4.9. Furthermore, it would result in unnecessarily prolonged process times. To avoid such a scenario and to reach the target crystal shape exactly, an automated check whether the current growth or dissolution phase had to be ended prematurely was performed. For this purpose, $\mathbf{h}_{S,end}$ was defined as the predicted mean seed crystal shape after a switching phase. With this definition, either the condition

$$[1, \, -G_1/G_2] \cdot \begin{bmatrix} h_{1,F} - h_{1,S,end} \\ h_{2,F} - h_{2,S,end} \end{bmatrix} \leq 0 \tag{4.22}$$

was evaluated during a dissolution phase, or the condition

$$[1, \, -D_1/D_2] \cdot \begin{bmatrix} h_{1,F} - h_{1,S,end} \\ h_{2,F} - h_{2,S,end} \end{bmatrix} \leq 0 \tag{4.23}$$

was evaluated during a growth phase. If violated, the respective growth or dissolution phase had to be ended prematurely, as exemplarily depicted in the right panel of Figure 4.9. In this
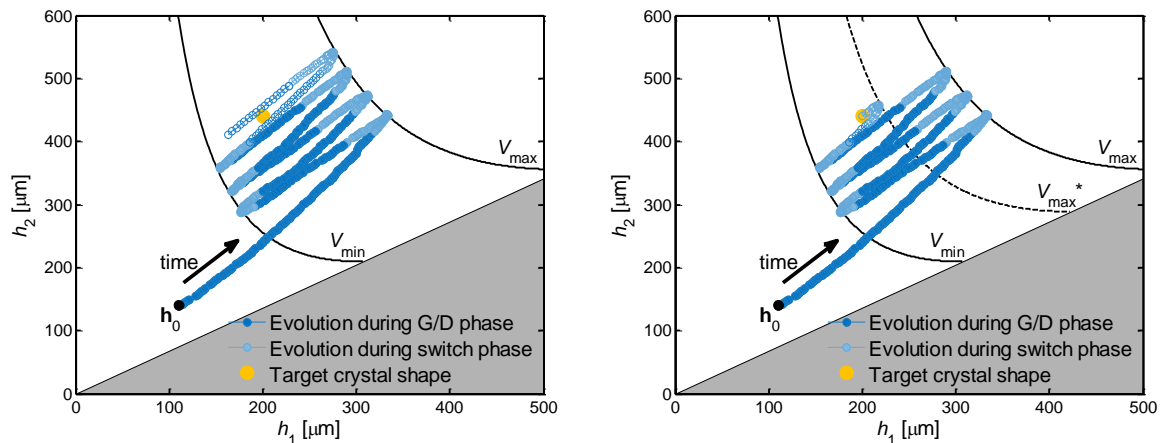
Figure 4.9: Adjustment of the last switching instance; left: Target crystal shape is missed by a full last growth period; right: Adjustment of the duration of the last growth period by V_{max}^*. Measurements are depicted by full markers, whereas model predictions are indicated by empty markers.

case, the constraint on the minimal or maximal crystal volume was replaced by either V_{min}^* or V_{max}^*, see Figure 4.9 right, such that the left hand sides of Eq. (4.22) or Eq. (4.23) was exactly zero after re-simulating the switching procedure. By this procedure the target crystal shape could be achieved with high precision, as demonstrated in Section 4.5 of this work where the experimental realization of controlled growth-dissolution cycles is addressed.

4.4 Kalman Filter

As discussed in the previous section, the accuracy with which the target crystal shape can be attained depends on an accurate determination of the last switching point. This accuracy is in turn dependent on the precision with which the mean crystal shape evolution can be observed. A crystal shape evolution observed during one cyclic growth-dissolution experiment is exemplarily depicted in Figure 4.10. As can be seen, the overall evolution could be tracked well with the observation techniques presented in Section 2.4. However, due to the rather low seed loading used in this experiment, the individual mean shape observations were subject to noticeable measurement noise. This noise was increasing with time and achieved maximal values at the end of each growth phase. Determining the last switching point on the basis of the measurement noise that was encountered at the end of this experiment would clearly lead to similar uncertainties in the final crystal shape. To reduce these uncertainties, and to thereby improve the controllability of the entire process, the measured mean crystal shape evolutions were smoothed by means of a Kalman filter. This Kalman filter is briefly described here and adjusted to the dynamics of the crystallization process. For a more detailed description of a Kalman filter, the reader is referred to Brown and Hwang (1995) or Welch and Bishop (2006).
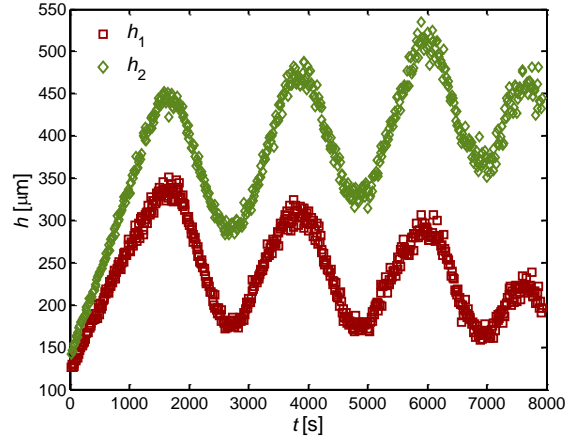
Figure 4.10: Unfiltered observations of the mean seed crystal shape evolution over time. The face distances h_1 of the prismatic {100}-faces are indicated by red squares and the face distances h_2 of the pyramidal {101}-faces are depicted by green diamonds

The Kalman filter estimates the state ($\mathbf{x} = \overline{\mathbf{h}}$) of the crystallization process. The dynamics of the crystal shape evolution during the time interval t_{k-1} and t_k can generally be described by:

$$\mathbf{x}_k = f\left(\mathbf{x}_{k-1}, \mathbf{u}_{k-1}, \mathbf{w}_{k-1}\right),$$ (4.24)

with $\mathbf{x}_k$ and $\mathbf{x}_{k-1}$ being the states at t_k and t_{k-1} respectively, with $\mathbf{u}_{k-1}$ denoting the vector of control inputs, and with the random variables $\mathbf{w}_{k-1}$ representing the process noise. The measurements $\mathbf{z}_k$ are related to the state $\mathbf{x}_k$ by:

$$\mathbf{z}_k = g\left(\mathbf{x}_k, \mathbf{v}_k\right),$$ (4.25)

with the random measurement noise $\mathbf{v}_k$. By using the definition of the face-specific growth rates G_i, the control inputs $\mathbf{u}_{k-1}$ can be defined as:

$$\mathbf{u}_{k-1} = \begin{bmatrix} \int_{t_{k-1}}^{t_k} G_1(\tau)d\tau \\ \int_{t_{k-1}}^{t_k} G_2(\tau)d\tau \end{bmatrix}.$$ (4.26)

Naturally, similar control inputs can be defined for dissolution as well, which is, however, omitted in this section for the sake of brevity. The definition of $\mathbf{u}_{k-1}$ allows formulating the process dynamics of Eq. (4.24) as the following linear stochastic difference equation:

$$\mathbf{x}_k = \mathbf{x}_{k-1} + \mathbf{u}_{k-1} + \mathbf{w}_{k-1} = \mathbf{A}\mathbf{x}_{k-1} + \mathbf{B}\mathbf{u}_{k-1} + \mathbf{w}_{k-1}$$ (4.27a)
$$\mathbf{z}_k = \mathbf{C}\mathbf{x}_k + \mathbf{v}_k.$$ (4.27b)

In this formulation, the Jacobian matrices

$$\mathbf{A} = \left[\frac{\partial f_i}{\partial x_j}\right]_{i,j=1,2}, \quad \mathbf{B} = \left[\frac{\partial f_i}{\partial u_j}\right]_{i,j=1,2}, \quad \mathbf{C} = \left[\frac{\partial g_i}{\partial x_j}\right]_{i,j=1,2}$$ (4.28)

are each equal to the identity matrix $\mathbf{I}_2$ and constant over time. Given an *a posteriori* state estimate $\hat{\mathbf{x}}_{k-1}$ from the previous observation time t_{k-1} together with a control input $\mathbf{u}_{k-1}$, an *a*

priori state estimate $\hat{\mathbf{x}}_k^-$ (denoted by the superscript –) can be obtained through Eq. (4.27a) by neglecting the process noise $\mathbf{w}_{k-1}$:

$$\hat{\mathbf{x}}_k^- = \mathbf{A}\hat{\mathbf{x}}_{k-1} + \mathbf{B}\mathbf{u}_{k-1}. \tag{4.29}$$

An *a priori* estimate of the error covariance matrix $\mathbf{P}_k^-$ can be calculated by using the process noise covariance matrix $\mathbf{Q}_k$ via:

$$\mathbf{P}_k^- = \mathbf{A}\mathbf{P}_{k-1}\mathbf{A}^\mathrm{T} + \mathbf{Q}_{k-1} \tag{4.30}$$

In order to obtain an *a posteriori* estimate $\hat{\mathbf{x}}_k$ on the basis of the *a priori* estimate $\hat{\mathbf{x}}_k^-$ and the measurements $\mathbf{z}_k$, the Kalman gain $\mathbf{K}_k$ is introduced. This Kalman gain weights the differences between the measurements $\mathbf{z}_k$, and the predicted measurements $\mathbf{C}\hat{\mathbf{x}}_k^-$, and is calculated by:

$$\mathbf{K}_k = \mathbf{P}_k^- \mathbf{C}^T \left(\mathbf{C}\mathbf{P}_k^- \mathbf{C}^\mathrm{T} + \mathbf{R}_k \right)^{-1} \tag{4.31}$$

with the measurement error covariance matrix $\mathbf{R}_k$. Using the Kalman gain $\mathbf{K}_k$, *a posteriori* estimates for the state vector $\hat{\mathbf{x}}_k$ and the error covariance matrix $\mathbf{P}_k$ can be calculated as soon as a new set of measurements $\mathbf{z}_k$ is available by:

$$\hat{\mathbf{x}}_k = \hat{\mathbf{x}}_k^- + \mathbf{K}_k \left(\mathbf{z}_k - \mathbf{C}\hat{\mathbf{x}}_k^- \right), \tag{4.32}$$

and:

$$\mathbf{P}_k = \left(\mathbf{I} - \mathbf{K}_k\mathbf{C} \right) \mathbf{P}_k^- . \tag{4.33}$$

As can be seen, only the error covariance matrices $\mathbf{R}_k$ and $\mathbf{Q}_k$ need to be known in order to evaluate the filter equations, Eq. (4.29) to Eq (4.33), once $\hat{\mathbf{x}}_0$, $\mathbf{K}_0$ and $\mathbf{P}_0$ were initialized. In this work, the measurement covariance matrix $\mathbf{R}_k$ was determined by analyzing all crystal shape estimates obtained during the first growth phase of a preliminary cyclic experiment. Through the regression of the mean crystal shape evolution with the kinetics presented in Section 3.1 of this work, estimates for the mean crystal shape trajectory were obtained at any time instance. Since all observations of crystals from the seed crystal population of the entire growth time were used for the estimation, it can be assumed that the accuracy of the regressed crystal shape trajectory was significantly higher than the accuracy of a CSSD observation at a single time instance. Therefore, the obtained mean crystal shape evolution, shown as thick and dashed black line in Figure 4.11, was treated as the 'true' mean shape evolution for the estimation of $\mathbf{R}_k$. By this approach, the deviations of the estimated crystal shape of every single observed seed crystal could be calculated, as illustrated in Figure 4.11, and hence the measurement error covariance matrix for a single crystal shape measurement could be obtained. By taking into account that an estimate for $\overline{\mathbf{h}}$ was obtained by averaging over $n_{\mathrm{obs},k}$ crystals, the measurement error covariance matrix $\mathbf{R}_k$ could be determined as:
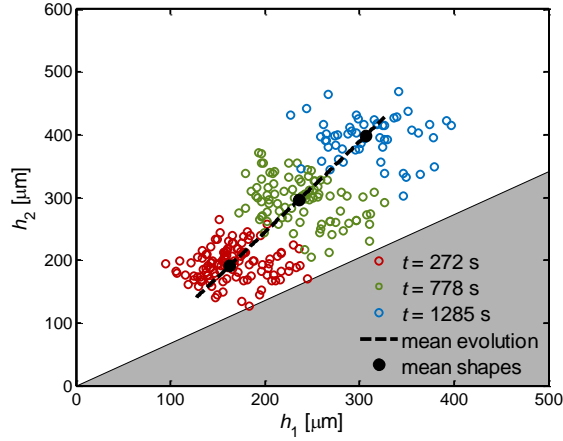
Figure 4.11: Estimation of the measurement error covariance matrix $\mathbf{R}_k$. The regressed mean crystal shape trajectory is shown as black dashed line, and three CSSDs, measured at different times, are shown with different colors. The 'true' mean crystal shapes of these CSSDs are indicated by black points.

$$\mathbf{R}_k = \frac{1}{n_{\text{obs},k}} \begin{bmatrix} 1090.8 & 178.0 \\ 178.0 & 1181.5 \end{bmatrix}. \tag{4.34}$$

Despite existing approaches (Solonen 2014), determining the process noise covariance matrix $\mathbf{Q}_k$ is generally more difficult than estimating the measurement error covariance matrix $\mathbf{R}_k$. Instead, the parameters of $\mathbf{Q}_k$ are often used as tuning parameters, to improve the performance of the Kalman filter. This was also done in this work, where the model error was set to be ten percent of the predicted advancement of the crystal population:

$$\mathbf{Q}_k = 0.01 \begin{bmatrix} \left(\int_{t_{k-1}}^{t_k} G_1(\tau) d\tau \right)^2 & 0 \\ 0 & \left(\int_{t_{k-1}}^{t_k} G_2(\tau) d\tau \right)^2 \end{bmatrix}. \tag{4.35}$$

The performance of the filter with the error matrices described above is depicted in Figure 4.12. As can be seen, the application of the filter led to a significant smoothing of the measured crystal shape evolution and the measurement noise at the end of each growth phase was completely compensated. However, a slight bias of the filtered mean shape evolution of 10 μm to 20 μm is apparent during the dissolution phases, as visible in the right panel of Figure 4.12. This bias can be attributed to uncertainties in the dissolution kinetics. To account for these uncertainties, the growth and dissolution kinetics were updated on the basis of the measured CSSD evolution during the first growth or dissolution phase respectively, as was already suggested by Jiang et al. (2014a).

To further improve the performance of the Kalman filter, the state vector $\mathbf{x}$ was extended according to:
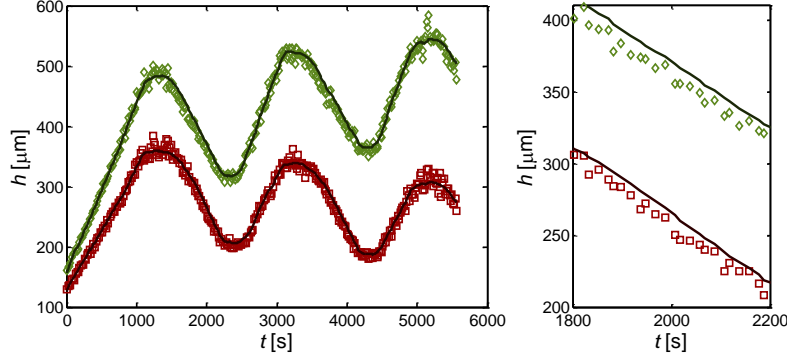
Figure 4.12: Application of the Kalman filter using the states $\mathbf{x} = \overline{\mathbf{h}}$; left: measured (marker) and filtered (solid) mean shape evolution; right: detailed depiction of the filter performance during the first dissolution phase.

$$\mathbf{x} = \begin{bmatrix} \tilde{h}_1 & \tilde{h}_2 & \delta_1 & \delta_2 \end{bmatrix}^{\mathrm{T}}, \tag{4.36}$$

from which the mean crystal shape can be obtained by:

$$\overline{h}_i = \tilde{h}_i + \delta_i. \tag{4.37}$$

With this state vector, the Jacobians **A**, **B** and **C** defined by Eq. (4.28) change according to:

$$\mathbf{A} = \mathbf{I}_4 \tag{4.38a}$$

$$\mathbf{B} = \begin{bmatrix} 1 & 0 \\ 0 & 1 \\ 0 & 0 \\ 0 & 0 \end{bmatrix} \tag{4.38b}$$

$$\mathbf{C} = \begin{bmatrix} 1 & 0 & 1 & 0 \\ 0 & 1 & 0 & 1 \end{bmatrix}. \tag{4.38c}$$

As can be seen from Eq. (4.38b), the model predictions for the *a priory* state estimates cover the mean crystal shape evolution due to growth or dissolution with the states $\tilde{h}_i$, while no change in the states δ_i is predicted. Since more states are to be estimated with this approach than measurements are available, deviations between model predictions and measurements can be assigned to the states $\tilde{h}_i$, to the states δ_i, or to both state types in a similar scale depending on the choice of the process noise covariance matrix $\mathbf{Q}_k$. In this work, the parameters of this matrix were set to:

$$\mathbf{Q}_k = 2.5 \times 10^{-5} \begin{bmatrix} \left(\int_{t_{k-1}}^{t_k} G_1(\tau)d\tau \right)^2 & 0 & 0 & 0 \\ 0 & \left(\int_{t_{k-1}}^{t_k} G_2(\tau)d\tau \right)^2 & 0 & 0 \\ 0 & 0 & 100(\Delta t_k)^2 & 0 \\ 0 & 0 & 0 & 100(\Delta t_k)^2 \end{bmatrix}. \tag{4.39}$$
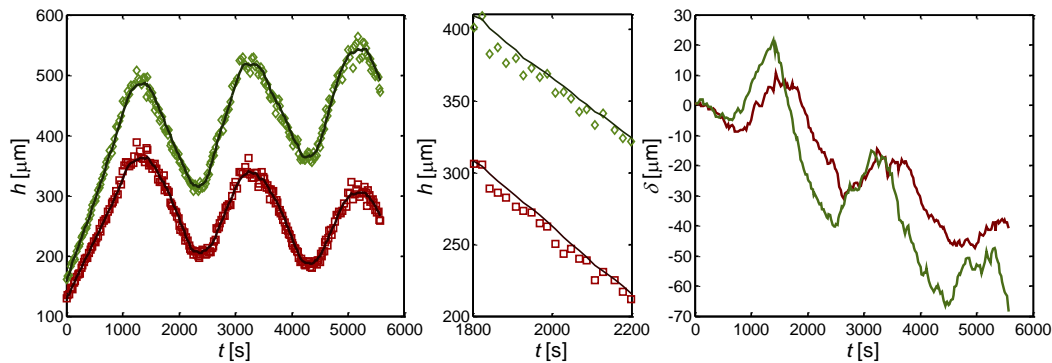
Figure 4.13: Application of the Kalman filter using the states $\mathbf{x} = [\, \tilde{h}_1 \quad \tilde{h}_2 \quad \delta_1 \quad \delta_2]^{\mathrm{T}}$**; left: measured (marker) and filtered (solid) mean shape evolution; middle: detailed depiction of the filter performance during the first dissolution phase; right: evolution of the additional states** δ_i **over time.**

Since the evaluation of the integrals in Eq. (4.39) yielded values of about 3 μm to 6 μm while the time differences Δt_k were in the order of 10 s to 20 s, any mismatch between measurements and model predictions was essentially attributed to the states δ_i, while the states $\tilde{h}_i$ evolved according to the model predictions. Due to this additional flexibility in the estimated states, the bias between filtered and measured mean shape evolution during the dissolution phases, as observable in Figure 4.12, could be reduced significantly while the overall performance of the filter still showed good results in terms of smoothness and convergence, as depicted in Figure 4.13.

With the help of this Kalman filter, the controllability of the cyclic crystallization process can be expected to be increased. Therefore the filtering methods presented in this section were directly applied to the experiments for the shape manipulation by controlled growth-dissolution cycles that are presented in the next section.

4.5 Experimental Realization of Growth-Dissolution Cycles

In this section, the experimental realization of crystal shape control through growth-dissolution cycles is discussed. To realize the process in a time-optimal manner and to ensure that the target crystal shape can be obtained with high precision, the process was embedded in a hierarchical controller structure based on the control routines of the previous sections. On the highest hierarchy level of the controller, the optimal levels of supersaturation S_G^* and undersaturation S_D^* were determined by solving the optimization problem of Eq. (4.1). Within the solution of Eq. (4.1), the initial crystal shape $\mathbf{h}_0$ (occurring in Eqs. (4.2) and (4.3)) was replaced by the latest filtered observation of the mean seed crystals shape. Through this repeated optimization, a robustness of the time optimal crystal shape trajectory with respect to uncertainties in the model prediction could be achieved. Once S_G^* and S_D^* were determined, a trajectory planning was performed, in which the next switching point was determined through either Eq. (4.20) or (4.21) together with the corresponding temperature profiles of the thermostats. Additionally, Eqs. (4.22) or (4.23) were evaluated to check
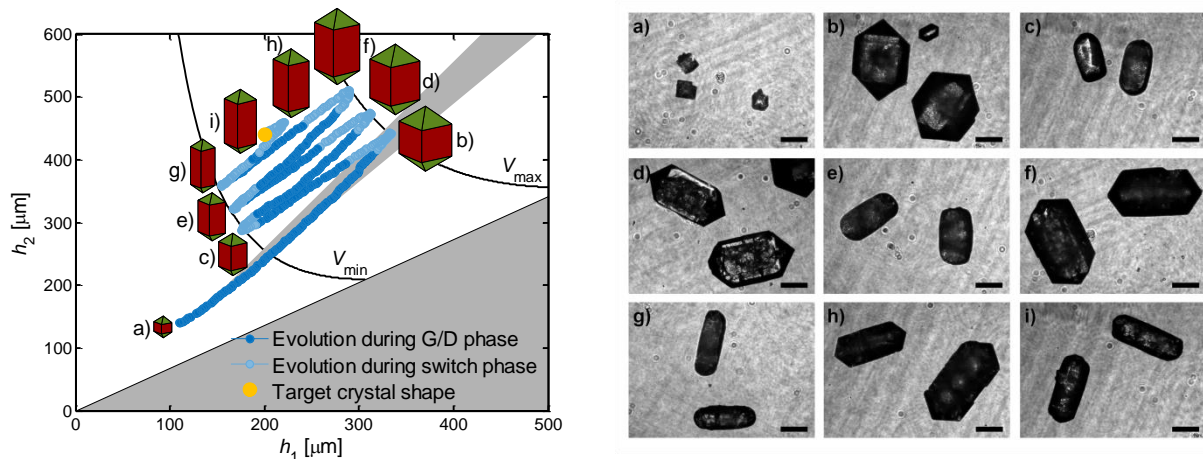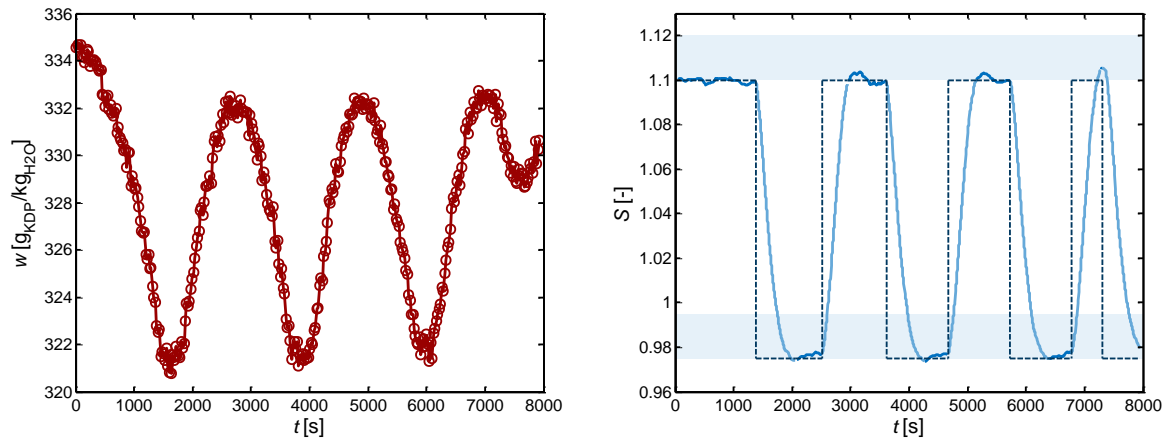
Figure 4.14: Observed CSSD evolution during a cyclic growth-dissolution process with $1.10 \leq S_G \leq 1.12$; left: Filtered mean crystal shape evolution during the growth and dissolution phases (dark blue) and during the switching phases (light blue) and example crystal shapes during the switching phases; right: example crystal photographs corresponding to the example crystals depicted in the left panel. Scale bars in the lower right corners of the micrographs correspond to 400 µm.
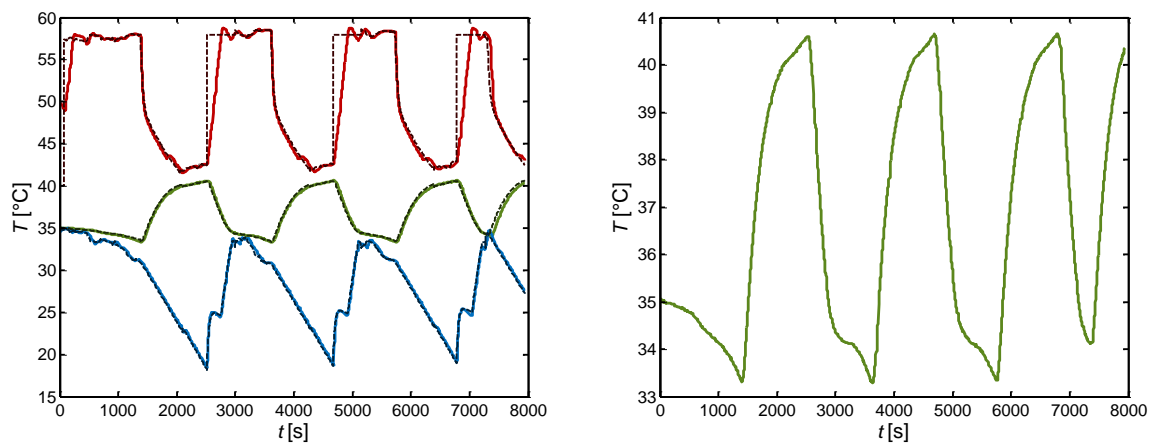
Figure 4.15: Experimentally realized temperature profiles during a cyclic growth-dissolution process with $1.10 \leq S_G \leq 1.12$; left: Measured temperature profiles for the heating thermostat (red), the crystallizer (green) and the cooling thermostat (blue) with set-point values indicated by dark dashed lines; right: detailed depiction of the measured crystallizer temperature profile.

whether a premature supersaturation switch was necessary in order to attain the target crystal shape. On the lowest hierarchy level of the controller, the optimal levels of supersaturation S_G^* and undersaturation S_D^* were realized through the supersaturation controller presented in Section 4.2.

An experimental realization of crystal shape control by growth-dissolution cycles is depicted in Figures 4.14 to 4.16. In this experiment, the supersaturation ranges were set to $1.10 \leq S_G \leq 1.12$ and $0.975 \leq S_D \leq 0.995$, respectively. The target crystal shape was set to of $\bar{\mathbf{h}}_F = [200$ µm, 400 µm$]^T$, and thus to rather elongated crystals shapes, see Figure 4.14. After the preparation of the solution with a supersaturation level of 1.10 at 35 °C, the seed material was added to the solution. Afterwards, the routines for controlling the supersaturation and for

Figure 4.16: Concentration profiles measured during a cyclic growth-dissolution process with $1.10 \leq S_G \leq$ 1.12; left: Measured concentration profile; right: Supersaturation profile resulting from the measured concentration and temperature profiles. Set-point values are indicated by dark dashed lines and the regions of applicable supersaturation and undersaturation levels are marked by light blue areas.

controlling the crystal shape trajectory described in Sections 4.2 and 4.3 were started together with the video collection and the automated image processing programs.

The resulting observed mean crystal shape evolution is depicted in the left panel of Figure 4.14, together with representative shapes of the mean seed crystals with maximal or minimal volumes during the switching phases. For comparison, also exemplary micrographs of the observed crystals are included in the right panel of Figure 4.14. As can be seen, the seed crystal population was gradually evolving towards the target crystal shape, and the region attainable by a growth phase under these supersaturation constraints - indicated by a gray shaded region originating at the initial mean seed shape - could be left by subsequent dissolution and growth phases. Due to the availability of real time observations of the CSSD, the developed algorithms for controlling the mean seed crystal trajectory were successful in realizing a cyclic growth dissolution process between the volume constraints V_{min} and V_{max} as well as in attaining the target crystal shape with high precision. Interestingly, the slopes of the mean shape evolution during different growth and dissolution phases were essentially parallel, indicating that the underlying growth and dissolution kinetics were indeed not dependent on crystal size or shape.

The measured temperature profiles for both thermostats and the crystallizer are shown in Figure 4.15. Due to the use of two thermostats, the temperature changes which were necessary to realize the supersaturation switches could be realized reasonably fast with durations of approximately 11 minutes for switches from growth to dissolution and approximately 8 minutes for switches from dissolution to growth. However, the total time that was required for all supersaturation switches in this experiment was 4068 s yielding a total process time of 7942 s. In contrast to this experimentally realized process time, the solution of the optimal control problem, which assumes negligible switching times as discussed in Section 4.1 yields a total process time of 5450 s (see Figures 4.1 and 4.2, which were simulated with the same parameters that were also used in this experiment). Hence, an
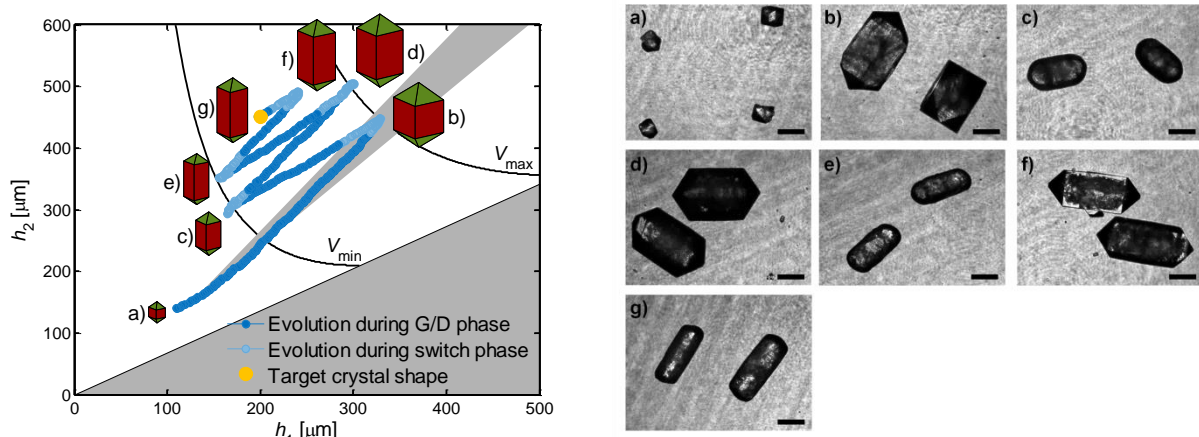
Figure 4.17: Observed CSSD evolution during a cyclic growth-dissolution process with $1.09 \leq S_G \leq 1.12$; left: Filtered mean crystal shape evolution during the growth and dissolution phases (dark blue) and during the switching phases (light blue) and example crystal shapes during the switching phases; right: example crystal photographs corresponding to the example crystals depicted in the left panel. Scale bars in the lower right corners of the micrographs correspond to 400 µm.

increase of almost 46% of the total process time due to the supersaturation switches was observable in this experiment.

The set-point profiles of the thermostat and the crystallizer temperature, indicated by dark dashed lines in the left panel of Figure 4.15, could be realized well and led to good controllability of the concentration and supersaturation profiles during the experiment, as shown in Figure 4.16. As can be seen from the left panel of this figure, the concentration level is reliably cycling between a maximal and minimal value. This indicates that a cyclic crystallization process bounded by the maximal and minimal crystal volume V_{min} and V_{max}, can indeed be controlled using the concentration measurements as proposed by Bajcinca (2013), provided that the solute consumption due to the growth of nucleated crystals can be neglected. The measured supersaturation profile of this experiment is depicted in the right panel of Figure 4.16. The supersaturation level could be controlled extremely well during the first growth period, and only slight deviations from the set-point level occurred, which were, however, reliably corrected by the PI supersaturation controller presented in Section 4.2. Also the supersaturation switches performed based on the methods presented in Section 4.3 could be realized accurately. Only switches from dissolution to growth resulted in slight overshoots in the supersaturation level, which were, however, compensated reasonably fast by the supersatruation controller to maintain the set-point supersaturation level afterwards. The dashed lines in Figure 4.16 indicate the optimized supersaturation levels over time. As can be seen, the lower bounds for S_G and S_D were active throughout the entire crystallization time. For undersaturated conditions this lower bound corresponds to the maximal dissolution velocities, while for supersaturated conditions, the application of the minimal growth velocities were found to be optimal. This can be explained by the growth kinetics in the chosen supersaturation interval. At lower supersaturation levels, KDP crystals grow towards more elongated crystals, and thus more towards the final crystal shape as compared to higher supersaturation values. Therefore, an even further decrease in the total crystallization time can be expected if the value for the minimal applicable supersaturation is decreased.
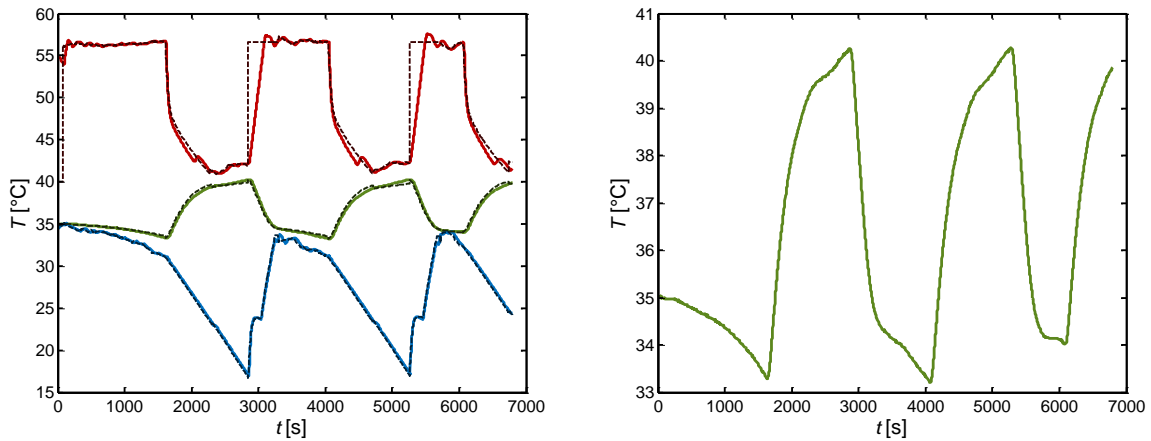
Figure 4.18: Experimentally realized temperature profiles during a cyclic growth-dissolution process with $1.09 \leq S_G \leq 1.12$; left: Measured temperature profiles for the heating thermostat (red), the crystallizer (green) and the cooling thermostat (blue) with set-point values indicated by dark dashed lines; right: detailed depiction of the measured crystallizer temperature profile.

Such an experiment was conducted in which the constraints for the applicable supersaturation for growth were relaxed to $1.09 \leq S_G \leq 1.12$ while the undersaturation ranges for dissolution were identical to the previous experiment. The results of this experiment are depicted in Figures 4.17 to 4.19, and discussed below.

The filtered mean crystal shape evolution that was measured during the second experiment is shown in Figure 4.17. As in the previous experiment, this evolution could be tightly controlled with the controller routines that were developed in this work. A slight overshoot of the measured trajectory is only visible during the first switch from dissolution to growth, where the constraint for the minimal crystal volume was slightly violated. The subsequent supersaturation switches were, however, accurately controlled, and hence the target crystal shape could be obtained almost exactly. Notably, the number of supersaturation switches necessary to reach the target shape could be reduced by two.

This can be attributed to the growth phases which were, as already expected, performed at a supersaturation of $S = 1.09$ (see also Figure 4.19). While the application of this supersaturation led to longer individual growth phases (approximately 1700 s compared to 1300 s for the first growth phases of both experiments) the crystal shape trajectory was evolving more toward the target crystal shape than at $S = 1.10$. This resulted in the observed reduction of the number of necessary supersaturation switches which in turn resulted in a decrease of the total process time to only 6799 s, compared to 7942 s for the previously discussed experiment. The constraint for the minimal supersaturation was again active throughout the entire growth phases of this experiment (see Figure 4.19), which still indicated that a further relaxation of this constraint would result in an even further decrease in the total process time. As this decrease is, however, accompanied with an increase in the uncertainties of the growth kinetics (see the according discussion in Section 3.2) a further decrease of $S_{G,min}$ was not considered in an additional experiment.

The supersaturation levels themselves could again be tightly controlled with the methods developed in this work. The overshooting behavior resulting from the supersaturation
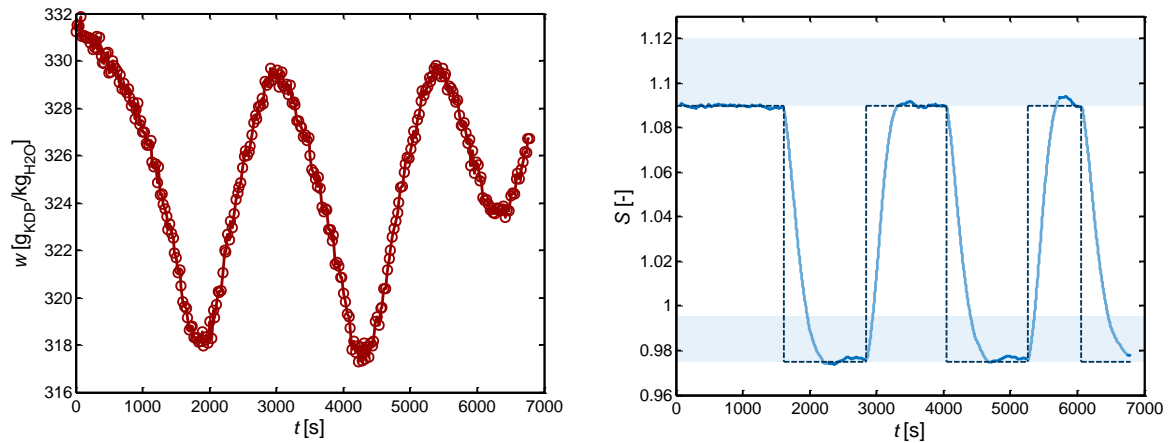
Figure 4.19: Concentration profiles measured during a cyclic growth-dissolution process with $1.10 \leq S_G \leq 1.12$; left: Measured concentration profile; right: Supersaturation profile resulting from the measured concentration – and temperature profile. Set-point values are indicated by dark dashed lines and the regions of applicable supersaturation and undersaturation levels are marked by light blue areas.

switches were again compensated reasonably fast by the PI controller, which was successful in maintaining the level of supersaturation or undersaturation constant afterwards.

The experimental results described above clearly demonstrate the effectiveness of the controller routines that were developed in this work. The crystal shape trajectory could be tightly controlled with respect to the constraints within the state-space that were considered, and the target crystal shape could ultimately be attained reliable and with high precision. It can thus be safely assumed that the availability of online measurements of the CSSD offers (in conjunction with adequate controller strategies) the possibility to control crystal shape distributions in a variety of different concepts for crystallization processes. While this work is the first demonstration in which such feedback on crystal size and shape was employed for the control of a cyclic batch crystallization processes, it can be expected that the closed-loop control of the crystal size and shape distributions will have an important role in the future design of crystallization processes.

Both experiments described above were consistent in enlarging the region of crystal shapes attainable by pure growth processes under the given constraints on supersaturation. Hence, it can be concluded that the application of growth-dissolution cycles does indeed constitute a viable process concept to control crystal shape distributions through pure temperature control.

4.6 Summary – Growth-Dissolution Cycles

This chapter was focused investigating the process concept of growth-dissolution cycles for the manipulation of crystal shapes. Initially, the optimal control solutions of Bajcinca (2013) and Bötschi et al. (2017) for a time-minimal process were summarized and adjusted to the growth and dissolution kinetics of this work. One key result of both approaches is the

optimality of constant levels of supersaturation and undersaturation during the individual growth and dissolution phases. Therefore, a supersaturation controller was developed in this chapter. To derive the controller equations, the process model was inverted in such a way, that a temperature profile for the thermostat was obtained, which is necessary to maintain the level of supersaturation or undersaturation constant during grow or dissolution. The resulting equation was used as input in a PI feedback controller structure, whose application led to satisfactory results during simulations and experimental realizations.

Furthermore, the time-optimal procedures for the switches between growth and dissolution or dissolution and growth were derived, and realized experimentally. Due to the accuracy of the crystallization kinetics and the model equations for the crystallizer temperature, a reliable and precise switching between different supersaturation and undersaturation levels could be achieved, and the CSSD could be forced to evolve within the given constraint on maximal and minimal crystal volume. Also the time instance for the final switching procedure could be identified, ensuring that the target crystal shape could be reached with high precision.

To improve the controllability of the crystallization process, a Kalman filter was applied to the CSSD measurements. With this filter, a reduction in measurement noise was obtained, and therefore, the precision to which the switching procedures could be initiated and to which the target crystal shape could be attained was significantly increased.

The final section of this chapter was concerned with the experimental realization of controlled growth-dissolution cycles for the shape manipulation of KDP crystals. The controller routines of the previous sections were implemented in a hierarchical structure, to control the overall process. In order to achieve a desired target crystal shape with time minimal effort, the optimal supersaturation and undersaturation levels were continuously calculated and realized through the supersaturation controller. The CSSD was forced to cycle between the constraints for the minimal and maximal mean seed crystal volume to ensure that a minimal number of supersaturation switches was required. Due to the precise measurements of the CSSD evolution, the crystallization process could be controlled well, and the target crystal shape could be obtained with high precision, as demonstrated in two separate experiments. Both experiments demonstrate that the region of crystal shapes can be enlarged compared to pure growth processes, thus proving the applicability of growth-dissolution cycles for crystal shape control.

5. Conclusions and Outlook

This chapter aims at summarizing and concluding the results that were presented in the previous sections. Furthermore, some open questions are addressed, and fields that require further research and development are identified in this chapter. In order to structure this discussion, four main research fields are identified to which this work contributes. These fields cover the acquisition of real-time observations of the state of the solid phase (addressed in Section 5.1), the determination of face-specific crystallization kinetics (Section 5.2), the closed-loop control of crystallization processes (Section 5.3) and finally the application of growth-dissolution cycles for crystal shape control (discussed in Section 5.4).

5.1 Crystal Shape Observer

The observation of a crystallization process with respect to the state of the solid phase is a key technology for understanding and ultimately for controlling the dynamics that are governing the crystallization process. Despite the existence of alternative measurement principles, like FBRM, Coulter Counter or laser diffraction, the use of video microscopy has been shown to be a promising and successful technology for this purpose by several publications in the past decade and as well by this work. In fact, it was recently demonstrated for the example of needle-like crystal shapes that only the application of video microscopy (and in particular stereo microscopy) allows for a precise estimation of growth kinetics (Albuquerque 2016).

The images recorded by video microscopy offer an immediate impression of the state of the crystalline phase to a human operator. An automated observation requires however reliable routines for object identification and quantification. Particularly the later criterion poses a major challenge, if crystals with non-spherical shapes are to be measured. In such cases, simple scalar measurements, like equivalent diameters or Ferret lengths, are not suited to describe the actual crystal shape. Instead, advanced algorithms to reconstruct the crystal shape from the measured crystal projections are necessary. The application of such algorithms in combination with the necessity of processing the collected video frames requires an efficient implementation in order to reduce the required computation time and ultimately to obtain measurement information about the state of the crystalline phase in real time. This is particularly challenging due to the large amount of data (in the order of several hundred megabytes per second) that has to be processed. Therefore, the successful implementation of algorithms that are capable of observing the size and shape distribution of a crystal population was the main focus of this work in the field of crystal shape observations. A real-time observation could be demonstrated for the first time, and has to be regarded as the most important contribution of this thesis to this research area.

This work was exclusively focused on the estimation of KDP crystal shapes from images that were obtained from a single camera. In fact, the geometry of KDP crystals constitutes a rather simple example in this context as the crystal shape can be described by a simple geometrical model and varies essentially only in crystal length and width. In case of more complex crystal geometries, as they can be expected for example for Paracetamol[14] or L-Methionine[15], a successful shape estimation using only a single camera remains to be demonstrated. As an alternative to measurements with a single camera, the use of a stereoscopic camera setup was suggested and convincingly demonstrated by several authors (Schorsch 2014, Ochsenbein 2015 or Albuquerque 2016). Such a setup does not only provide additional measurement information that can be used for shape estimation, but it also allows the application of generic crystal shapes with the help of which the true crystal geometry can be approximated. Hence, a (possibly simplified) description of complex crystal shapes can be facilitated by such a measurement setup.

Although the potential of observing a crystallization process by use of video microscopy could be clearly demonstrated in this work, the automated application of such a measurement setup in industrial crystallization processes is still limited. This is in particular due to the low suspension densities that are required for this technology, that are uneconomical in industrial practice. In case of the application of microscope probes at high suspension densities, the observability of the process suffers from crystal overlapping as well from crystals that are not located in the focal plane of the camera leading to blurred crystal images. Although both issues have been addressed in the context of estimating bubble size distributions in multiphase systems (Honkanen 2005, Honkanen 2010, Zhang 2012), similar algorithms are rare in the field of crystallization, with the notable exception of the pioneering work of Larsen and coworkers (Larsen 2006, Larsen 2007a, Larsen 2007b, Larsen 2008).

The problems associated with overlapping and out-of-focus crystals that are arising for microscope probes can be (partially) resolved by the application of flow-through microscopes if the geometry of the flow-through cell is properly designed. However, the improvement in image quality that is typically obtained by such devices comes at the price of an additional external sampling loop. This sampling loop induces an imminent danger of clogging, in particular at high suspension densities. Avoiding such a scenario does therefore require an artificial dilution of the suspension that is circulated in the sampling loop. This can be achieved by providing an additional stream of clear solution, either by filtering the solution

---

[14] The shape of monoclinic Paracetamol (under ambient conditions the stable polymorph of Paracetamol) is typically characterized by four different face-types (Ristic 2001, Kuvadia 2011). This high number of possible face types results, in conjunction with the symmetry operations of the space group $P2_1/a$ (Boerrigter 2002), in a large number of qualitatively different crystal shapes that are geometrically possible (Borchert 2012b, Singh 2013).

[15] L-Methionine crystals grown from water are known to have a distinct plate-like crystal shape due to the slow growth rates of the {001}-faces (Shim 2016). Since the {001}-faces have to be expected to be oriented preferably parallel to the image plain in the flow through cell, an accurate estimation of the crystal thickness cannot be guaranteed in a single camera setup.

from the crystallization vessel, as for instance proposed by Schorsch et al. (2012), or by providing an additional stream of saturated solution. Technical realizations of such setups are however currently not commercially available, which has to be considered as one of the major bottlenecks for the application of flow-through microscopes in industrial processes.

It is clear from the discussion above, that further research and development is required to establish video microscopy as a standard observation tool in industrial crystallization processes which are featuring high suspension densities. In turn, future developments in this area can be expected to lead to developments that allow for the full exploitation of the advantages of video microscopy in industrial practice and can therefore be expected to be highly relevant in technical applications.

5.2 Crystallization Kinetics

The ability to observe a crystallization process with respect to the state of the liquid as well as to the state of the solid phase, offers the ability to determine the crystallization kinetics under realistic process conditions. Therefore, the precision, with which the kinetics can be obtained, can be expected to be significantly increased compared to experiments on a single crystal level. Single crystal experiments are often time consuming, and require repetition experiments in order to be robust against growth rate dispersion. However, even if the distribution of grow rates can be accurately determined by those experiments, the applicability of the kinetics to batch crystallization processes remains questionable. This is particularly due to differences in the fluid dynamics of batch processes and of the single crystal experiments. In fact, the comparison of the growth kinetics of KDP that were determined in this work to literature data given in Figure 3.6 reveals that, even under batch conditions but different fluid dynamics, the crystallization kinetics show significant differences. This signifies the importance of determining the crystallization kinetics under real process conditions.

This importance is increased even further, if the impurities that are present in the solution are affecting the growth kinetics, and are therefore a major source of batch-to-batch variations. This was clearly the case in the experiments described in Chapter 3. Due to the accurate measurements of the face-specific growth rates at different levels of supersaturation and temperature, the effect of impurities on the growth kinetics could not only be identified, but as well described by the combination of the step-pinning mechanism and the classical BCF-theory of spiral growth. By analyzing the growth kinetics that were obtained, it was evident that the majority of crystal shapes that can be obtained through crystal growth require supersaturations at which the growth of the prismatic {100}-faces of KDP is strongly influenced by the presence of impurities in the solution. As these impurity concentrations have to be considered to fluctuate between different batches and raw material charges, a pure growth process under such supersaturation levels was deemed unreliable. Instead, it was

concluded, that growth should be performed under higher driving forces, at which growth is no longer influenced by the impurities.

Due to the accurate observation of the CSSD over time, also the phenomena of growth rate dispersion and secondary nucleation were observed and parameterized. The CSSD-widening, which is accompanied by growth rate dispersion, could be modeled with the random fluctuation model, whose face-specific growth rate diffusivities were determined, and a positive correlation of these values with the face-specific growth rates was found.

A second series of experiments was conducted to determine the face-specific dissolution rates of KDP. It was found, that both face-types dissolve at similar rates, and the obtained kinetics indicate that dissolution is diffusion limited. The appearance of high-indexed faces on the outer crystal surfaces was clearly visible, which, together with the diffusion limitation, is in accordance with the classical Hartman-Perdock theory. The appearance of higher indexed faces, however, changes the crystal shape from faceted objects to elliptical crystals, as shown for example in Figure 3.20. Hence, the crystal shape model which was employed for the shape estimation was not strictly adequate. While it could be shown for the case of KDP that accurate shape estimation was possible, it has to be emphasized, that this will in general not be the case for more complex crystal shapes. In such cases, the application of a shape model for faceted crystals might lead to poor and biased estimates for the face distances and consequently for the dissolution rates. This situation can be resolved by performing experiments at constant undersaturation, controlled for example by a model-free controller, and switching to supersaturated conditions at the final state of the experiments. As soon, as the expected face-types re-appear on the crystal surface, the shape model that is used for the estimation is adequate again. With this procedure, the dissolution rates can be obtained by measuring the displacement of crystal population between the beginning of the dissolution process and the instance at which the crystals re-assume their faceted geometry.

5.3 Closed-Loop Control of Crystallization Processes

Control of crystallization processes generally serves to improve the process with respect to the final properties of the crystal shape distribution as well as to improve the process robustness. While the first aspect can be resolved by means of optimal control, the process robustness can be improved through closed-loop control, which exploits the observations of the process that are available. Such a closed-loop control of a batch crystallization process was realized with respect to two different objectives.

The first objective of the present work was the control of supersaturation profiles over time. While this objective was pursued as a prerequisite for time-optimal cyclic processes, the applicability of the developed methods stretches far beyond this scope. In fact, control of supersaturation profiles offers direct control over the crystallization kinetics and is hence a

key aspect in realizing crystallization processes that are optimal with respect to various different objectives. Such objectives include for example the minimization of the mass or amount of nucleated crystals or the maximization of the total crystal yield (see for example Ward et al. (2006) and references therein) and lead to supersaturation profiles that result in either early- or late-growth strategies.

Although the methods for supersaturation control were developed for the rather simple task of controlling a constant level of supersaturation, the governing equations can be easily adjusted to control any (differentiable) supersaturation profile as they result from the objectives given above. Therefore, the methods developed in this work for supersaturation control can be expected to be applicable in a variety of different crystallization processes that require the realization of specific supersaturation profiles over time.

The second objective of this work was to control the crystallization process with respect to the CSSD in a closed-loop manner. While already the control of crystal size distributions that are characterized by a single size coordinate alone poses a major challenge for the current technologies that are available, the closed-loop control of crystal shape distributions (characterized by two size coordinates here) was realized for the first time in this work. Due to the accurate real-time observations of the CSSD, the trajectory of the mean seed crystal shape could be tightly controlled in this work, as demonstrated for the application of growth-dissolution cycles.

As in the case of supersaturation control, the applicability of the routines for controlling crystal shape distributions is not limited to the example that was studied is this work. Instead, it can be expected that the availability of CSSD measurements can be exploited to control either the crystal size or shape distribution for different process concepts in a similar fashion.

5.4 Growth-Dissolution Cycles

The control of crystal shapes by growth-dissolution cycles constitutes a promising process concept for crystal shape control, as the process is solely influenced through the supersaturation which in turn is controlled via pure temperature control. Therefore, the use of special additives or solvent changes, which are frequently used techniques to alter crystal shapes, can be omitted by this approach. Furthermore, the concept of a cyclic crystallization process inherently exploits the advantages of direct nucleation control strategies (Nagy 2011, Griffin 2015, Wu 2016) due to the required dissolution phases. Hence, and in addition to the possibility for crystal shape control, also the amount of nucleated crystals can be reliably confined[16] by this concept.

Such a cyclic crystallization process was realized for the first time in a fully closed-loop manner in this work. Due to the availability of and accurate kinetic data, the time optimal

---

[16] or even completely avoided given that the last phase is a sufficiently long dissolution phase

temperature and supersaturation profiles of this process could be well approximated in the experimental realizations. Furthermore, the availability of real-time measurements of the state of the crystalline phase enabled a tight control of the crystal shape trajectory. A reliable cycling between minimal and maximal mean seed crystal volumes was accurately realized, and the final target crystal shape could be attained with high precision. Both aspects demonstrate the efficiency and robustness of the control scheme that was developed and implemented in this work.

It was demonstrated that the region of crystal shapes which are attainable from pure growth process can be enlarged by additional dissolution phases. Therefore, the application of growth-dissolution cycles can open the way for the design of robust crystallization processes a towards more desirable crystals size and shape distributions.

However, it has to be emphasized, that the region of crystal shapes which is attainable by the application of growth-dissolution cycles does typically not cover the entire geometrical state space. Instead, the attainable region is constrained by the face-specific growth and dissolution kinetics (see Lovette et al. (2012b) for a detailed analysis). Due to these limitations, a cyclic crystallization process might in practice not always lead to improvements in the final crystal shape distribution. Consider, as a simple example, crystals whose geometry is described by two different face types and whose growth results in the formation of needle- or plate-like crystal shapes regardless of the supersaturation level that is applied, e.g. Urea (Davey 1986) or L-Methionine (Shim 2016) crystallized from water. Such crystal shapes appear, if one face type (index one for the illustrative example that follows) is growing significantly slower than the second face, which is, however, not disappearing from the crystal surface. If a cyclic growth-dissolution process is to decrease the average aspect ratio of the crystal population, a combination of supersaturation and undersaturation levels has to be found, which leads to the fulfillment of the following inequality condition:

$$\frac{G_1(S_G)}{G_2(S_G)} > \frac{D_1(S_D)}{D_2(S_D)}. \tag{5.1}$$

Such a scenario might, however, be quite unlikely as it imposes very restrictive constraints on the acceptable ratio $D_1(S_D)/D_2(S_D)$ considering the low values of the ratio $G_1(S_G)/G_2(S_G)$ that lead to the growth of needle- or plate-like crystals in the first place.

In such cases, the concept of growth-dissolution cycles might be extended to a cyclic process consisting of subsequent growth, breakage and dissolution phases, as for example demonstrated by Kim et al. (2003). Due to the low thickness of needle- or plate-like crystals, the breakage planes will be preferably oriented perpendicular to the slow growing faces. Hence, the breakage process in this concept serves to decrease the average crystal aspect ratio. The dissolution phases of this process concept are not (primarily) applied to alter the crystal shape but are used to dissolve smaller fragments originating from the breakage process and hence, serve to maintain the total number of crystals at an acceptable level. In order to increase the crystalline mass, a new growth phase is initiated after the dissolution

phase. This again leads to an increase in the average crystal aspect ratios, which is compensated by the subsequent breakage process.

In a more recent publication, this process concept was investigated by Salvatori and Mazzotti (2017) in a simulation study using face-specific growth and dissolution rates together with a model-based description of the breakage process that directly depends on the shape of the crystals. The simulation results presented by the authors indicate that the region of attainable crystal shapes can indeed be enlarged towards more compact crystal shapes compared to a 'pure' growth-dissolution process. Both publications (Kim 2003, Salvatori 2017) demonstrate the effectiveness of the concept of a cyclic growth-breakage-dissolution process for crystal shape manipulation. Considering the possible advantages of such a process clearly justifies further research in this field in terms of experimental realization and parameterization, process control and optimization, to fully exploit the potential of cyclic crystallization processes for the control of crystal shape distributions.

References

Abu Bakar, M.R., Nagy, Z.K., Rielly, C.D. (2009). Seeded batch cooling crystallization with temperature cycling for the control of size uniformity and polymorphic purity of sulfathiazole crystals. *Org. Process Res. Dev.*, **13**, 1343-1356.

de Albuquerque, I., Mazzotti, M., Ochsenbein, D.R., Morari, M. (2016). Effect of needle-like crystal shape on measured particle size distributions. *AIChE J.*, **62**, 2974-2985.

Alvarez, A.J., Singh, A., Myerson, A.S. (2011). Crystallization of cyclosporine in a multistage continuous MSMPR crystallizer. *Cryst. Growth Des.*, **11**, 4392-4400.

Bajcinca, N., Hofmann, S. (2011). Optimal control for batch crystallization with size-dependent growth kinetics. *In Proceedings of the 2011 American Control Conference (ACC 2011)*, 2558-2565.

Bajcinca, N. (2013). Time optimal cyclic crystallization. *Comput. Chem. Eng.*, **58**, 381-389.

Berglund, K.A., Larson, M.A. (1984). Modeling of growth rate dispersion of citric acid monohydrate in continuous crystallizers. *AIChE J.*, **30**, 280-287.

Binev, D. (2015). Continuous fluidized bed crystallization. Ph.D. Thesis, Otto-von-Guericke University, Magdeburg, Germany.

Bladgen, N., de Matas, M., Gavan, P.T., York, P. (2007). Crystal engineering of active pharmaceutical ingredients to improve solubility and dissolution rates. *Adv. Drug Deliv. Rev.*, **7**, 617-630.

Boerrigter S.X.M., Cuppen, H.M., Ristic, R.I., Sherwood, J.N., Bennema, P., Meekes, H. (2002). Explanation for the supersaturation-dependent morphology of monoclinic paracetamol. *Cryst. Growth Des.*, **2**, 357-361.

Borchert, C., Sundmacher, K. (2011). Crystal aggregation in a flow tube: Image-based observation. *Chem. Eng. Technol.*, **34**, 545-556.

Borchert, C., Sundmacher, K. (2012a). Morphology evolution of crystal populations: Modeling and observation analysis. *Chem. Eng. Sci.*, **70**, 87-98.

Borchert, C., Sundmacher, K. (2012b). Efficient formulation of crystal shape evolution equations. *Chem. Eng. Sci.*, **84**, 85-99.

Borchert, C. (2012c). Topics in crystal shape dynamics. Ph.D. Thesis, Otto-von-Guericke University, Magdeburg, Germany.

Borchert, C., Temmel, E., Eisenschmidt, H., Lorenz, H., Seidel-Morgenstern, A., Sundmacher, K. (2014). Image-based in situ identification of face specific crystal growth rates from crystal populations. *Cryst. Growth Des.*, **14**, 952-971.

Borsos, A., Majumder, A., Nagy, Z.K. (2016). Multi-impurity adsorption model for modeling crystal purity and shape evolution during crystallization processes in impure media. *Cryst. Growth Des.*, **16**, 555-568.

Botez, C.E., Carbajal, D., Adiraju, V.A., Tackett, R.J., Chianelli, R.R. (2010). Intermediate-temperature polymorphic phase transition in KH_2PO_4: A synchrotron X-ray study. *J. Phys. Chem. Solids*, **71**, 1576-1580.

Bötschi, S., Ochsenbein, D.R., Morari, M., Mazzotti, M. (2017). Multi-objective path planning for single crystal size and shape modification. *Cryst. Growth Des.* **17**, 4873-4886.

Brown, R.G., Hwang, P.Y.C. (1995). Introduction to random signal analysis and Kalman filtering, 2nd Edition. John Wiley & Sons Inc., York / Chichester / Brisbane / Toronto / Singapore.

Bunin, G.A., Lima, F.V., Georgakis, C., Hunt, C.M. (2010). Model predictive control and dynamic operability studies in a stirred tank: Rapid temperature cycling for crystallization. *Chem. Eng. Comm.*, **297**, 733-752.

Burton, W.K., Cabrera, N., Franck, F.C. (1951). The growth of crystals and the equilibrium structure of their surfaces. *Phil. Trans. Roy. Soc. London A*, **243**, 299-358.

Cabrera, N., Levine, M.M. (1956). On the dislocation theory of evaporation of crystals. *Philos. Mag.*, **1:5**, 450-458.

Christopher, P., Linic, S. (2010). Shape- and size-specific chemistry of Ag nanostructures in catalytic ethylene epoxidation. *ChemCatChem*, **2**, 78-83.

Clark, J.N., Ihli, J., Schenk, A.S., Kim, Y.-Y., Kulak, A.N., Campbell, J.M., Nisbet, G., Meldrum, F.C., Robinson, I.K. (2015). Three-dimensional imaging of dislocation propagation during crystal growth and dissolution. *Nat. Mater.*, **14**, 780-784.

Crank, J. (1975). The mathematics of diffusion. 2nd Edition, Oxford University Press Inc., New York.

Dandekar, P., Kuvadia, Z.B., Doherty, M.F. (2013). Engineering crystal morphology. *Annu. Rev. Mater. Res.*, **43**, 359-286.

Davey R.J., Mullin, J.W., Whiting, M.J.L. (1982). Habit modification of succinic acid crystals grown from different solvents. *J. Cryst. Growth*, **58**, 304-312.

Davey, R.J., Fila, W., Garside, J. (1986). The influence of biuret on the growth kinetics of urea crystals from aqueous solutions. *J. Cryst. Growth*, **79**, 607-613.

Dowty, E. (1980). Computing and drawing crystal shapes. *Am. Mineral.*, **65**, 465-471.

Eder, R.J.P., Schrank, S., Besenhard, M., Roblegg, E., Gruber-Woelfler, H., Khinast, J.G. (2012). Continuous sonocrystallization of acetysalicylic acid (ASA): Control of crystal size. *Cryst. Growth Des.*, **12**, 4733-4738.

Eggers, J., Kempkes, M., Mazzotti, M. (2008). Measurement of size and shape distributions of particles through image analysis. *Chem. Eng. Sci.*, **63**, 5513-5521.

Eisenschmidt, H., Voigt, A., Sundmacher, K. (2015a). Face-specific growth and dissolution kinetics of potassium dihydrogen phosphate crystals from batch crystallization experiments. *Cryst. Growth Des.*, **15**, 219-227.

Eisenschmidt, H., Bajcinca, N., Sundmacher, K. (2015b). Model-based observation and design of crystal shapes via controlled growth-dissolution Cycles. I*n J.K.H. Krist, V. Gernaey and R. Gani, editors. 12th International Symposium on Process Systems Engineering and 25th European Symposium on Computer Aided Process Engineering, Comput. Aided Chem. Eng.*, **37**, 1673-1678.

Eisenschmidt, H., Bajcinca, N., Sundmacher, K. (2016). Optimal control of crystal shapes in batch crystallization experiments by growth-dissolution cycles. *Cryst. Growth Des.*, **16**, 3297-3306.

Feng, L., Berglund, K.A. (2002). ATR-FTIR for determining optimal cooling curves for batch crystallization of succinic acid. *Cryst. Growth Des.*, **2**, 449-452.

Ferreira, A., Faria, N., Rocha, F., Teixeira, J.A. (2011). Using an online image analysis technique to characterize sucrose crystal morphology during a crystallization run. *Ind. Eng. Chem. Res.,* **50**, 6990-7002.

Flood, A.E. (2010). Feedback between crystal growth rates and surface roughening. *CrystEngComm*, **12**, 313-323.

Fu, Y.-J., Gao, Z.-S., Liu, J.-M., Li, Y.-P., Zeng, H., Jian, M.-H. (1999). The effects of anionic impurities on the growth habit and optical properties of KDP. *J. Cryst. Growth*, **198/199**, 682-686.

Gahn, C. (1997). Die Festigkeit von Kristallen und ihr Einfluss auf die Kinetik in Suspensions-Kristallisatoren. PhD. Thesis, Technical University München, Germany.

Gerstlauer, A., Mitrović, A., Motz, S., Gilles, E.-D. (2001). A population model for crystallization processes using two independent particle properties. *Chem. Eng. Sci.*, **56**, 2553-2565.

Gilbertson, L.M., Albalghiti, E.M., Fishman, Z.S., Perreault, F., Corredor, C., Posner, J.D., Elimelech, M., Pfefferle, L.D., Zimmermann, J.B. (2016). Shape-dependent surface reactivity and antimicrobial activity on nano-cupric oxide. *Environ. Sci. Technol.*, **50**, 3975-3984.

Gonzalez, R.C., Woods, R.E. (2002). Digital image processing. Prentice-Hall, Upper Saddle River, NJ.

Griffin, D.J., Grover, M.A., Kawajiri, Y., Rousseau, R.W. (2015). Mass-count plots for crystal size control. *Chem. Eng. Sci.*, **137**, 338-351.

Gunawan, R., Ma, D.L., Fujiwara, M., Braatz, R.D. (2002). Identification of kinetic parameters in multidimensional crystallization processes. *Int. J. Mod. Phys. B*, **16**, 367-374.

Guzman, L.A., Kubota, N., Yokota, M., Sato, A., Ando, K. (2001). Growth hysteresis of a potassium sulphate crystal in the presence of chromium(III) impurity. *Cryst. Growth Des.,* **1**, 225-229.

Guzman L.A., Kubota, N. (2005). Growth rate hysteresis of a potassium dihydrogen phosphate (KDP) crystal in the presence of traces of impurity. *J. Cryst. Growth*, **275**, e237-e242.

Hofmann, S., Raisch, J. (2010). Application of optimal control theory to a batch crystallizer using orbital flatness. *In 16th Nordic Process Control Workshop, Nordic Working Group on Process Control*, 61-67.

Honkanen, M., Saarenrinne, P., Stoor, T., Niinimäki, J. (2005). Recognition of highly overlapping ellipse-like bubble images. *Meas. Sci. Technol.*, **16**, 1760-1770.

Honkanen M., Eloranta, H., Saarenrinne, P. (2010). Digital imaging measurement of dense multiphase flows in industrial processes. *Flow Meas. Instrum.*, **21**, 25-32.

Hulburt, H.M., Katz, S. (1964). Some problems in particle technology: A statistical mechanical formulation. *Chem. Eng. Sci.*, **19**, 555-574.

Jiang, M., Zhu, X., Molaro, M.C., Rasche, M.L., Zhang, H., Chadwick, K., Raimondo, D.M., Kim, K.-K.K., Zhou, L., Zhu, Z., Wong, M.H., O'Grady, D., Hebrault, D., Tedesco, J., Braatz, R.D. (2014a). Modification of crystal shape through deep temperature cycling. *Ind. Eng. Chem. Res.*, **53**, 5325-5336.

Jiang, M., Zhu, Z., Jinemez, E., Papageorgiou, Waetzig, J., Hardy, A., Langston, M., Braatz, R.D. (2014b). Continuous-flow tubular crystallization in slugs spontaneously induced by hydrodynamics. *Cryst. Growth Des.*, **14**, 851-860.

Jones, C.M., Larson, M.A. (1999). Characterizing growth-rate dispersion of $NaNO_3$ secondary nuclei. *AIChE J.*, **45**, 2128-2135.

Kempkes, M., Vetter, T., Mazzotti, M. (2010). Measurement of 3d particle size distributions by stereoscopic imaging. *Chem. Eng. Sci.*, **65**, 1362-1373.

Kim, S., Wei, C., Kiang, S. (2003). Crystallization process development of an active pharmaceutical ingredient and particle engineering via the use of ultrasonics and temperature. *Org. Process Res. Dev.*, **7**, 997-1001.

Kim, S.H., Dandekar, P., Lovette, M.A., Doherty, M.F. (2014). Kink rate model for the general case of organic molecular crystals. *Cryst. Growth Des.*, **14**, 2460-2467.

Kubota, N., Mullin, J.W. (1995). A kinetic model for crystal growth from aqueous solution in the presence of impurity. *J. Cryst. Growth*, **152**, 203-208.

Kubota, N., Yokota, M., Mullin, J.W. (2000). The combined influence of supersaturation and impurity concentration on crystal growth. *J. Cryst. Growth*, **212**, 480-488.

Kubota, N. (2001). Effect of impurities on the growth kinetics of crystals. *Cryst. Res. Technol.*, **36**, 749-769.

Kuvadia, Z. B., Doherty, M. F. (2011). Spiral growth model for faceted crystals of non-centrosymmetric organic molecules grown from solution. *Cryst. Growth Des.*, **11**, 2780-2802.

Lahav, M., Leiserowitz, L. (2001). The effect of solvent on crystal growth and morphology. *Chem. Eng. Sci.*, **56**, 2245-2253.

Larsen, P.A., Rawlings, J.B., Ferrier, N.J. (2006). An algorithm for analyzing noisy, in situ images of high-aspect-ration crystals to monitor particle size distribution. *Chem. Eng. Sci.*, **61**, 5236-5248.

Larsen, P.A., Rawlings, J.B., Ferrier, N.J. (2007a). Model-based object recognition to measure crystal size and shape distributions from in situ video images. *Chem. Eng. Sci.*, **62**, 1430-1441.

Larsen, P.A. (2007b). Computer vision and statistical estimation tools for in situ, imaging-based monitoring of particulate populations. Ph.D. Thesis, University of Wisconsin-Madison, United States.

Larsen, P.A., Rawlings, J.B. (2008). Assessing the reliability of particle number density measurements obtained by image analysis. *Part. Part. Syst. Charact*. **25**, 420-433.

Larson M.A., White, E.T., Ramanarayanan, K.A., Berglund, K.A. (1985). Growth rate dispersion in MSMPR crystallizers. *AIChE J.,* **31**, 90-94.

Lasaga A.C., Luttge, A. (2001). Variation of crystal dissolution rate based on a dissolution stepwave model. *Science*, **291**, 2400-2404.

Law, M., Greene, L.E., Johnson, J.C., Saykally, R., Yang, P. (2005). Nanowire dye-sensitized solar cells. *Nat. Mater.*, **4**, 455-459.

Le Borne, S., Eisenschmidt, H., Sundmacher, K. (2016). Image-based analytical crystal shape computation exemplified for potassium dihydrogen phosphate (KDP). *Chem. Eng. Sci.*, **139**, 61-74.

Leroudier, J., Zaccaro, J., Ildefonso, M., Veesler, S., Baruchel, J., Ibanez, A. (2011). Nucleation control and rapid growth of KDP crystals in stationary conditions. *Cryst. Growth Des.*, **11**, 2592-2598.

Li, R.F., Thomson, G.B., White, G., Wang, X.Z., Calderon De Anda, J., Roberts, K.J. (2006). Integration of crystal morphology modeling and on-line shape measurement. *AIChE J.*, **52**, 2297-2305.

Li, G. (2008). Rapid z-plate seed regeneration of large size KDP crystal from solution. *J. Cryst. Growth*, **310**, 36-39.

Linic, S., Christopher, P. (2010). Overcoming limitation in the design of selective solid catalysts by manipulating shape and size of catalytic particles: Epoxidation reactions on silver. *ChemCatChem*, **2**, 1061-1063.

Lovette, M.A., Robben Browning, A., Griffin, D.W., Sizemore, J.P., Snyder, R.C., Doherty, M.F. (2008). Crystal shape engineering. *Ind. Eng. Chem. Res.*, **47**, 9812-9833.

Lovette, M.A., Doherty, M.F. (2012a). Predictive modeling of supersaturation-dependent crystal shapes. *Cryst. Growth Des.*, **12**, 656-669.

Lovette, M.A., Muratore, M., Doherty, M.F. (2012b). Crystal shape modifications trough cycles of dissolution and growth: Attainable regions and experimental validation. *AIChE J.*, **58**, 1465-1474.

Ma, D.L., Braatz, R.D. (2001). Worst-case analysis of finite-time control policies. *IEEE Trans. Cont. Sys. Tech.*, **9**, 766-774.

Ma, D.L., Tafti, D.K., Braatz, R.D. (2002). High-resolution simulation of multidimensional crystal growth. *Ind. Eng. Chem. Res.*, **41**, 6217-6223.

Ma, D.L., Braatz, R.D. (2003). Robust identification and control of batch processes. *Comput. Chem. Eng.*, **27**, 1175-1184.

Ma, C.Y., Wan, J., Wang, X.Z. (2012a). Faceted growth rate estimation of potash alum crystals grown from solution in a hot-stage reactor. *Powder Technol.*, **227**, 96-103.

Ma, C.Y., Wang, X.Z. (2012b). Model identification of crystal facet growth kinetics in morphological population balance modeling of L-glutamic acid crystallization and experimental validation. *Chem. Eng. Sci.*, **70**, 22-30.

Majumder, A., Kariwala, V., Ansumali, S., Rajendran A. (2010). Fast high-resolution method for solving multidimensional population balances in crystallization. *Ind. Eng. Chem. Res.*, **48**, 3862-3872.

Majumder, A., Nagy, Z.K. (2013). Prediction and control of crystal shape distribution in the presence of crystal growth modifiers. *Chem. Eng. Sci.*, **101**, 593-602.

Maunier, C., Bouchut, P., Bouillet, S., Cabane, H., Courchinoux, R., Defossez, P., Poncetta, J.-C., Ferriou-Daurios, N. (2007). Growth and characterization of large KDP crystals for high power lasers. *Opt. Mater.*, **30**, 88-90.

McElroy Brown, P., Myerson, A.S. (1989). The growth, dissolution and aging of terephthalic acid crystals. *AIChE J.*, **35**, 1749-1752.

Moguel, L.F., Muhr, H., Dietz, A., Plasari, E. (2010). CFD simulation of barium carbonate precipitation in a fluidized bed reactor. *Chem. Eng. Res. Des.*, **88**, 1206-1216.

Mullin, J.W., Amatavivadhana, A., Chakraborty, M. (1970). Crystal habit modification studies with ammonium and potassium dihydrogen phosphate. *J. Appl. Chem.*, **20**, 153-158.

Mullin, J.W., Nývlt, J. (1971). Programmed cooling of batch crystallizers. *Chem. Eng. Sci.*, **26**, 369-377.

Mullin, J.W. (2001). Crystallization. 4th Edition, Butterworth Heinemann: Oxford / Boston / Johannesburg / Melbourne / New Delhi / Singapore.

Muster, T.H., Prestidge, C.A. (2002). Face-specific surface properties of pharmaceutical crystals. *J. Pharm. Sci.*, **91**, 1432-1444.

Nagy, Z.K., Aamir, E., Rielly, C.D. (2011). Internal fines removal using population balance model based control of crystal size distribution under dissolution, growth and nucleation mechanisms. *Cryst. Growth Des.*, **11**, 2205-2219.

Nguyen, T.T.H., Hammond, R.B., Roberts, K.J., Marziano, I., Nichols, G. (2014). Precision measurement of the growth rate and mechanism of ibuprofen {001} and {011} as a function of crystallization environment. *CrystEngComm.*, **16**, 4568-4586.

Nývlt, J., Ulrich, J. (1995). Admixtures in crystallization. VCH Verlagsgesellschaft, Weinheim, Germany.

Ochsenbein, D.R., Schorsch, S., Vetter, T., Mazzotti, M., Morari, M. (2014). Growth rate estimation of β L-Glutamic acid from online measurements of multidimensional particle size distributions and concentration. *Ind. Eng. Chem. Res.*, **53**, 9136-9148.

Ochsenbein, D.R., Schorsch, S., Salvatori, F., Vetter, T., Morari, M., Mazzotti, M. (2015). Modeling the facet growth rate dispersion of β L-glutamic acid – Combining single crystal experiments with nd particle size distribution data. *Chem. Eng. Sci.*, **133**, 30-43.

Pantaraks, P., Matsuoka, M., Flood, A.E. (2007). Effect of growth rate history on current crystal growth. 2. Crystal growth of sucrose, $Al(SO_4)_2 \cdot 12H_2O$, KH_2PO_4, and K_2SO_4. *Cryst. Growth Des.*, **7**, 2635-2642.

Ramanarayanan, K.A., Berglund, K.A., Larson, M.A. (1985). Growth kinetics in the presence of growth rate dispersion from batch crystallizers. *Chem. Eng. Sci.*, **40**, 1604-1608.

Ramkrishna, D. (2000). Population balances: Theory and applications to particulate systems in engineering. Academic Press, San Diego / San Francisco / New York / Boston / London / Sydney / Tokyo.

Randolph, A.D., White, E.T. (1977). Modeling size dispersion in the prediction of crystal size distribution. *Chem. Eng. Sci.*, **32**, 1067-1076.

Rashkovich, L.N., Kronsky, N.V. (1997). Influence of Fe^{3+} and Al^{3+} ions on the kinetics of steps on the {100} faces of KDP. *J. Cryst. Growth*, **182**, 434-441.

Reinhold, A., Briesen, H. (2011). Convex geometry for the morphological modeling and characterization of crystal shapes. *Part. Part. Syst. Charact.*, **28**, 37-56.

Ristic, R.I., Sherwood, J.N., Shripathi, T. (1997). The influence of tensile strain on the growth of crystals of potash alum and sodium nitrate. *J. Cryst. Growth*, **179**, 194-204.

Ristic, R.I., Finnie, S., Sheen, D.B. Sherwood, J.N. (2001). Macro- and micromorphology of monoclinic paracetamol grown from pure aqueous solution. *J. Phys. Chem. B*, **105**, 9057-9066.

Salvatori, F., Mazzotti, M. (2017). Manipulation of particle morphology by crystallization, milling, and heating cycles – a mathematical approach. *Ind. Eng. Chem. Res.*, **56**, 9188-9201.

Sangwal, K. (2007). Additives and crystallization from fundamentals to applications. Wiley: Chichester.

Sasaki, T., Yokotani, A. (1990). Growth of large KDP crystals for laser fusion experiments. *J. Cryst. Growth*, **99**, 820-826.

Schöll, J., Lindenberg, C., Vicum, L., Brozio, J., Mazzotti, M. (2007). Precipitation of α L-glutamic acid: Determination of growth kinetics. *Faraday Discuss.*, **136**, 247-264.

Schorsch, S., Vetter, T., Mazzotti, M. (2012). Measuring multidimensional particle size distributions during crystallization. *Chem. Eng. Sci.*, **77**, 130-142.

Schorsch, S., Ochsenbein, D.R., Vetter, T., Morari, M., Mazzotti, M. (2014). High accuracy online measurement of multidimensional particle size distributions during crystallization. *Chem. Eng. Sci.*, **105**, 155-168.

Shekunov, B.Y., Grant, D.J.W. (1997). In situ interferometric studies of the growth and dissolution behaviour of paracetamol (acetaminophen). 1. Growth kinetics. *J. Phys. Chem. B*, **101**, 3973-3979.

Shiau, L.D., Chen, S.H., Liu, Y.C. (1999). Modelling of a fluidized-bed crystallizer operated in a batch mode. *Chem. Eng. Sci.*, **54**, 865-871.

Shim, H.-M., Myerson, A. S., Koo, K.-K. (2016). Molecular modeling on the role of local concentration in the crystallization of L-methionine from aqueous solution. *Cryst. Growth Des.*, **16**, 3454-3464.

Simone, E., Klapwijk, A.R., Wilson, C.C., Nagy, Z.K. (2017). Investigation of the evolution of crystal size and shape during temperature cycling and in the presence of a polymeric additive using combined process analytical technologies. *Cryst. Growth Des.*, **17**, 1695-1706.

Singh, M.R., Ramkrishna, D. (2013). A comprehensive approach to predicting crystal morphology distributions with population balances. *Cryst. Growth Des.*, **13**, 1397-1411.

Singh, M.R., Nere, N., Tung, H.-H., Mukherjee, S., Bordawekar, S., Ramkrishna, D. (2014). Measurement of polar plots of crystal dissolution rates using hot-stage microscopy. Some further insights into dissolution morphologies. *Cryst. Growth Des.*, **14**, 5647-5661.

Snyder, R.C., Doherty, M.F. (2007a). Faceted crystal shape evolution during dissolution or growth. *AIChE J.*, **53**, 1337-1348.

Snyder, R.C., Studener, S., Doherty, M.F. (2007b). Manipulation of crystal shape by cycles of growth and dissolution. *AIChE J.*, **53**, 1510-1517.

Solonen, A., Hakkarainen, J., Ilin, A., Abbas, M., Bibov, A. (2014). Estimating model error covariance matrix parameters in extended Kalman filtering. *Nonlin. Processes Geophys.*, **21**, 919-927.

Sun, C., Xue, D. (2014). Crystallization behaviours of KDP and ADP. *Opt. Mater.*, **36**, 1966-1969

Suwannasang, K., Flood, A.E., Rougeot, C., Coquerel, G. (2013). Using programmed heating-cooling cycles with racemization in solution for complete symmetry breaking of a conglomerate forming system. *Cryst. Growth Des.*, **13**, 3498-3504.

Suwannasang, K., Flood, C., Coquerel, G. (2016). A novel design approach to scale up the temperature cycle enhanced deracemization process: Coupled mixed-suspension vessels. *Cryst. Growth Des.*, **16**, 6461-6467.

Temmel, E., Eisenschmidt, H., Lorenz, H., Sundmacher, K., Seidel-Morgenstern, A. (2016a). A short-cut method for the quantification of crystallization kinetics. 1. Method development. *Cryst. Growth Des.*, **16**, 6743-6755.

Temmel, E., Eicke, M., Lorenz, H., Seidel-Morgenstern, A. (2016b). A short-cut method for the quantification of crystallization kinetics. 2. Experimental application. *Cryst. Growth Des.*, **16**, 6756-6768.

Thomas, T.N., Land, T.A., DeYoreo, J.J., Casey, W.H. (2004). In situ atomic force microscopy investigation of the {100} face of KH_2PO_4 in the presence of Fe(III), Al(III), and Cr(III). *Langmuir*, **20**, 7643-7652.

Tseng, Y.T., Ward, J.D. (2017). Comparison of objective functions for batch crystallization using a simple process model and Pontryagin's minimum principle. *Comput. Chem. Eng.*, **99**, 271-279.

Variankaval, N., Cote, A.S., Doherty, M.F. (2008). From form to function: Crystallization of active pharmaceutical ingredients. *AIChE J.*, **54**, 1682-1688.

Vekilov, P.G. (2007). What determines the rate of growth of crystals from solution? *Cryst. Growth Des.*, **7**, 2796-2810.

Ward, J.D., Mellichamp, D.A., Doherty, M.F. (2006). Choosing an operation policy for seeded batch crystallization. *AIChE J.*, **52**, 2046-2054.

Welch, G., Bishop, G. (2006). An introduction to the Kalman filter. UNC-Chapel Hill, TR 95-041.

White, E.T. Wright P.G. (1971). Magnitude of size dispersion effects in crystallization. *Chem. Eng. Progr. Sympos. Ser. No.*, **110**, 67, 81-87.

Wiedmeyer, V., Voigt, A., Sundmacher, K. (2017a). Crystal population growth in a continuous helically coiled flow tube crystallizer. *Chem. Eng. Technol.*, **40**, 1584-1590.

Wiedmeyer, V., Anker, F., Bartsch, C., Voigt, A., John, V., Sundmacher, K. (2017b). Continuous crystallization in a helically coiled flow tube: Analysis of flow field, residence time behavior, and crystal growth. *Ind. Eng. Chem. Res.*, **56**, 3699-3712.

Wintermantel, K. (1999). Process and product engineering – achievements, present and future challenges. *Chem. Eng. Sci.*, **54**, 1601-1620.

Wong, S.Y., Tatusko, A.P., Trout, B.L., Myerson, A.S. (2012). Development of continuous crystallization processes using a single-stage mixed-suspension, mixed-product removal crystallizer with recycle. *Cryst. Growth Des.*, **12**, 5701-5707.

Wu Z., Yang, S., Wu, W. (2016). Application of temperature cycling for crystal quality control during crystallization. *CrystEngComm*, **18**, 2222-2238.

Xu, Y., Wang, H., Yu, Y., Tian, L., Zhao, W., Zhang, B. (2011). Cu_2O nanocrystals: Surfactant-free room-temperature morphology-modulated synthesis and shape-dependent heterogeneous organic catalytic activities. *J. Phys. Chem. C*, **115**, 15288-15296.

Yang, G., Kubota, N., Sha, Z., Louhi-Kultanen, M., Wang, J. (2006). Crystal shape control by manipulating supersaturation in batch cooling crystallization. *Cryst. Growth Des.*, **6**, 2799-2803.

Yang, H.G., Sun, C.H., Qiao, S.Z., Zou, J., Liu, G., Campbell Smith, S., Cheng, H.M., Lu, G.Q. (2008). Anatase TiO_2 single crystals with a large percentage of reactive facets. *Nature*, **453**, 638-641.

Zacher, U., Mersmann, A. (1995). The influence of internal crystal perfection on growth rate dispersion in a continuous suspension crystallizer. *J. Cryst. Growth*, **147**, 172-180.

Zaitseva, N., Carman, L., Smolsky, I., Torres, R., Yan, M. (1999). The effect of impurities and supersaturation on the rapid growth of KDP crystals. *J. Cryst. Growth*, **204**, 512-524.

Zaitseva, N., Carman, L. (2001). Rapid growth of KDP-type crystals. *Prog. Cryst. Growth Charact. Mater.*, **43**, 1-118.

Zhang, W.-H., Jiang, X., Liu, Y.-M. (2012). A method for recognizing overlapping elliptical bubbles in bubble image. *Pattern Recognit. Lett.*, **33**, 1543-1548.

Zhang, Y., Sizemore, J.P., Doherty, M.F. (2006). Shape evolution of 3-dimensional faceted crystals. *AIChE J.*, **52**, 1906-1915.

Zhang, B., Willis, R., Romagnoli, J.A., Fois, C., Tronci, S., Baratti, R. (2014). Image-based multiresolution-ANN approach for online particle size characterization. *Ind. Eng. Chem. Res.*, **53**, 7008-7018.

Ziegler, G.M. (1995). Lectures on polytopes. Springer: New York / Berlin / Heidelberg.

Zumstein, R.C., Rousseau, R.W. (1987a). Growth rate dispersion by initial growth rate distributions and growth rate fluctuations. *AIChE J.*, **33**, 121-129.

Zumstein, R.C., Rousseau, R.W. (1987b). Growth rate dispersion in batch crystallization with transient conditions. *AIChE J.*, **33**, 1921-1925.

List of Figures

List of Tables

Publications

Journal Publications

Borchert, C., Temmel, E., <u>Eisenschmidt, H.</u>, Lorenz, H., Seidel-Morgenstern, A., Sundmacher, K. (2014). Image-based in situ identification of face specific crystal growth rates from crystal populations. *Cryst. Growth Des.*, **14**, 952-971.

H. Eisenschmidt improved the computational performance of the algorithms and wrote parts of the manuscript.

<u>Eisenschmidt, H.</u>, Voigt, A., Sundmacher, K. (2015). Face-specific growth and dissolution kinetics of potassium dihydrogen phosphate crystals from batch crystallization experiments. *Cryst. Growth Des.*, **15**, 219-227.

H. Eisenschmidt designed and performed the experiments and wrote the manuscript.

<u>Eisenschmidt, H.</u>, Bajcinca, N., Sundmacher, K. (2016). Optimal control of crystal shapes in batch crystallization experiments by growth-dissolution cycles. *Cryst. Growth Des.*, **16**, 3297-3306.

H. Eisenschmidt designed and implemented the controllers, performed the experiments and wrote the manuscript.

Le Borne, S., <u>Eisenschmidt, H.</u>, Sundmacher, K. (2016). Image-based analytical crystal shape computation exemplified for potassium dihydrogen phosphate (KDP). *Chem. Eng. Sci.*, **139**, 61-74.

H. Eisenschmidt provided the experimental data as well as the test data from Borchert et al. (2014) and wrote parts of the manuscript.

Temmel, E., <u>Eisenschmidt, H.</u>, Lorenz, H., Sundmacher, K., Seidel-Morgenstern, A. (2016). A short-cut method for the quantification of crystallization kinetics. 1. Method development. *Cryst. Growth Des.*, **16**, 6743-6755.

H. Eisenschmidt participated in the development of the presented methodology.

<u>Eisenschmidt, H.</u>, Soumaya, M., Bajcinca, N., Le Borne, S., Sundmacher, K. (2017). Estimation of aggregation kernels based on Laurent polynomial approximation. *Comput. Chem. Eng.*, **103**, 210-217.

H. Eisenschmidt developed parts of the methodologies, implemented and tested the algorithms, and wrote the manuscript.

Conference Proceedings

Eisenschmidt, H., Borchert, C., Sundmacher, K. (2010). Image-based measurement of crystal shape distributions. *In J. Stelzer, J. Ulrich, editors. 17th International Workshop on Industrial Crystallization, BIWIC 2010*, 241-249.

Eisenschmidt, H., Voigt, A., Sundmacher, K. (2013). Estimation of crystal shape distributions from microscopic images. *In H. Qu, J. Rantanen and C. Malwade, editors. 20th International Workshop on Industrial Crystallization, BIWIC 2013*, 215-221.

Eisenschmidt, H., Bajcinca, N., Sundmacher, K. (2015). Model-based observation and design of crystal shapes via controlled growth-dissolution cycles. *In J.K.H. Krist, V. Gernaey and R. Gani, editors. 12th International Symposium on Process Systems Engineering and 25th European Symposium on Computer Aided Process Engineering, Comput. Aided Chem. Eng.*, **37**, 1673-1678.

Bajcinca, N., Hofmann, S., Eisenschmidt, H., Sundmacher, K. (2015). Generalizing ODE modeling structure for multivariate systems with distributed parameters. *9th IFAC Symposium on Advanced Control of Chemical Processes ADCHEM, IFAC-PapersOnLine*, **48**, 240-247.

Other Conference Talks and Presentations

Eisenschmidt, H., Sundmacher, K. (2012). Bestimmung von Kristallformverteilungen aus binären Bilder. *ProcessNet-Fachausschuss Kristallisation*, Wittenberg, Germany. (Poster Presentation).

Borchert, C., Temmel, E., Eisenschmidt, H., Lorenz, H., Seidel-Morgenstern, A., Sundmacher, K. (2012). Experimental investigation on crystal size and shape dynamics. *4th European Conference on Crystal Growth, ECCG4*, Glasgow, United Kingdom. (Oral Presentation).

Temmel, E., Borchert, C., Eisenschmidt, H., Seidel-Morgenstern, A., Sundmacher, K., Lorenz, H. (2012). Online-Analyse der Kristallform- und größenentwicklung bei Kristallisationsprozessen. *AK Prozessanalytik der GDCh-Fachgruppe Analytische Chemie und der DECHEMA*, Berlin, Germany. (Poster Presentation).

Eisenschmidt, H., Voigt, A., Sundmacher, K. (2013). Experimentelle Untersuchungen zum Auflöseverhalten von Kaliumdihydrogenphosphat-Kristallen. *ProcessNet-Fachausschuss Kristallisation*, Magdeburg, Germany. (Oral Presentation).

Eisenschmidt, H., Voigt, A., Sundmacher, K. (2013). Estimation of crystal shape distributions from microscopic images. *PARTEC2013*, Nürnberg, Germany. (Poster Presentation).

Eisenschmidt, H., Voigt, A., Sundmacher, K. (2014). Image-based real time crystal shape observer. 6th International Conference on Pharmaceutical Engineering, *ICPE6*, Graz, Austria. (Oral Presentation).

Curriculum Vitae

Personal Details

Name	Holger Eisenschmidt
Date of birth	26 October 1983 in Magdeburg
Address	Lorenzlust 30, D-39128 Magdeburg

Education

08/1994 – 06/2003	**Ökumenisches Domgymnasium**, Magdeburg University-entrance Diploma
10/2003 – 03/2005	**Otto-von-Guericke-University**, Magdeburg Studies of Physics
04/2005 – 05/2011	**Otto-von-Guericke-University**, Magdeburg Studies of Process Engineering
05/2011	**Otto-von-Guericke-University**, Magdeburg Diplom-Ingenieur in Process Engineering

Work Experience

05/2010 – 10/2010	**Linde AG**, Pullach Internship
06/2011 – 12/2011	**Otto-von-Guericke University**, Magdeburg, Research Assistant
01/2012 – 03/2013	**Max-Planck-Institute for Dynamics of Complex Technical Systems**, Magdeburg, Research Assistant
04/2013 – 04/2017	**Otto-von-Guericke University**, Magdeburg, Research Assistant
Since 02/2018	**Max-Planck-Institute for Dynamics of Complex Technical Systems**, Magdeburg, Research Assistant

Awards

06/2003	**Deutsche Physikalische Gesellschaft**, Bad Honnef Free membership
03/2012	**ProcessNet Fachgruppe Kristallisation**, Bad Honnef Best poster award

Holger Eisenschmidt, den 27. Juli 2018